

DISSERTATION

Electron Emission and Energy Loss in Grazing Collisions of Multiply Charged Ions and Neutral Projectiles with Insulator Surfaces

ausgeführt zum Zwecke der Erlangung des akademischen Grades eines
Doktors der technischen Wissenschaften
unter der Leitung von

a.o. Univ.-Prof. Dr. Friedrich Aumayr
E134
Institut für Allgemeine Physik

eingereicht an der Technischen Universität Wien
Technisch-Naturwissenschaftliche Fakultät

von

Dipl.-Ing. Johannes Stöckl
9325049
Hohe Schule 5, 2122 Ulrichskirchen

Wien, am 20. Mai 2003



Kurzfassung

Im ersten Teil der vorliegenden Arbeit wird eine neuartige Elektronendetektorgeometrie für die Messung der Elektronenemission sowie des Energieverlustes der Projektilionen bei streifender Ion-Oberflächen-Streuung beschrieben. Dieser Aufbau wurde erfolgreich bei Koinzidenzmessungen von Elektronenemission aus einer reinen monokristallinen LiF Oberfläche unter streifendem Einfall von langsamen mehrfach geladenen Ionen angewandt. Zuerst wird eine Beschreibung der charakteristischen Eigenschaften sowie der Bedienung des e~-Detektors und des Choppers gegeben, die sich auch für weitere Experimente nützlich erweisen könnte. Für, von der Oberfläche reflektierte Projektil, wurde eine Streuverteilung mittels zweidimensional auflösenden Detektors in Koinzidenz mit der Anzahl emittierter Elektronen und dem Energieverlust des Projektils während der Streuung aufgenommen. Auf diese Weise war es möglich drei verschiedene Arten von Projektiltrajektorien zu unterscheiden und zu untersuchen: Projektil, die nicht in das Target eindringen und an der ersten Lage spekular reflektiert werden; Projektil, die in die Oberfläche eindringen und an den ersten Lagen darunter gestreut werden und den Kristall wieder verlassen, sowie Projektil, die tiefer in den Kristall eindringen. Es konnte gezeigt werden, dass Koinzidenzmessungen eine einzigartige Möglichkeit darstellen den Anteil der Potentialemission an der gesamten Elektronenausbeute zu ermitteln, auch wenn gleichzeitig ein beträchtlicher Anteil an, durch kinetische Energie angeregter, Elektronen vorhanden ist. Die Ergebnisse unterstützen vorhandene Konzepte für die Ladungsabhängigkeit von Potential- und kinetischer Emission aus LiF, die in Experimenten bei normalem Einfall der Projektil gemessen wurden und liefern weiters neue Informationen zur e"-Emission (potentiell und kinetisch) aus Isolatoren.

Im zweiten Teil wurde ein ähnlicher Aufbau verwendet um die streifende Streuung von neutralen H^o ($E = 300 \text{ eV} \dots 20 \text{ keV}$) an einer LiF(001) Oberfläche zu untersuchen. Mittels Messung von Flugzeitspektren in Koinzidenz mit der Zahl emittierter Elektronen konnten Elektronenemission und Anregungsphänomene nahe deren Schwellwerten untersucht werden. Die Ergebnisse können im Rahmen eines Modells von Zweierstößen der H^o mit F⁺ Gitteratomen, bei denen negative H^o als gemeinsame Vorstufe zur Anregung sowie zur Elektronen dienen, interpretiert werden.

Abstract

In the first part of this work an innovative electron detector geometry for measuring electron emission as well as projectile energy loss in grazing ion-surface collisions is described. This setup has been successfully applied in coincidence measurements of slow multiply charged ion-induced electron emission from a clean monocrystalline LiF surface at grazing incidence of the projectile ions. A description of the characteristic features and operation of the electron detector and the chopper-unit which may also prove useful in various other experimental situations is given. For projectiles reflected from the surface the scattering distribution has been recorded on a two dimensional detector in coincidence with the number of emitted electrons and the energy loss of the projectiles during scattering. In this way it was possible to distinguish and to investigate more closely electron emission for three different types of trajectories: non-penetrating projectiles specularly reflected from the topmost surface plane, projectiles entering the target and being reflected from subsurface layers and projectiles penetrating deeply into the target. It could be demonstrated that the coincidence technique is a unique tool to evaluate potential electron emission contribution even in the presence of a considerable number of kinetically excited electrons. The results support existing concepts on the charge state dependence of potential- and kinetic electron emission from LiF gained in normal incidence experiments and provide new information on the potential and kinetic electron emission from insulators.

In the second part a similar setup has been used to study neutral hydrogen atoms with energies ranging from about 300 eV to 20 keV are scattered from a clean and flat LiF(OOl) surface under grazing angles of incidence. By detection of time-of-flight(TOF) spectra in coincidence with the number of emitted electrons, electron emission and excitation phenomena near their respective thresholds were studied. The data are consistently interpreted in the framework of a binary collision model between hydrogen projectiles and F" lattice ions where the formation of negative hydrogen ions is the common precursor of electronic excitation of the target as well as electron emission.

Contents

Motivation	7
Part I:	
Electron emission and energy loss in grazing collisions of multiply charged ions with insulator surfaces	15
I.1. Introduction	16
I.2. Description of the experiment and its operation	17
I.2.1. Ion beam formation	17
I.2.2. Target preparation	21
I.2.3. Electron detection	23
I.2.4. Energy loss measurements	28
I.2.5. Electronics and Data Acquisition	34
I.2.6. Coincidence Measurements	37
I.3. Results and discussion	47
Part II:	
Electron emission and energy loss in grazing collisions of neutral projectiles with insulator surfaces	58
ILL Introduction	59
II.2. Description of the experiment	61
II.2.1. Experimental setup	61
II.2.2. Data acquisition	64
II.2.3. Data analysis	65
II.3. Results for HO on LiF	68
II.4. Results for He^0 on LiF	81
Summary	83
References	84
Danksagung	87
Lebenslauf	88

Motivation

Collisions of energetic heavy particles (atoms, molecules, ions) with solid surfaces are of great relevance because of important applications as, for example, plasma-wall interaction in gaseous discharges and thermonuclear fusion experiments, surface-analytics, -preparation and -modification, and for single particle detection schemes. Electron emission is a frequent consequence of inelastic ion-surface collisions and often accompanies other processes like projectile backscattering, - energy loss or sputtering. In basic studies of ion-surface collisions the emission of electrons therefore provides an important key for a detailed understanding of the underlying physical processes. In fig. M.1 the most relevant processes in ion-surface interaction can be seen.

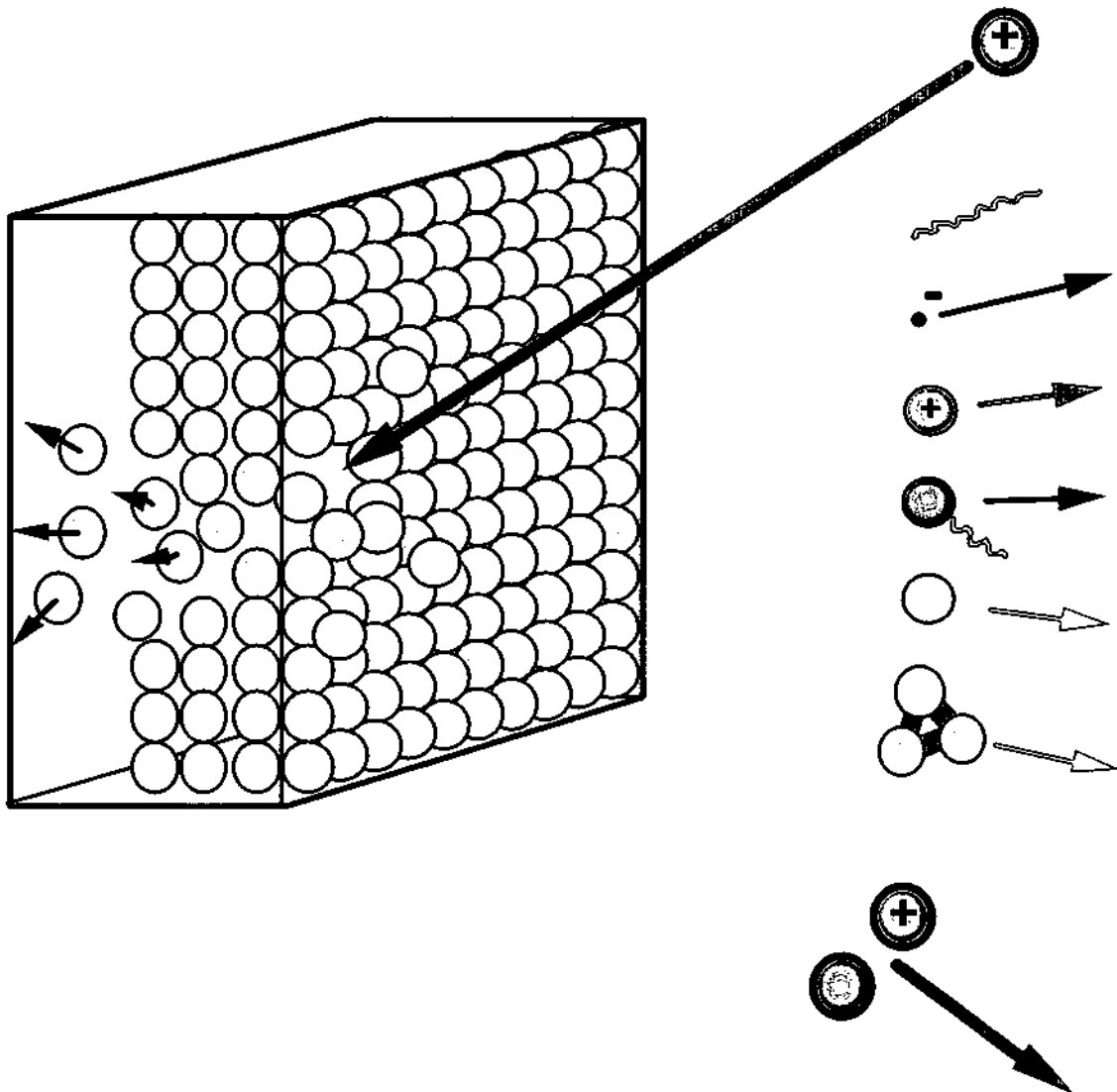


Fig. M.1: Processes occurring in ion-surface interaction.

Two main contributions to electron emission are commonly distinguished. Kinetic electron emission (KE) arises as a consequence of the momentum transfer from the (heavy) projectile (associated with its kinetic energy E_{kin}). Potential electron emission (PE) results from the conversion of internal energy E_{pot} initially stored in the projectile (e.g., excitation energy of metastable atoms, recombination energy of singly and multiply charged ions) via Auger-type processes. Both PE and KE processes can take place above an energy threshold related to the minimum energy Φ (surface work function) required to remove an electron from the solid surface. This implies a kinetic energy threshold for the occurrence of KE (center of mass energy $E_{cm} > \Phi$) and a potential energy threshold for PE ($E_{pot} > 2\Phi$).

PE and KE are therefore clearly separable in two limiting cases. For very slow projectiles with sufficiently large internal energy only PE can occur (e.g. for slow multicharged ions), while faster projectiles induce exclusively KE if their potential energy does not exceed 2Φ (e.g. this is the case for ground state neutral atoms or singly charged ions with sufficiently small ionization energy). Most investigations on electron emission in ion-surface collisions have so far concentrated on these two limiting cases. Review papers on "pure" KE have e.g. been published by Hasselkamp [1], Rosier and Brauer [2], and Baragiola [3]. Generally, KE processes are closely related to the inelastic energy loss (stopping power) of ions in the target bulk [3]. Several basic KE mechanisms have been identified. The most important ones concern direct binary collisions of the projectile with (quasi-free) target electrons, and electron promotion due to electron-electron interaction in quasimolecular collisions between the projectile and target atoms. Electrons of sufficient energy emitted due to these mechanisms as well as energetic target recoil atoms can cause additional production of secondary electrons. Recently a further mechanism specific for grazing collisions of keV singly charged ions with single crystal surfaces has been reported by Spierings *et al.* [4], where KE can be induced by the time - dependent perturbation of localized atomic electrons due to the fast distant passage of an incompletely screened charge.

PE in slow (multiply charged) ion - surface collisions, on the other hand, is a consequence of the decay of transiently formed "hollow atoms", a topic that has been extensively reviewed by Burgdörfer [5], Arnau *et al.* [6] and most recently by Winter

and Aumayr [7, 8]. The name for this exotic atom species refers to the fact that already at large distances in front of the surface electrons from the target are captured into highly excited (Rydberg) states of the projectile ion, whereas inner shells in first place remain empty. Subsequent deexcitation of such a short-lived multiply inverted complex via various electronic transitions (e.g. autoionization, Auger capture) leads to emission of a large number of electrons [9] ("above surface - PE"). Although the projectile is eventually fully neutralized, the kinetic energy gain due to the image charge acceleration before achieving this neutralization limits the available time interval between hollow atom formation and its impact on the surface to less than 100 fs. This is much shorter than the time necessary for a complete deexcitation of the hollow atom via a sequence of Auger processes. Close to the surface, valence electrons of the target will dynamically screen the ion charge thereby removing all loosely bound electrons from the projectile ("peel off; "at surface - PE") and destroying the hollow atom. Inner-shell vacancies, however, will predominantly be filled at and below the surface (via Auger capture from the disturbed conduction - or valence band, or via vacancy transfer in close collisions with target atoms). The resulting fast Auger electrons [10] may produce further slow secondary electrons ("below surface - PE") on their way through the target (alternatively, inner shell recombination may involve X-ray emission). A schematic illustration of the different mechanisms during interaction of a highly charged ion with a surface can be found in Fig. M.2. A review paper on collisions of atoms and ions with surfaces under grazing incidence has been published by H. Winter [11].

The majority of relevant investigations has been performed for conducting target surfaces, whereas very little is known about KE and PE from insulating targets. Kinetic electron emission yields arising from bombardment of insulators are generally found to be substantially larger than those from metal targets. In specific cases yields for insulators can be by one order of magnitude higher than those for metals, which makes insulator surfaces especially useful for applications in ion-electron converters or electron multipliers. Recent measurements in our group for normally incident singly (and multiply) charged projectiles on LiF [12] not only showed an enhancement of the total electron yield as compared to a clean Au surface, but also a threshold for (kinetic) electron production at a much lower impact energy than that for metal targets.

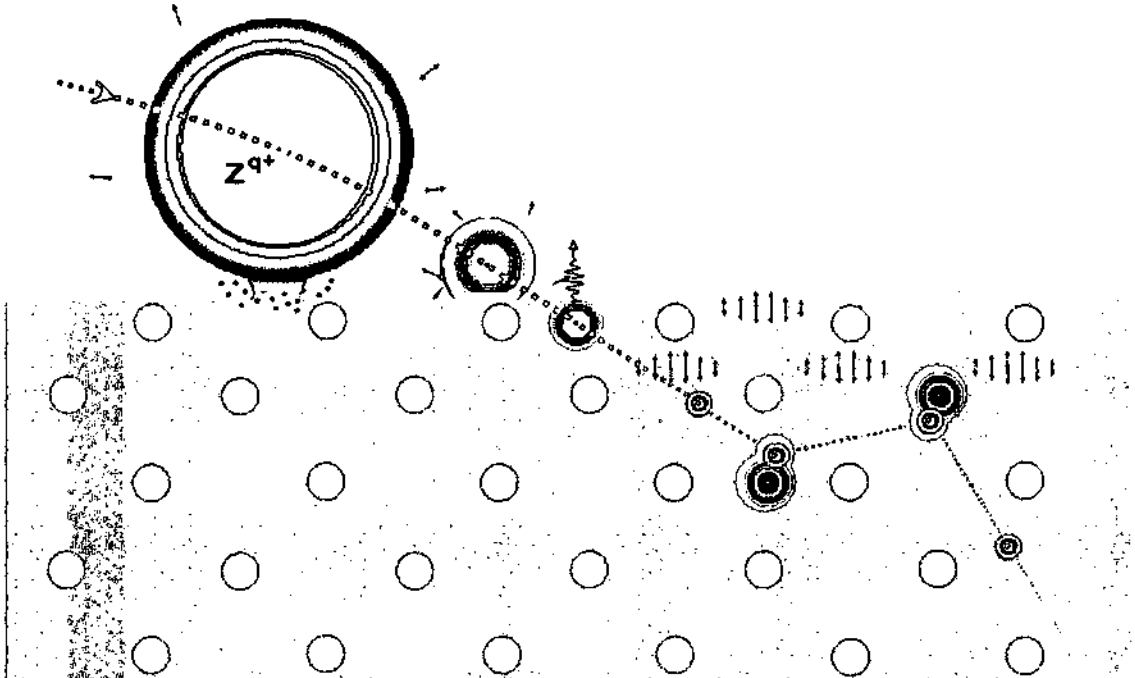


Fig. M.2: Schematic illustration of different mechanisms during interaction of a highly charged ion with a surface.

At a first glance, this experimental result for an insulator target was rather surprising, since valence electrons are more tightly bound in LiF than are conduction electrons in metals. In a qualitative explanation this finding was attributed to efficient electron emission via quasi-molecular autoionisation in collisions of the projectile with F⁻ at halogen lattice sites, and to the larger mean free paths of slow electrons in insulators than in metals. A quantitative calculation by Zamini *et al.* [13] based on electron promotion could reproduce the dependence of the electron yield on projectile energy.

Investigations with multiply charged ions are further complicated by the fact that both PE and KE will contribute to electron emission [14-16] and that at higher kinetic energies PE and KE might no longer be regarded as mutually independent. PE should be affected by the projectile velocity (e.g. via the available time in front of the surface for Auger type processes) [17], whereas KE can be influenced by the (pre - equilibrium) charge state of the projectile [15]. In particular, alkali halide targets show a dependence of KE on the projectile charge state [12, 18]. A complete picture of the interrelation of PE and KE and of the connection between electron emission and energy loss in this

regime is still missing. To gain such information especially for the case of insulating targets was the subject of the present thesis. The energy regions for investigation of potential and kinetic energy dominated processes can be seen in Fig. M.3.

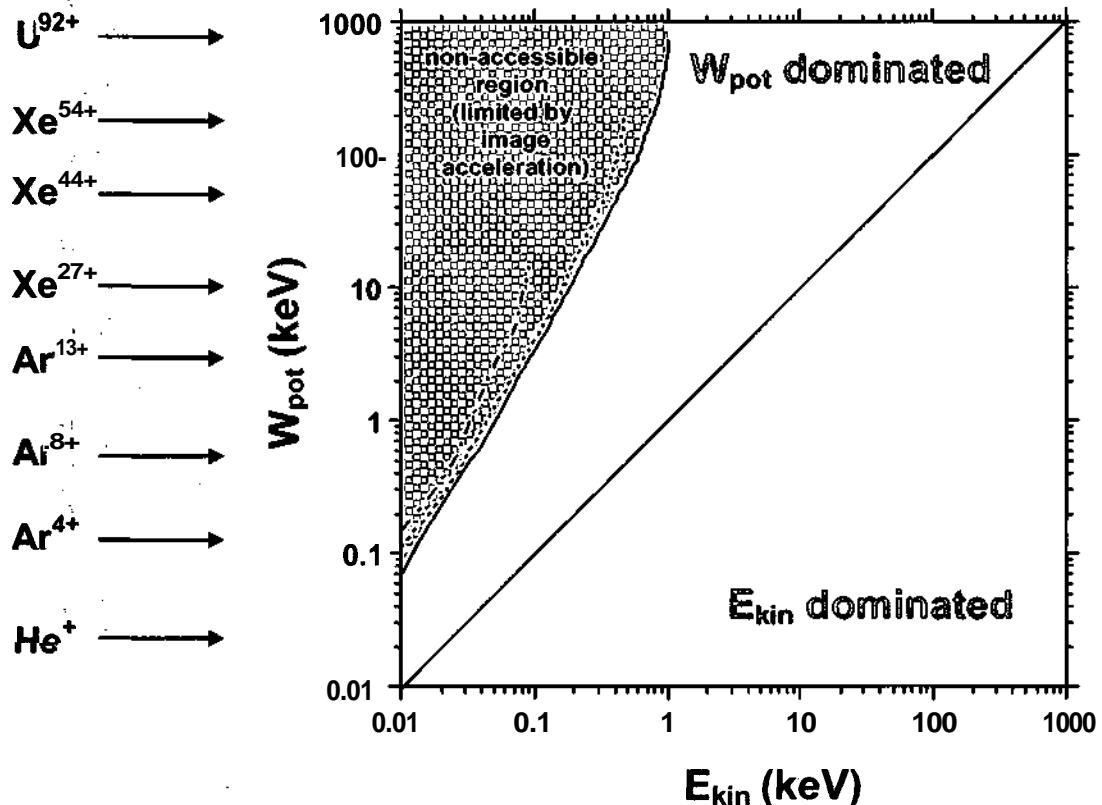


Fig. M.3: In region where E_{kin} is larger than the potential energy W_{pot} the interaction is dominated by the projectile's kinetic energy and vice versa. Due to image charge acceleration it is not possible to reach very low kinetic energies for high potential energies (yellow area).

In this thesis we investigate some novel aspects of ion-induced electron emission as well as excitation mechanisms of insulator surfaces. In part I we will present our studies on electron emission and projectile energy loss induced by multiply charged ions and discuss the role of the projectile charge state in the interaction with a LiF(001) surface. Studies on electron emission induced by neutral hydrogen and helium atoms on a LiF (001) surface under surface channeling scattering conditions are presented in part II.

Some parts of the here presented work have already been published in scientific journals:

- A. Mertens, S. Lederer, K. Maass, H. Winter, **J. Stöckl**, HP. Winter, and F. Aumayr
Excitation vs. electron emission near the kinetic thresholds for grazing impact of hydrogen atoms on LiF(OOl)
Physical Review B **65**, 132410 (2002)
- **J. Stöckl**, HP. Winter, F. Aumayr, S. Lederer, A. Mertens, K. Maass and H. Winter
Formation of surface excitons and electron emission during grazing impact of hydrogen atoms on LiF(OOl)
Nuclear Instruments and Methods in Physics Research Section B: Beam Interactions with Materials and Atoms **193**, 645 (2002)
- A. Mertens, K. Maass, S. Lederer, H. Winter, H. Eder, **J. Stöckl**, HP. Winter, F. Aumayr, J. Viefhaus and U. Becker
Studies on electron emission during grazing impact of keV-hydrogen atoms on a LiF(OOl) surface via translational spectroscopy
Nuclear Instruments and Methods in Physics Research Section B: Beam Interactions with Materials and Atoms **182**, 23 (2001)
- **J. Stöckl**, C. Lemell, HP. Winter, and F. Aumayr
Electron Emission in Grazing HCl-LiF(001) Collisions
Physica Scripta **T92**, 135 (2001).
- C. Lemell, **J. Stöckl**, J. Burgdörfer, G. Betz, H. P. Winter, and F. Aumayr
Coincidence measurements of highly charged ions interacting with surfaces
AIP Conf. Proc. **500**, 656 (2000)

- C. Lemell, J. Stöckl, J. Burgdörfer, G. Betz, HP. Winter, and F. Aumayr
Coincidence measurements of highly charged ions interacting with a clean Au(111) surface
Physical Review A 61, 012902 (2000)
- C. Lemell, J. Stöckl, HP. Winter, and F. Aumayr
A versatile electron detector for studies on ion-surface scattering
Review of Scientific Instruments 70, 1653 (1999)

Part I:

- Electron emission and energy loss in grazing collisions of multiply charged ions with insulator surfaces

I.1. Introduction

Collisions of energetic particles (electrons, atoms, molecules, ions) or photons with atoms, molecules, clusters, and solid surfaces are of frequent experimental interest. In pertinent studies the emission of slow electrons often provides one of the keys toward a detailed understanding of the underlying physical processes.

Slow electron emission may be studied with regard to respective absolute total yields, energy and angular distributions, and combinations thereof. In particular, ion-induced electron emission from solid surfaces is of considerable principal and practical interest in modern surface physics and analytics, and also for various plasma based applications. Such electron emission processes are closely related to the inelastic energy loss of ions scattered off the surface (e.g., Ref. [6] refs therein). A more detailed understanding of such inelastic interactions may be achieved if trajectories of the scattered ions are well defined, as is the case in grazing incidence scattering geometries [19] and, moreover, when studying the scattered ions (time-of-flight and scattering angle) and emitted electrons in coincidence [20]. Such an experiment has been carried out for scattering of slow multiply charged Ar ions with various energies on a clean monocrystalline LiF (001) surface, with electrons emitted from the latter detected in coincidence with the scattered projectiles [21]. To this purpose a novel electron detector geometry has been built in order to determine the number of ejected electrons [so called electron statistics (ES)], from which precise totals electron yields can be derived. We have applied this electron detector for coincidence measurements with regard to angular-, charge-, and energy (time-of-flight) distributions of scattered projectiles, as will be described below.

I.2. Description of the experiment and its operation

I.2.1. Ion beam formation

The experiment has been designed for and installed at the 5 GHz electron cyclotron (ECR) ion source facility at TU Wien [22]. A schematic drawing of the ion source is shown in fig. 1.1. The confinement of the plasma is realized by means of a variable axial magnetic mirror field (up to 0.5 T) and a radial permanent hexapole field (NdFeB). A biased disk serves as electron emitter, which enhances the fraction of ions in higher charge states. A microwave power of up to 1 kW is delivered from a 5 GHz klystron driven by a tunable microwave oscillator.

The ion source was developed for producing multiply charged ions from gas phase atoms or molecules. High purity gases in compressed gas bottles can be mounted on the gas inlet whose gas flux is controlled by an automatic valve. Depending on the desired charge state the gas pressure in the plasma vessel can be varied from $2 \cdot 10^{-6}$ - $5 \cdot 10^{-5}$ mbar.

Because the beam line was left on ground potential the ion source had to be operated on a positive high voltage. The ion source provided projectile ions with energies

$$E_{kin} = (U_{extr} + U_{Plasma}) \cdot q \quad (1.1)$$

where U_{extr} is the extraction voltage ($U_{extr} \leq 10$ kV), U_{Plasma} the plasma potential ($U_{Plasma} \ll 100$ V), and q is the ion charge state. Formation of the extracted ion beam is achieved by an accel-decel configuration and a magnetic quadrupole doublet. The so focused beam, was then mass to charge analyzed in a sector magnet, and transported to a differentially pumped ultrahigh vacuum (UHV) chamber ($p - 10^{-10}$ mbar). A typical ion mass spectrum for Ar used as the ion source gas can be seen in Fig. 1.2.

The mass selected incident ion beam was collimated to 1 mm in diameter and directed into the chopper chamber. The deflected (chopped) beam was again collimated to 1mm in diameter and led onto a LiF(OOL) single crystal target which was mounted on

a manipulator that allows to adjust the ion impact angle ψ_{nom} as well as the azimuthal angle ϑ (crystallographic orientation). Projectiles scattered from the target (around the surface channeling direction) detected on a position sensitive multichannel plate (MCP) equipped with a 2-dimensional wedge&strip-anode which allows to measure the scattering distribution. A pumping scheme can be found in Fig. 1.3 [23, 24]; a schematic view of the beam line in Fig 1.4.

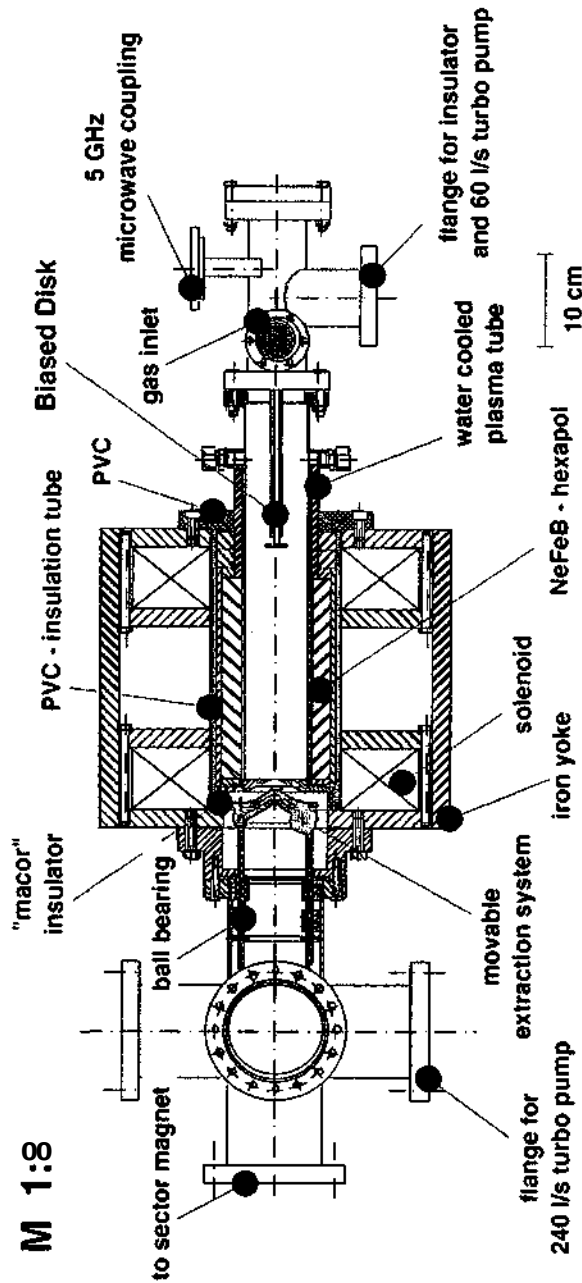


Fig. 1.1: 5 GHz ECR-Ion-Source BERTA.

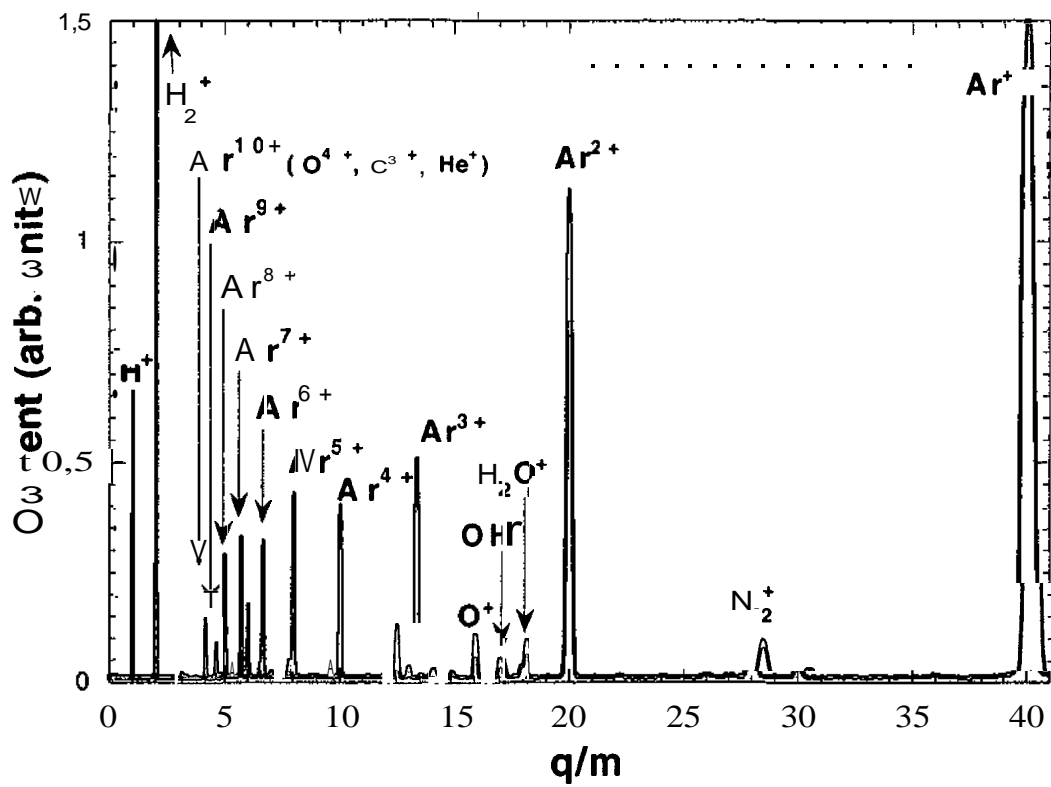


Fig. 1.2: Typical ion mass spectrum for Ar used as the ion source gas.

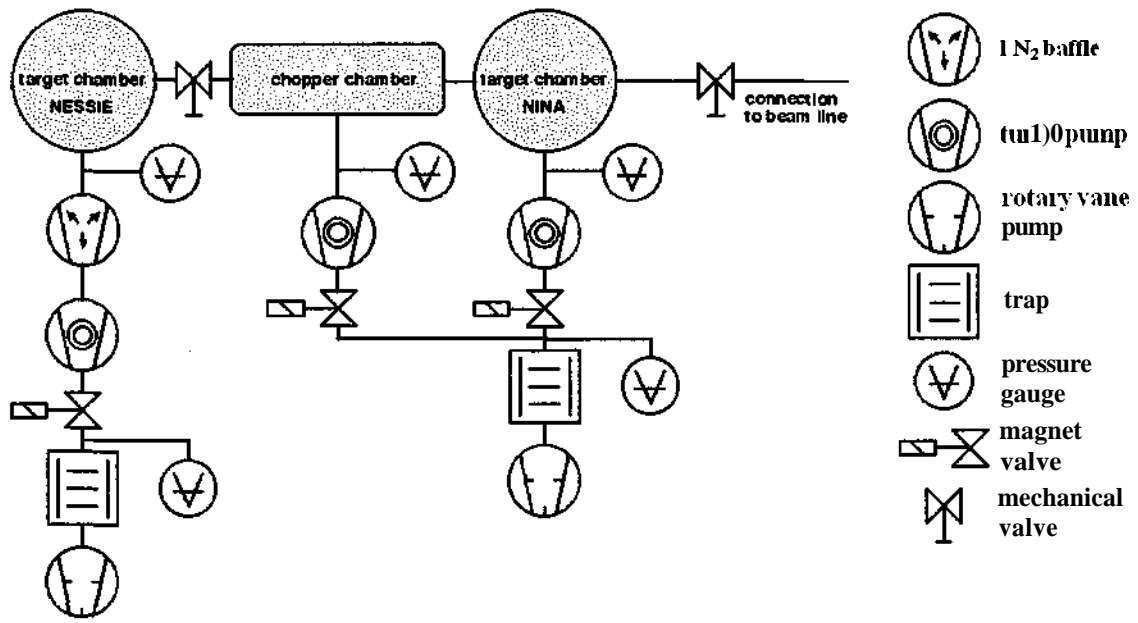


Fig. 1.3: Pumping scheme of the beam line.

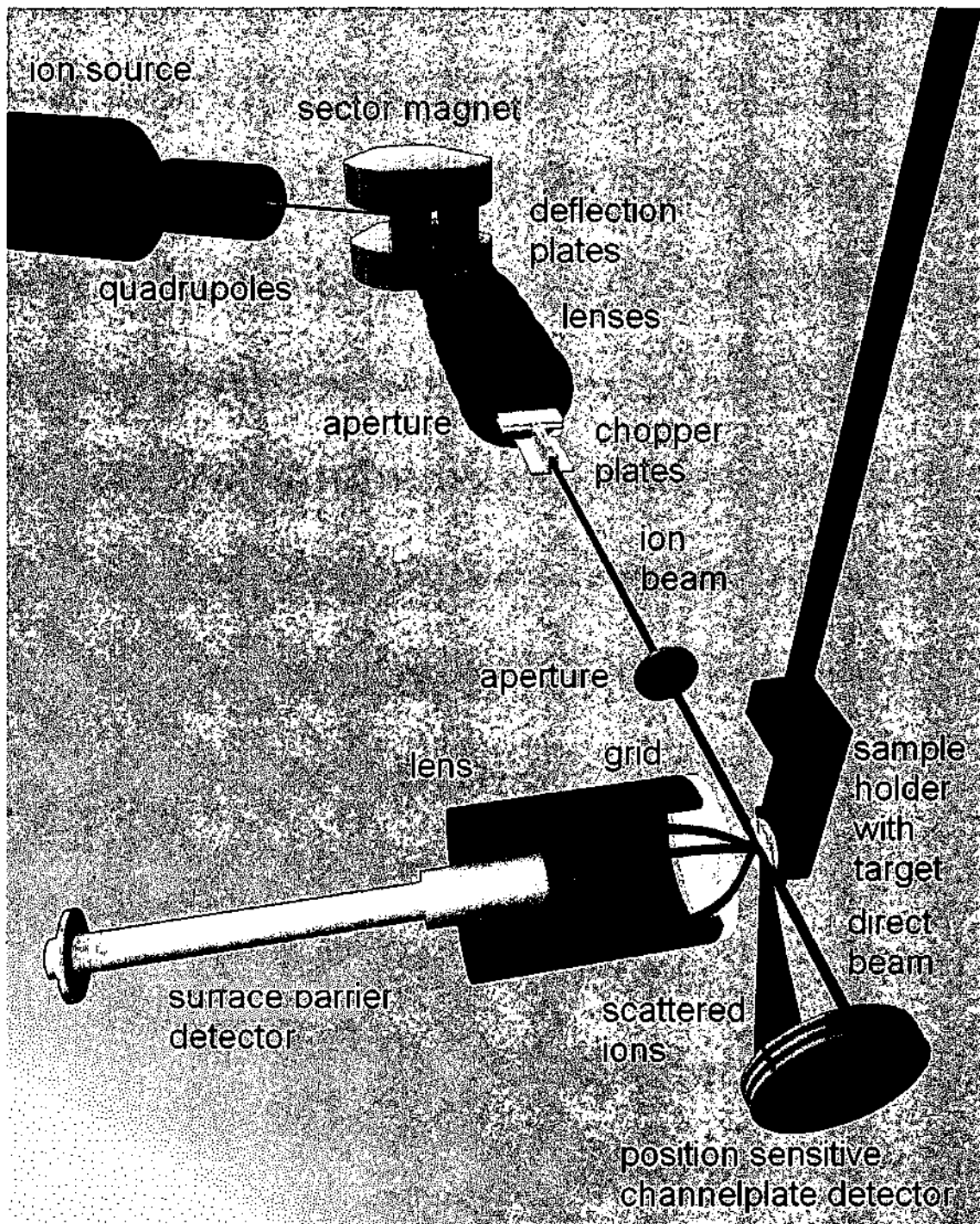


Fig. 1.4: Beam line (schematic) of the coincidence experiment NESSIE (New Experiment on Solid Surfaces Involving e^- -Emission).

I.2.2. Target preparation

In this thesis a LiF (001) single crystal was used as a target. LiF is an ionic insulator (fig. 1.5) which differs substantially from a metal surface. Its small valence band is fully occupied. The electrons in the valence band are rather localized near the halide sites (ionic binding). The binding energy for LiF is $E_b \sim 12$ eV (fig. 1.6). The unoccupied conduction band lies energetically about 2 eV above the vacuum level. The band gap, which is characteristic for insulators, is therefore 14 eV. The crystal structure consists of two face-centered cubic lattices -the so called NaCl (B1) structure (Pearson: cF8) — with a basis of $a = 7.6$ a.u. [25].

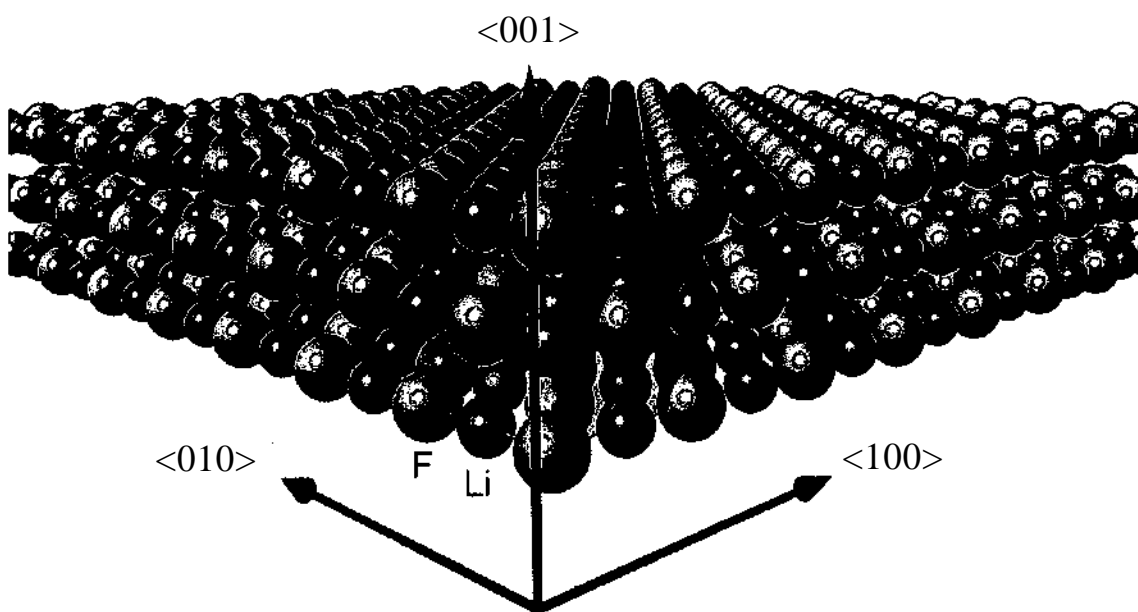


Fig. 1.5: LiF crystal (schematic) with the (001) surface on top. Li^+ ions are indicated red, F^- ions are shown in blue. The transparent cube marks a unit cell ($a = 7.6$ a.u.).

The target was prepared by annealing for about 90 minutes at about 400°C. During the measurements the target was kept at an elevated temperature of about 200°C,

where the ionic conductance of LiF is high enough to prevent macroscopic charging-up of the sample, while the microscopic situation during single impact events (e.g. local charging-up via electron extraction from the surface) is not affected. It is well known that ion-induced electron emission from single crystals shows a strong dependence on the azimuthal orientation of the target surface with respect to the ion beam direction [11, 26]. The results in this thesis have been obtained for a fixed azimuthal angle of 13° with respect to the $\langle 100 \rangle$ direction on the surface plane and are therefore characteristic for a "random" orientation of the LiF crystal. A schematic picture of a LiF crystal can be seen in Fig. 1.5. The band structure of LiF is shown in Fig. 1.6.

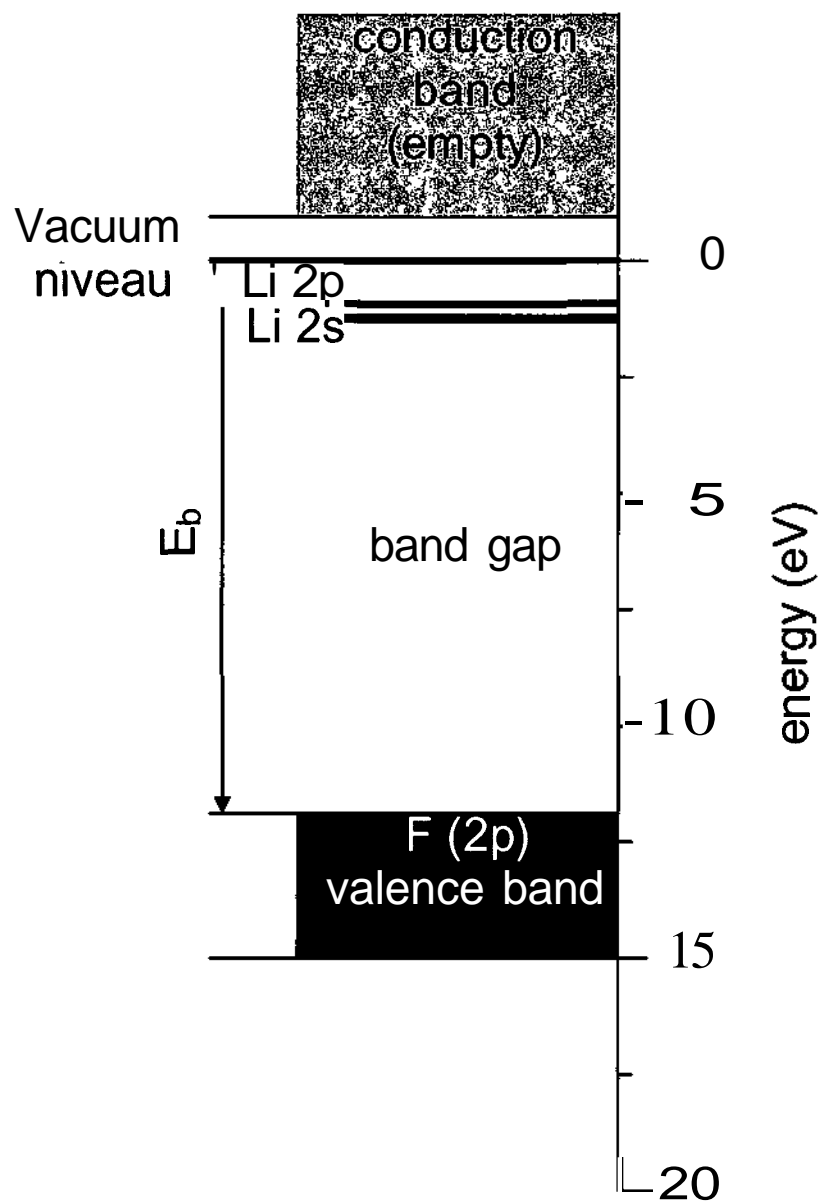


Fig. 1.6: Band structure of LiF (schematically).

I.2.3. Electron detection

Electrons emitted from the ion-surface interaction region were extracted by a weak electric field owing to a bias of some 10 V applied to a highly transparent grid about 1 cm in front of the target. This grid shields the adjacent high electric field from the +25 kV bias of a surface barrier detector (SBD; Canberra PD 100-12-300 AM-HT) which post-accelerates the extracted electrons. Fig. 1.7 shows ray-trace calculations performed for our geometry with the program MacSIMION which showed that an electric field of about 100 V/cm is sufficient to collect all electrons with energies below 50 eV emitted into the solid half angle. The extraction field, however, also influences the trajectory of incoming (slow) ions. This influence results in a slightly larger impact angle $\psi = \psi_{\text{nom}} + \Delta\psi$ (in ion-surface experiments $\Delta\psi$ includes the deflection due to the interaction of the incoming ion with its own image charge) [27, 28] and a deflection of the direct beam which has to be taken into proper account.

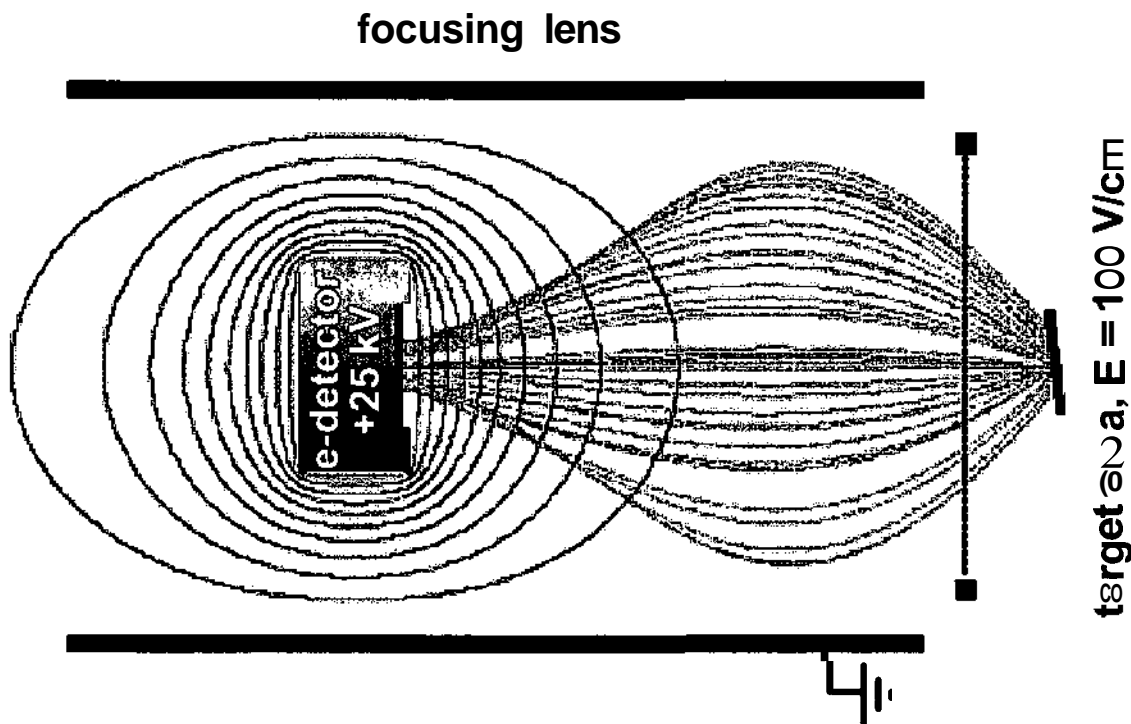


Fig. 1.7: Calculated potential distribution and resulting electron trajectories for an electric field of 100 V/cm in the target area. The electron detector is biased at +25 kV.

For a LiF surface the energy gain E_{im} due to the ion's image charge was experimentally determined (for a grazing incidence geometry similar to ours) to be

$$E_{im}(\text{eV}) = 1.10 \cdot q^{1.42}, \quad (1.2)$$

where q is the charge state of the incident ion (see Fig. 1.8) [29].

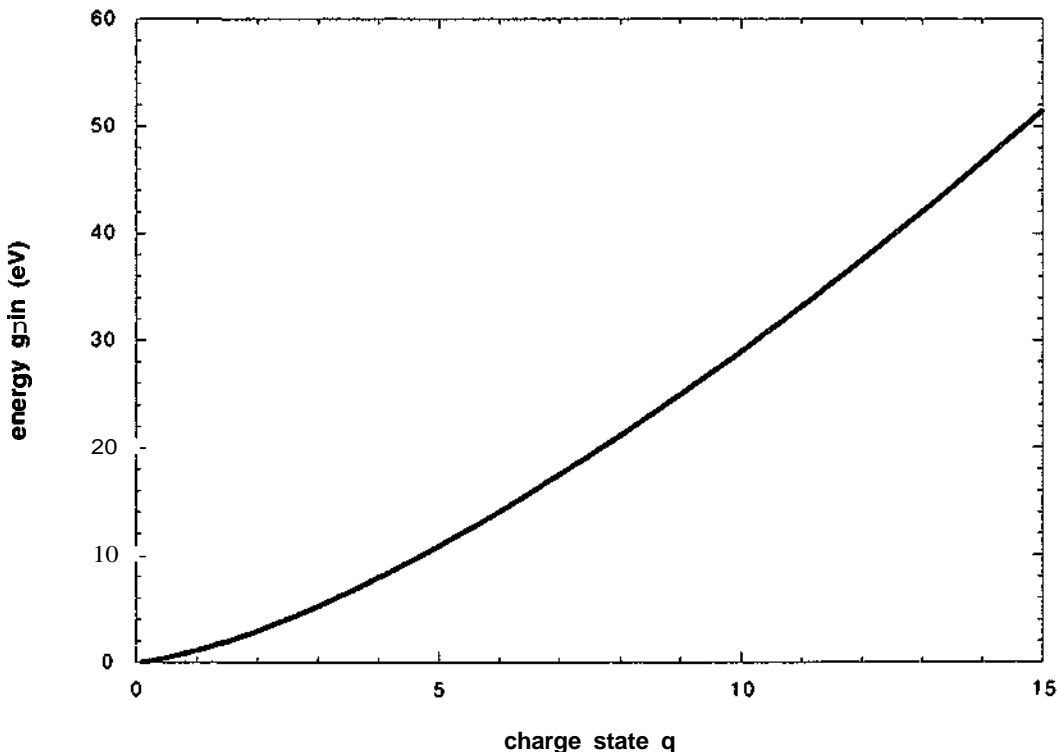


Fig. 1.8: Energy gain due to image charge acceleration for grazingly incident ions on a LiF(OOL) surface (from [29]).

Measurements of the resulting displacement on the position sensitive ion-detector compare well with calculations and MacSIMION simulations.

If only the electron detector is operated, our setup allows measuring electron statistics (ES) spectra for a variety of impact angles ψ ranging from almost 0° to more than 50° . For larger impact angles the applied extraction field is no more sufficient to collect all emitted electrons and hence measured yields become too low.

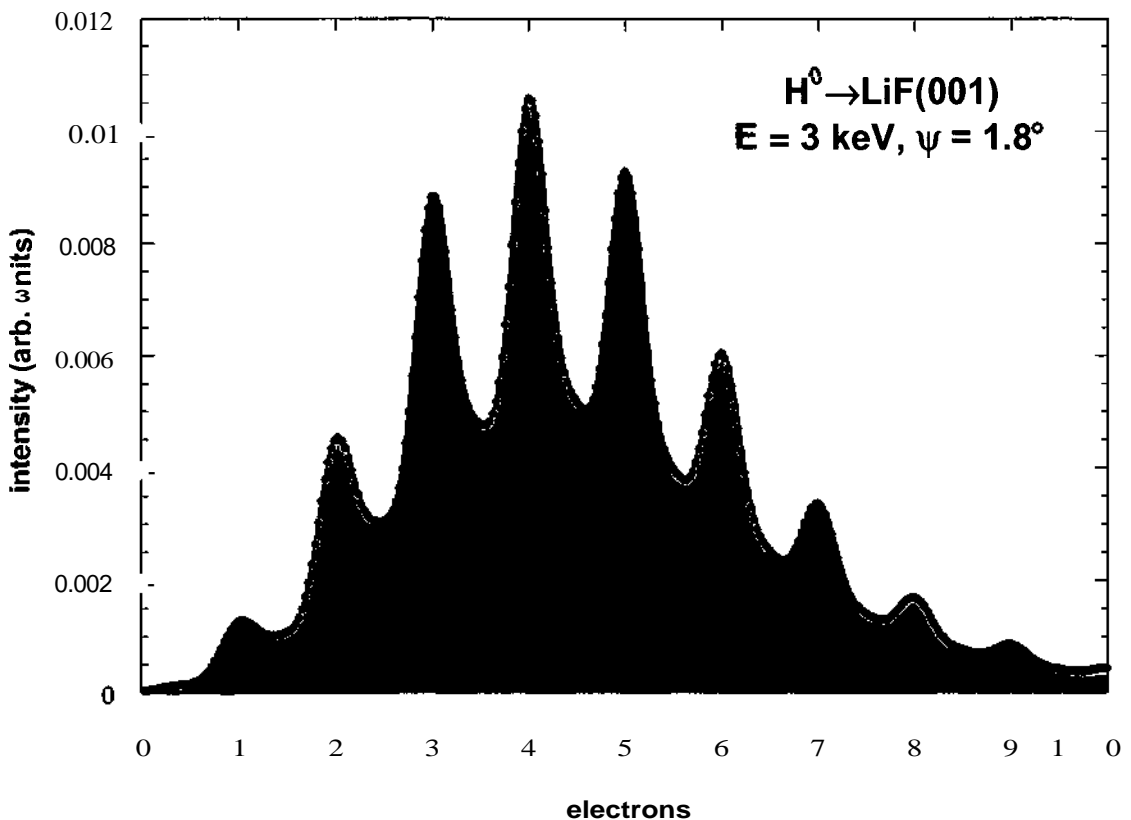


Fig. 1.9: Electron multiplicity spectrum for 3 keV H° atoms impinging on clean $\text{LiF}(001)$. Measured data are represented by symbols; the shaded areas are results of a fitting procedure (see the text). The area corresponding to the n th peak is directly related to the probabilities W_n for emission of n electrons.

The number of electrons emitted due to a particular ion impact event [the electron number statistics (ES) which gives access to the total electron yield % see below] is deduced from the detectors pulse height distribution [see fig. 1.9 for the example of an electron multiplicity spectrum induced by 3 keV H° atoms impinging on clean $\text{LiF}(001)$ - therefore explanations given here are also valid for part II] in the following way. Electron emission induced by a single projectile will be finished within less than 10^{-11} s, which is much shorter than the time resolution of the applied detector electronics ($\geq 10^{-9}$ s). Thus, n electrons emitted due to a particular ion impact will be registered like one electron of $n \times 25$ keV rather than as n individual 25 keV electrons. Consequently, the areas C_n (i.e., the integrated count numbers) below the n th peak (colored areas in fig. 1.9) of the resulting ES are directly related to the probabilities W_n .

for emission of n electrons. The shape of these shaded areas in fig. 1.9 stems from the fact that some electrons are backscattered from the detector and thereby depositing only a part of their energy into the latter. If negative secondary ions are emitted from the impact region, they would only cause a broad and unstructured background to the ES spectrum due to the limited energy resolution of the surface barrier type detector for heavy particles (and also reach the detector much later than the electrons). More details on the ES detection method can be found in earlier publication [30-32]. The following equation gives the simple relation between the individual probabilities W_n and the total electron emission yield γ which is defined as the mean number of electrons emitted due to impact of one projectile:

$$\gamma = \sum_{n=1}^{\infty} n \cdot W_n \quad (1.3)$$

$$\sum_{n=0}^{\infty} W_n = 1 \quad (1.4)$$

The probability W_0 for emission of no electron cannot be determined directly, but becomes sufficiently small to be safely neglected for yields $\gamma \geq 3$. Probabilities W_n for emission of n electrons calculated for the spectrum in Fig. 1.9 can be seen in Fig 1.10.

Probability spectra are usually fitted by binomial, poison, or polya distributions. For Ar ions impinging on LiF one usually measures yields $\gamma \geq 10$ and the envelope of the spectra can be fitted using a Gaussian distribution. Using the mean value γ_{Gauss} one can calculate the yield for electron emission via

$$\gamma = 1.07 \cdot \gamma_{Gauss} \quad (1.5)$$

This relation was derived by Kurz [33].

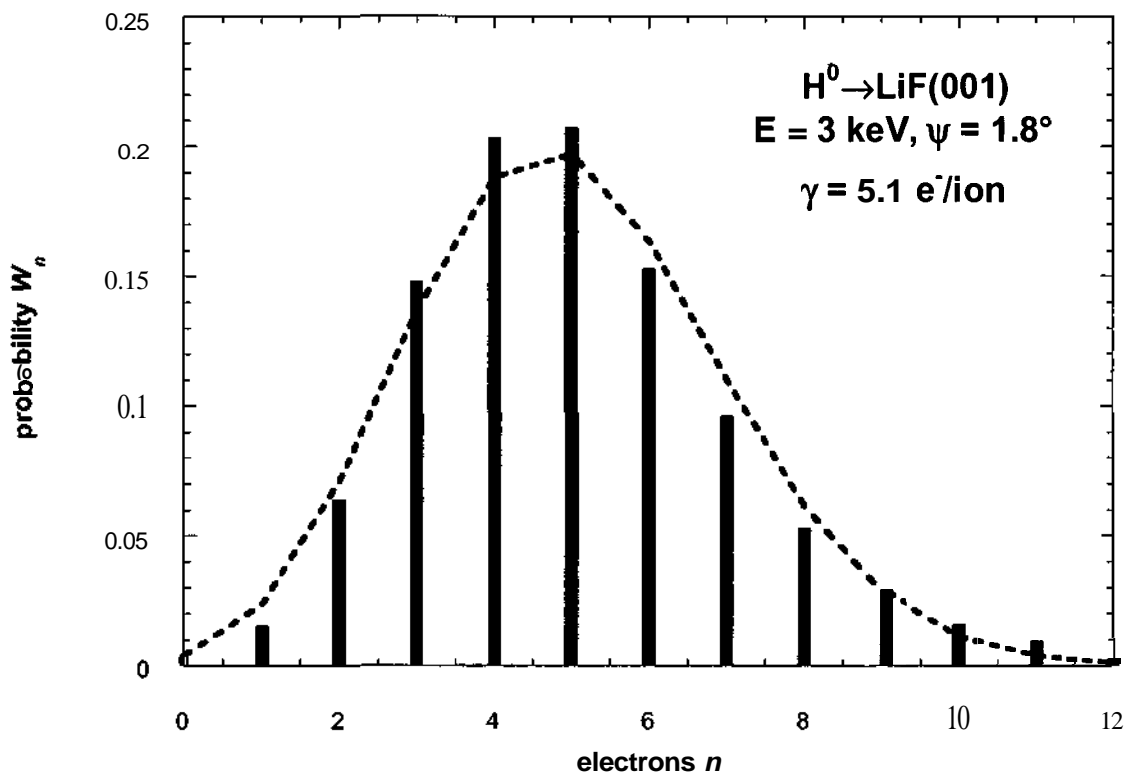


Fig. 1.10: Probabilities W_n for emission of n electrons calculated for the spectrum in fig. 1.9 for 3 keV H^0 atoms impinging on clean LiF(001). The dashed line indicates a binomial distribution fitted to the data (see text).

1.2.4. Energy loss measurements

For the measurement of the projectile time-of-flight (TOF) an electrostatic beam chopper built at the University of Linz/Austria [34, 35] has been installed at our beamline. This device deflects the ion beam periodically and sweeps over an aperture once a cycle to allow ions to hit the target. On the average less than one ion (~ 0.1) passes through the aperture per chopper cycle to allow an exact measurement of the time-of-flight. The chopper can be operated at a variable frequency (25 - 250 kHz) to adjust the count rate in the experiment and was originally designed for Protons with an energy $5 \text{ keV} < E < 150 \text{ keV}$.

When entering the chopper chamber the beam is collimated by two apertures (0.3 mm, and 0.1 mm; 1.5 cm apart) and passes two pairs of parallel plates ($/ = 50 \text{ mm}$ for y-axis and $/ = 60 \text{ mm}$ for x-axis) which can be polarized with voltages up to 400 V. In this setup the target beam line is turned by 1.5° in the x-z-plane out of the central line to obtain a rather clean ion beam (i.e. free of neutrals and charge-exchanged species). Between two chopper cycles the beam is deflected in y-direction ($V_x = 0 \text{ V}$, $V_y = -V$). When a cycle starts the beam will also be deflected in x-direction ($V_x = +V$, $V_y = -V$). Afterwards the polarization of the x-plates is reversed and the beam sweeps over an aperture (105 cm distance from the deflection plates) within 0.5 ns and ions can pass through to hit the target. The cycle is completed by grounding the x-plates and putting the y-plates on $V_y = -V$ immediately afterwards (Fig. 1.11).

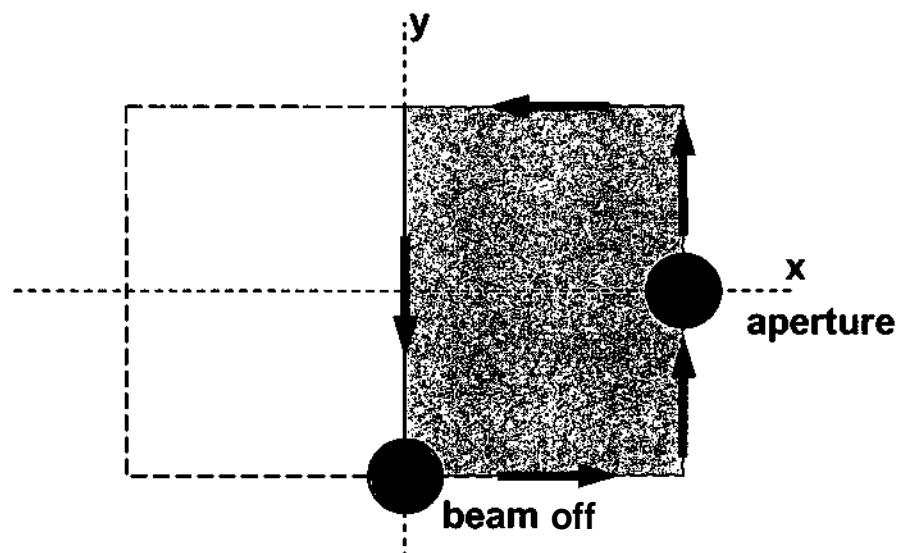


Fig. 1.11: Chopper cycle (schematic) as seen in beam direction.

Fig. 1.12 shows a typical TOF spectrum for Ar^{3+} ($E = 18$ keV) on $\text{LiF}(001)$ as measured with this setup with an arbitrary time scale (channels). The direct peak (left) as well as the TOF distribution of the scattered ions can be seen in this plot. The time-of-flight t of the ions from the detector is given by

$$t = \frac{x}{v} \quad (1.6)$$

where x is the distance from the target to the position where the ion hits the position sensitive detector and v is the velocity of the ion.

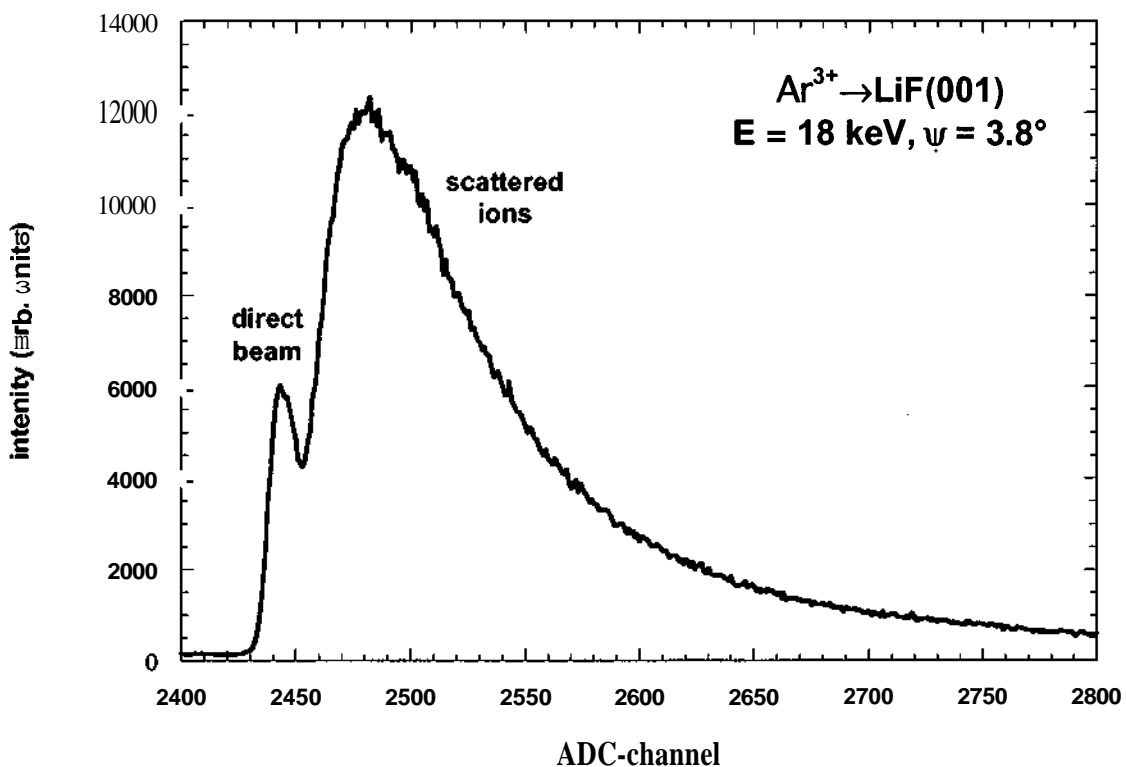


Fig. 1.12: Time-of-flightintensity vs. ADC-channel-number for 18 keV Ar^{3+} ions on $\text{LiF}(001)$. The left peak indicates the time-of-flight of the unscattered (direct) beam. The broad distribution corresponds to scattered ions.

ADC-channels can be transformed into a real TOF scale when considering the fact that the direct beam suffers no energy loss. The time t_0 is the flight time of the direct beam from the target to the detector and is therefore

$$t_0 = \frac{x_0}{v_0} \quad (1.7)$$

where x_0 is the distance from the target to the ion detector perpendicular to the MCP surface and v_0 the initial velocity of the ions:

$$v_0 = \sqrt{\frac{2E_0}{m}} \quad (1.8)$$

$$t_0 = \frac{x_0}{\sqrt{\frac{2E_0}{m}}} \quad (1.9)$$

using the ion mass m and the initial energy E_0 .

The ADC channel number c then transforms into a time scale by

$$t = t_0 + (c - c_0)\Delta t_c \quad (1.10)$$

where c_0 is the channel number of the direct beam and Δt_c is the time per channel of the time-to-amplitude conversion and the ADC (determined by a precise "delay" experiment). A such transformed TOF spectrum can be seen in fig. 1.13.

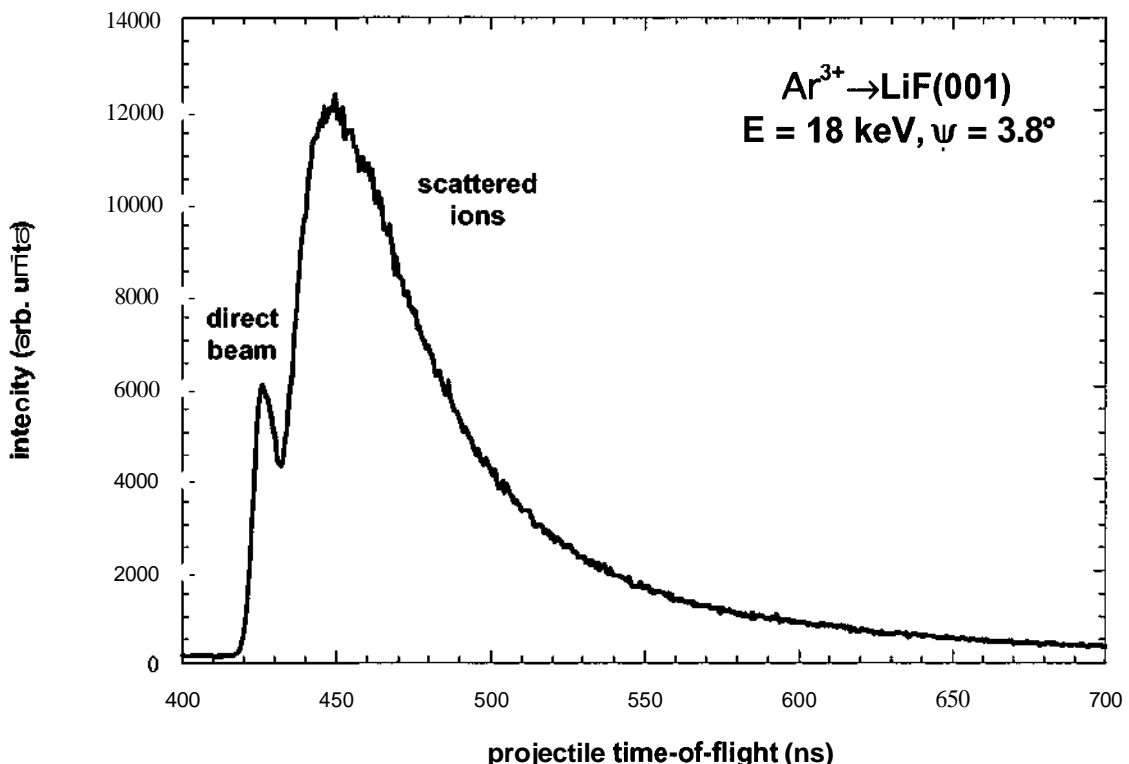


Fig. 1.13: Projectile time-of-flight spectrum for 18 keV Ar^{3+} ions on LiF(OOI) .

However, as shown in fig. 1.14 the distance for ions scattered from the surface is longer than x_0 and given by:

$$x = \sqrt{x_0^2 + \Delta y^2 + \Delta z^2} \quad (1.11)$$

where Δy and Δz are the distances from the position the direct beam hits the microchannel plate (MCP) to the position where the ion is actually detected.

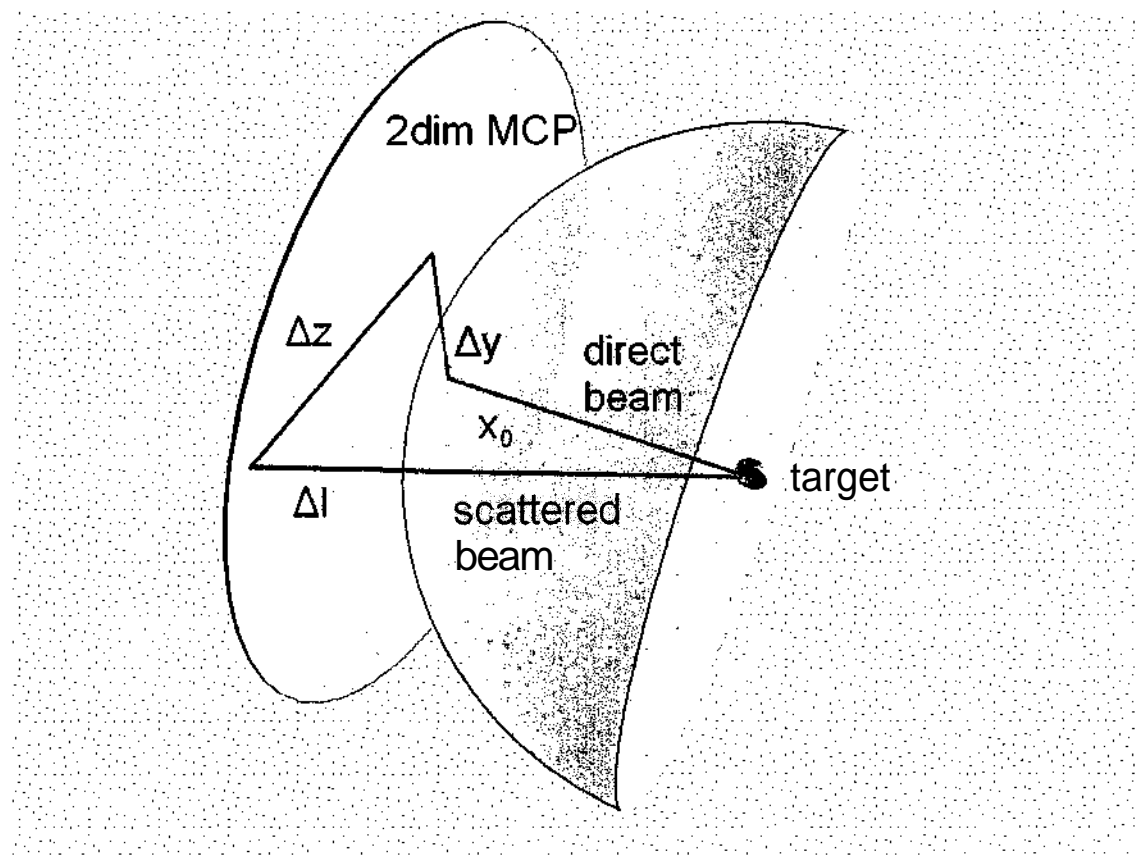


Fig. 1.14: Distances (schematically) in the coincidence experiment NESSIE. The sphere around the target marks the length x_0 .

Consequently, in a next step the recorded flight times t are transformed into "normalized" flight times t_n as if they all would have traveled equal distances of x_0 :

$$t_n = t \frac{x_0}{x} \quad (1.12)$$

$$v_n = \frac{x_0}{t_n} \quad (1.13)$$

This transformation, however, requires the knowledge of the impact coordinates (Ay, Az) of the scattered ion beam on the channelplate detector and has to be applied for each scattering event individually.

The energy loss E_{loss} is consequently given by

$$E_{loss} = E_0 - E = E_0 - \frac{m}{2} v_{\perp}^2 = E_0 - \frac{m}{2} \frac{x_0^2}{t_n^2} \quad (1.14)$$

The non-linear transformation of a TOF spectrum $f(t)$ into an energy loss spectrum $\tilde{f}(E)$ has to fulfill the requirement

$$\int f(t) dt = \int \tilde{f}(E) dE. \quad (1.15)$$

Therefore the transformation can be written as

$$\tilde{f}(E(t)) = f(t) \frac{1}{dE/dt}. \quad (1.16)$$

Using equ. (1.14)

$$\frac{dE_{loss}}{dt} = m \frac{x_0}{t^3} \quad (1.17)$$

one finds the transformation

$$\tilde{f}(E_{loss}(t)) = \frac{f(t)t^3}{mx_0}. \quad (1.18)$$

In fig. 1.15 the TOF spectrum from fig. 1.13 has been transformed into a corresponding energy loss spectrum as described above.

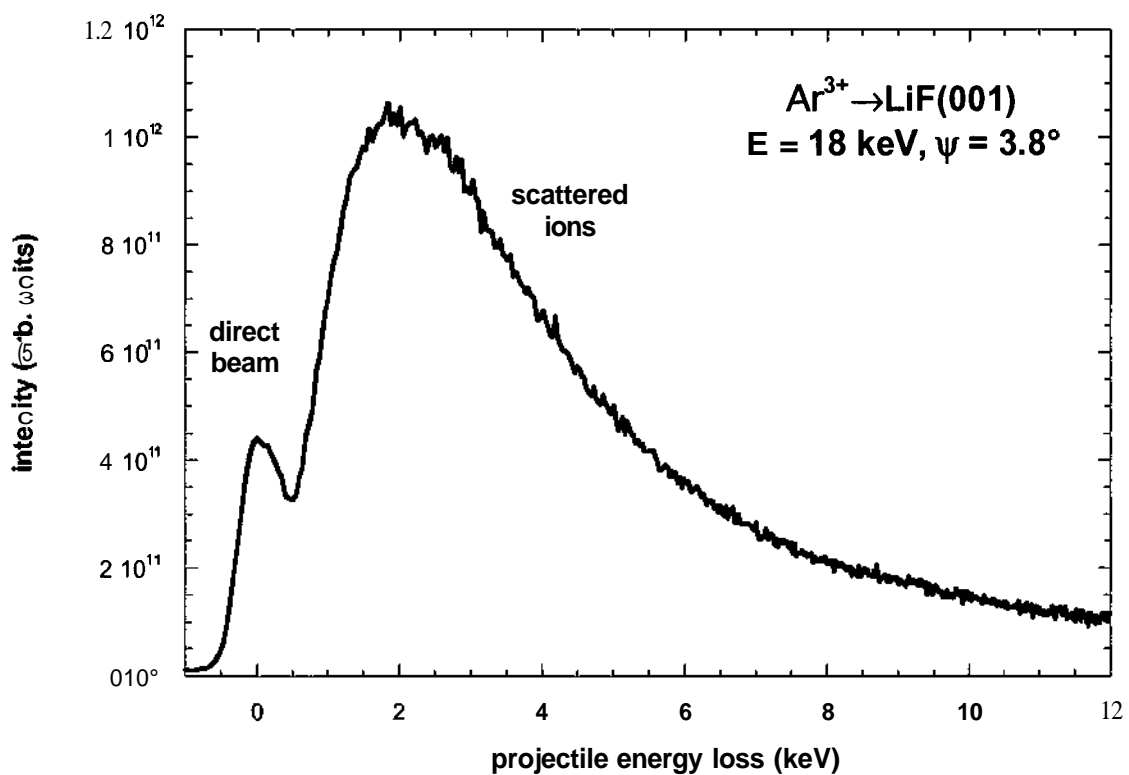


Fig. 1.15: Projectile energy loss spectrum for $18 \text{ keV} \text{ Ar}^{3+}$ ions on LiF(OOI) .

I.2.5. Electronics and Data Acquisition

In the following section the electronics of the experiment as well as the method of data acquisition are explained. A scheme of the electronics can be found in fig 1.16.

I.2.5.1. Electron signal

The outgoing charge pulse of the PIPS-detector is pre-amplified (ORTEC 142B) and transformed in an amplifier (ORTEC 570) to an analog output pulse (0 - 10 V) which is proportional to the deposited energy (and therefore the number of electrons). As the detector is kept on high voltage (+25 kV) the signal is transformed to ground potential via a self-built signal transformer. Afterwards the signal is led into the analog-digital-converter (ADC) unit (Kmax MiniCrate) to be recorded for later evaluation.

I.2.5.2. Ion signal

The 3 (position related) signals of the wedge&strip-anode (2-dim. readout of the microchannelplate detector in chevron configuration) are led into the 3-way-preamplifier (ROENTDEK), then amplified (ORTEC 570) and also recorded by the ADC-unit.

I.2.5.3. Gate-generation for coincidence measurements

The busy-output of the amplifier of the electron-branch is connected to a gate&delay-generator (ORTEC 416A). The generated gate-signal is delayed, transformed into an optical signal, and brought to ground potential via fiber optics. The busy output of one of the ion signal amplifier's is combined with the electron gate via a logical OR which gives the state 1 when either an electron or an ion is detected. The so derived signal is used to gate the ADC-unit.

I.2.5.4. Time-Of-Flight signal

The chopper unit puts out a time delayed standard NIM-output which is connected to the start-input of a time-to-amplitude-converter (TAC; ORTEC 584). The timing output of a preamplifier of the ion-branch is amplified with a timing filter

amplifier (ORTEC 474) and transformed to a standard NIM-pulse with a constant-fraction-discriminator (ORTEC 584). This pulse is used as the stop signal for the TAC. The TAC then generates an output pulse proportional to the measured time between start and stop which is also recorded by the ADC unit.

I.2.5.5. Data acquisition

The gate created with the logical OR triggers the two 4-parameter ADCs of the ADC-unit. Then the ADCs digitize 5 signals (wedge, strip, meander of the wedge&strip-anode, electron, and TOF-signal; 5 of the 8 ADCs are actually used). The ADC inputs (0 - 10 V) have a resolution of 13 bit (8 k). A list processor (HYTEC LP1342) is used as ADC controller and as a cache for the recorded data. When the memory is full measurements are interrupted and the data transferred to a computer (Mac G4) connected via an SCSI-interface. Typical count rates were about 2000 counts/s and the transfer time was some ms in 1 s intervals.

I.2.5.6. Data evaluation

The five measured signals are stored in the computer with commercial software (Kmax, Sparrow Corp.). Already during acquisition the X and Y-Position of the scattered ion is calculated from the three signals of the wedge&strip-anode. The remaining four signals are then stored in several 3 MB blocks in list mode. With the Sparrow software the stored data are also evaluated after taking the data. The following output files are created during the evaluation procedure:

- The scattering distribution of the projectile ions on the MCP
- The mean number of emitted electrons per ion in dependence of the position of the ion on the MCP
- The mean value of the time-of-flight of ion in dependence of the position of the ion on the MCP
- The electron emission statistics (ES) spectrum in coincidence with scattered ions
- The TOF spectrum of the scattered ions
- Electron emission vs. projectile-TOF

With the program it was also possible to define different regions of interest on the MCP and evaluate these regions separately.

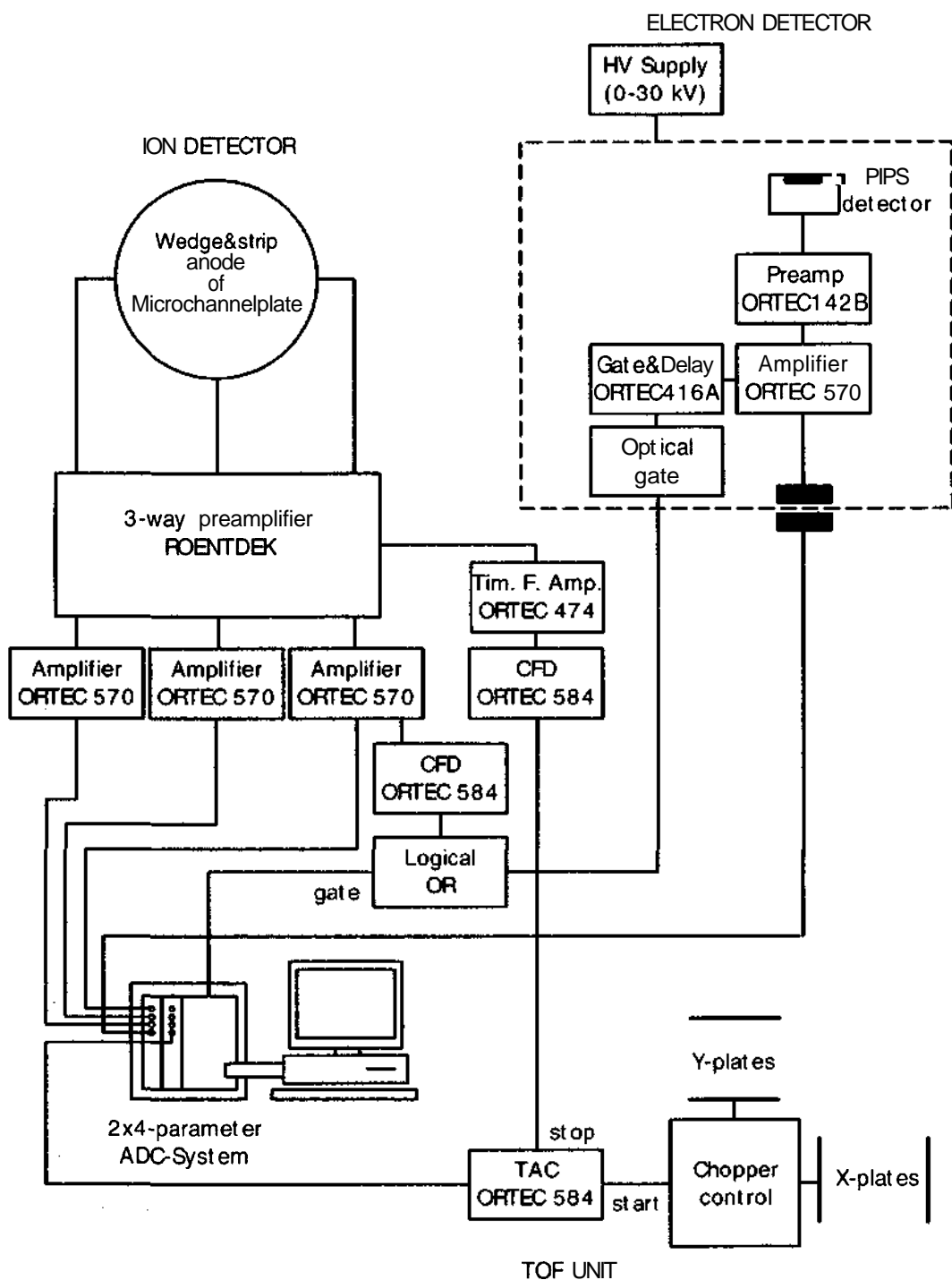


Fig. 1.16: Electronics (schematically) of the coincidence experiment NESSIE

I.2.6. Coincidence Measurements

In fig. 1.17 the intensity distribution of scattered projectiles, as recorded on the position sensitive MCP-detector, is shown for 18 keV Ar^{3+} ions impinging under a grazing angle of $\psi = 3.8^\circ$ onto the $\text{LiF}(001)$ single crystal surface (random azimuthal orientation). On the top of Fig. 1.17 the small fraction of the primary ion beam can be seen which has passed slightly above the target, while the broad feature on the bottom represents the angular distribution of scattered projectiles. The width of the scattering distribution ($\pm 3^\circ$ FWHM), points to imperfections in the $\text{LiF}(001)$ surface [36]. Projectiles scattered from the collective planar potential ("surface channeling" [19]) of an ideally flat surface are specularly reflected and would contribute only to the central peak of the angular distribution, while projectiles scattered from surface imperfections (e.g., steps) or those undergoing subsurface channeling show up in the wings of the scattering distribution.

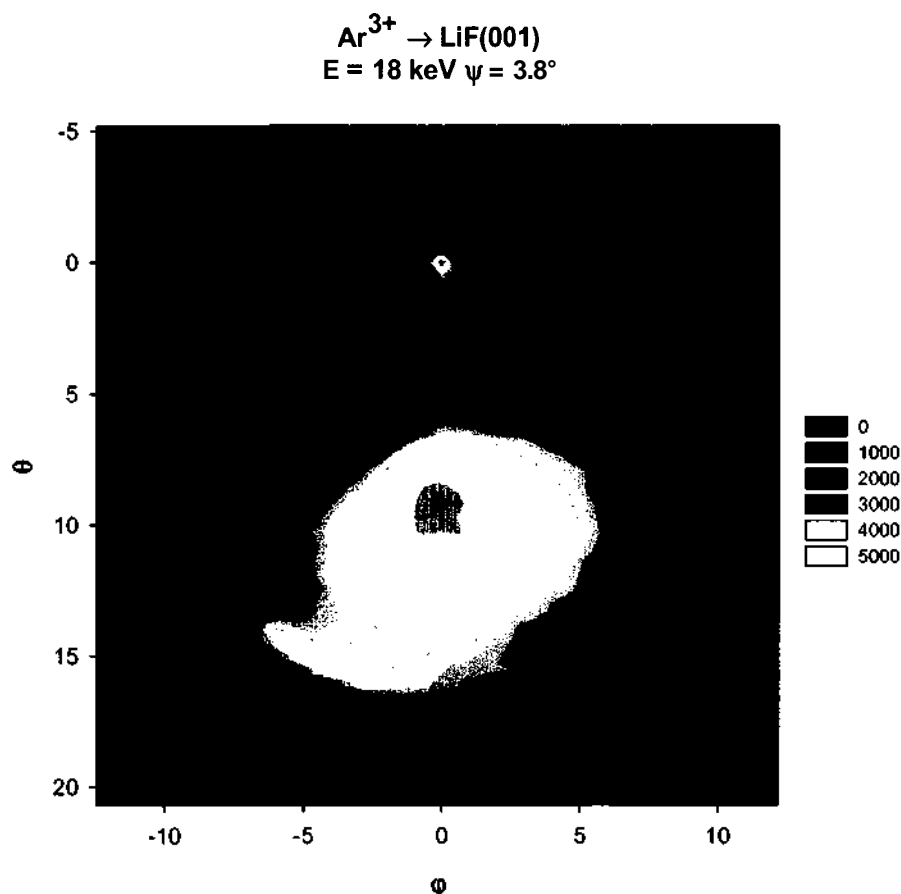


Fig. 1.17: Scattering distribution of 18 keV Ar^{3+} ions impinging on clean $\text{LiF}(001)$.

For a proper analysis of the measured data deflection of the direct beam and the scattered beam due to the weak electric field of the electron detector as well as image charge acceleration in front of the target had to be taken into account.

For a measured scattering angle θ the nominal angle of incidence ψ is given through:

$$\psi = \frac{\theta - \alpha}{2} \quad (1.19)$$

where α is the deflection of the direct peak with a velocity v_0 :

$$\alpha = \frac{v_{\perp}}{v_0} = \arctan \left(\frac{q U_e L}{m d v_0^2} \right) = \arctan \left(\frac{U_e}{U_q} \frac{L}{2d} \right). \quad (1.20)$$

U_e is the grid voltage of the electron detector; U_q the extraction voltage of the ion source, L marks the length of the electric field; d the distance from the grid to the target. E.g. for the example shown in fig. 1.17 U_e - 200 V, U_q - 9 kV, $L = 5$ cm, $d = 2$ cm. Then α amounts to $\alpha \approx 1.59^\circ$. The maximum of the scattering distribution is measured at $\theta = 9.15^\circ$ which leads to a nominal impact angle according to equ. (1.19) of $\psi = 3.8^\circ \pm 0.2^\circ$ (see fig. 1.18).

In fig. 1.19 measured angles of incidence for a fixed manipulator setting (red data for $\psi = 3.8^\circ$) show an increase with increasing projectile charge state due to image charge effects. If one corrects the latter by adjusting the target manipulator angles for each q by the right amount, one is able to record data at the same actual impact angle (see fig. 1.19).

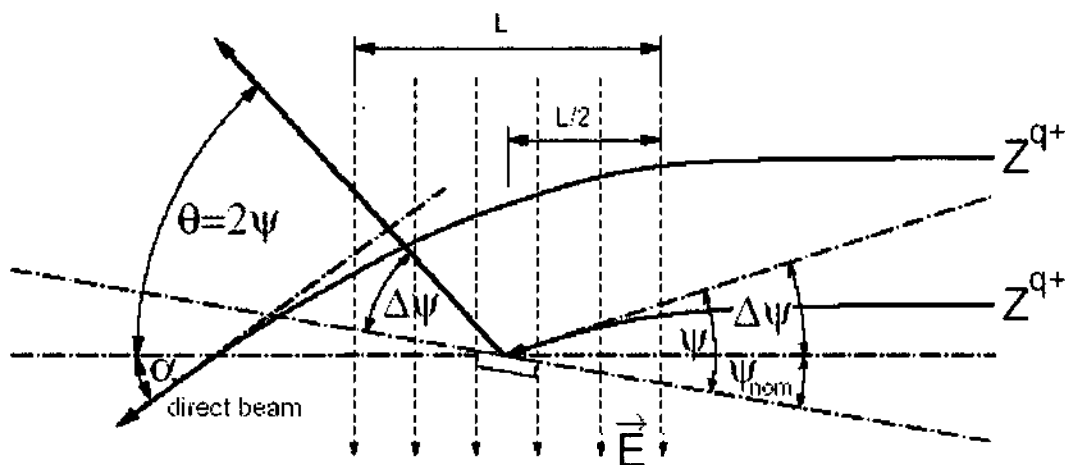


Fig. 1.18: Influence of the weak electric field on the scattering angle ψ .

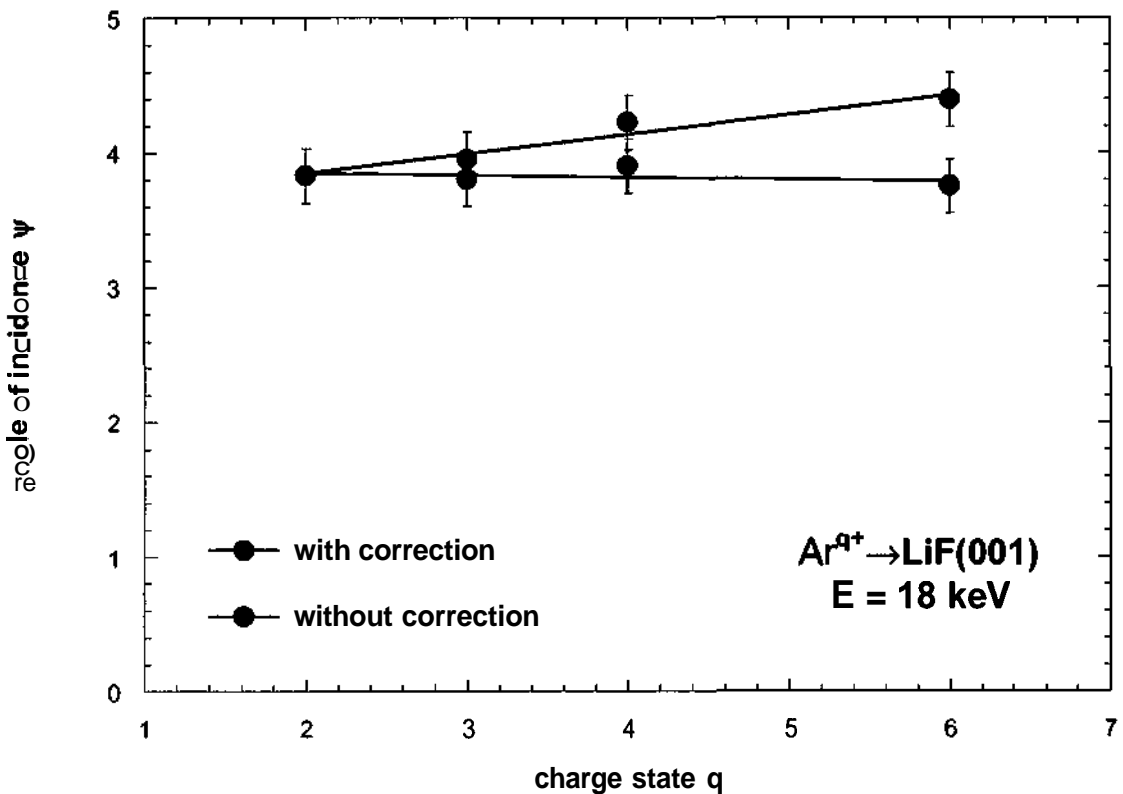


Fig. 1.19: "Actual" angle of incidence as measured for fixed manipulator setting (without correction) and after taking into account the effect of image charge acceleration (with correction) for 18 keV Ar^{q+} ions impinging on clean LiF(OOI) .

Fig. 1.20 shows the mean number of electrons per incident projectile (i.e., the total electron yield γ) for different projectile scattering angles (18 keV Ar^{3+} ions on LiF(OOI)). A pronounced minimum (in this case ~ 10 electrons/ion) appears between the position of the direct beam and the maximum of the scattering distribution (fig. 1.17). Particles emerging at larger scattering angles (wings of the distribution) cause emission of a considerably larger number of electrons (25 electrons/ion or even more). These measurements are in good agreement with previous measurements of Morozov *et al.* [37] who measured O^{q+} ($q < 7$) on LiF . Fig. 1.21 shows how this angle of minimum electron emission varies with the charge state q for 18 keV Ar^{q+} ions impinging on clean LiF(OOI) under 3.8° . Within our error bars this angle is independent of the charge state. No significant change of this angle is observed when the impact angles are corrected for

image charge effects as described above. Surprisingly the angle of minimum electron emission $e = 0.8^\circ$ ($0 \sim 5^\circ$) is close to the angle which corresponds to projectiles scattered in parallel to the target surface plane.

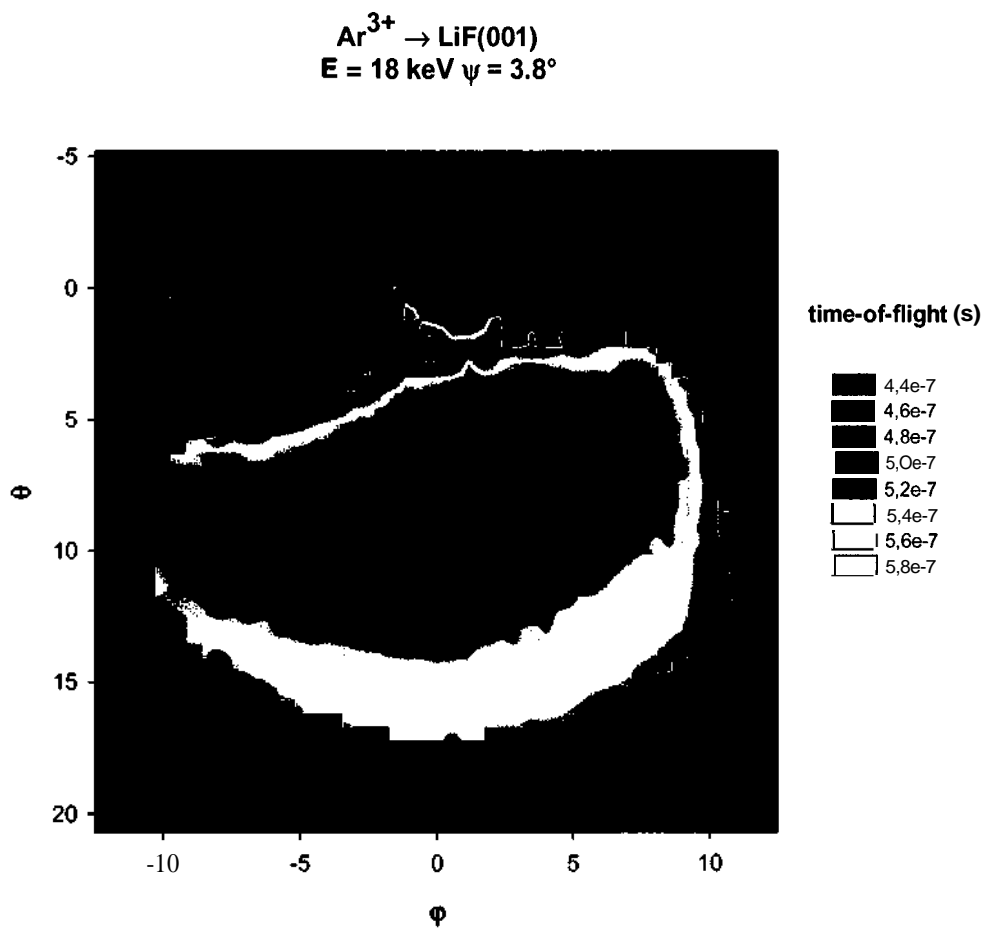


Fig. 1.20: Mean number of emitted electrons per incident ion plotted as a function of the position of the scattered projectiles as recorded on the MCP for 18 keV Ar^{3+} ions impinging on clean $\text{LiF}(001)$.

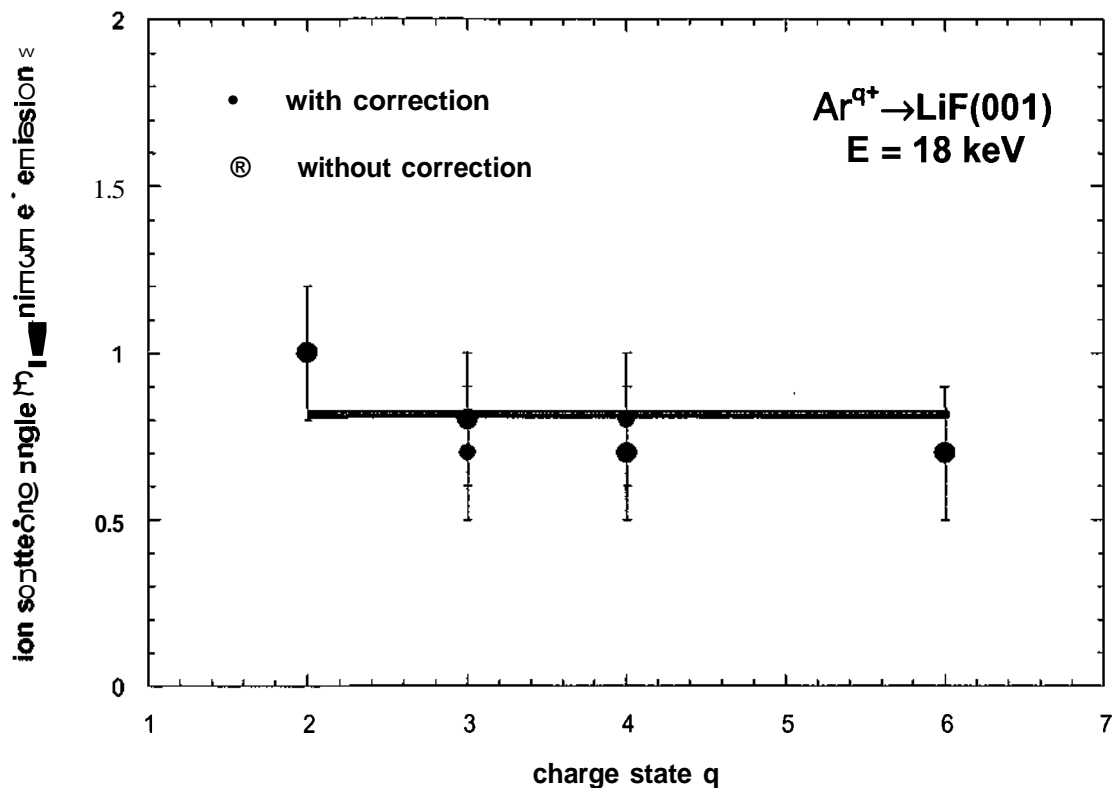


Fig. 1.21: Measured scattering angle ε for minimum electron emission y at fixed manipulator setting (without correction) as well as after correction of image charge effects (with correction) for 18 keV Ar^{q+} ions impinging on clean LiF(OOl). The angle $\varepsilon = 0^\circ$ indicates the value for projectiles which have been scattered parallel to the target surface.

In fig. 1.22 the time-of-flight which the projectiles need to reach the detector is shown as a function of the scattering angle. Already from a first glance it is seen that next-to-specularly reflected projectiles also have the shortest time-of-flight. Data are shown after correction for geometrical effects (c.f. equ. (1.12) in chap. I.2.4).

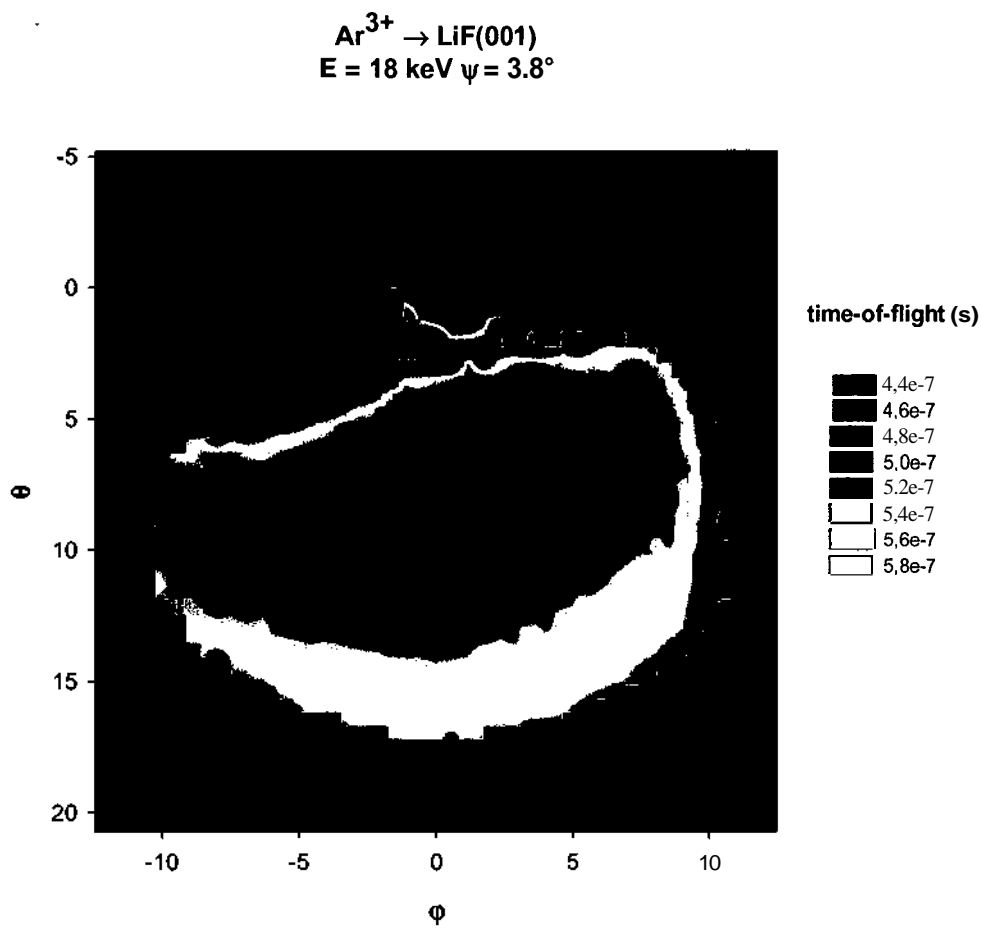


Fig. 1.22: Mean time-of-flight of projectile ions plotted as a function of the position of the scattered projectiles as recorded on the MCP for 18 keV Ar^{3+} ions impinging on clean LiF(OOL) .

Using the coincidence technique it was also possible to investigate a correlation between the number of emitted electrons and the projectile energy loss. In Fig. 1.23 a typical coincidence spectra is shown for 18 keV Ar^{3+} ions impinging on clean LiF(OOL) . It can be clearly seen that the number of emitted electrons increases with larger projectile energy losses.

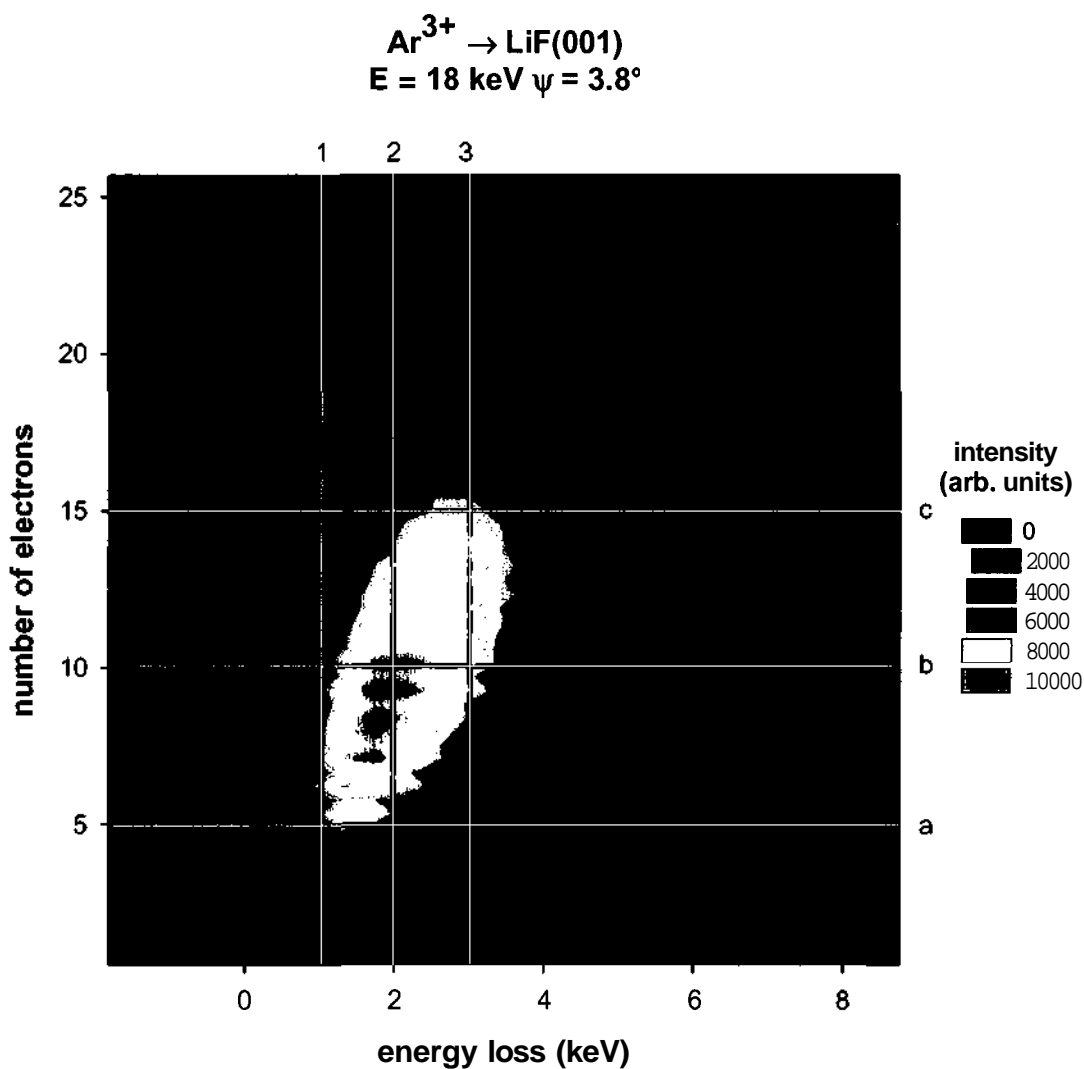


Fig. 1.23: Coincidence spectrum for number of electrons vs. projectile energy loss for 18 keV Ar^{3+} ions impinging on clean $\text{LiF}(001)$. The white lines (1..3, a..c) refer to cuts in the spectrum as shown in figs. 1.24 and 1.25.

White lines in Fig. 1.23 indicate possible cuts through such a coincidence spectrum for further analysis. A spectrum can be cut along constant values of projectile energy loss (cuts 1..3 in fig. 1.23) as well as constant numbers of emitted electrons (cuts a..b in fig. 1.23). Fig. 1.24 shows a comparison of cuts along constant projectile energy loss for $E_{loss} = 1, 2$, and 3 keV of Ar^{3+} projectiles impinging on LiF . The such derived electron spectra can be analyzed in the usual way. It can be seen very clearly that the number of emitted electrons increases with increasing projectile energy loss. The curves

show also features which correspond to individual numbers of electrons as detected by the SBD.

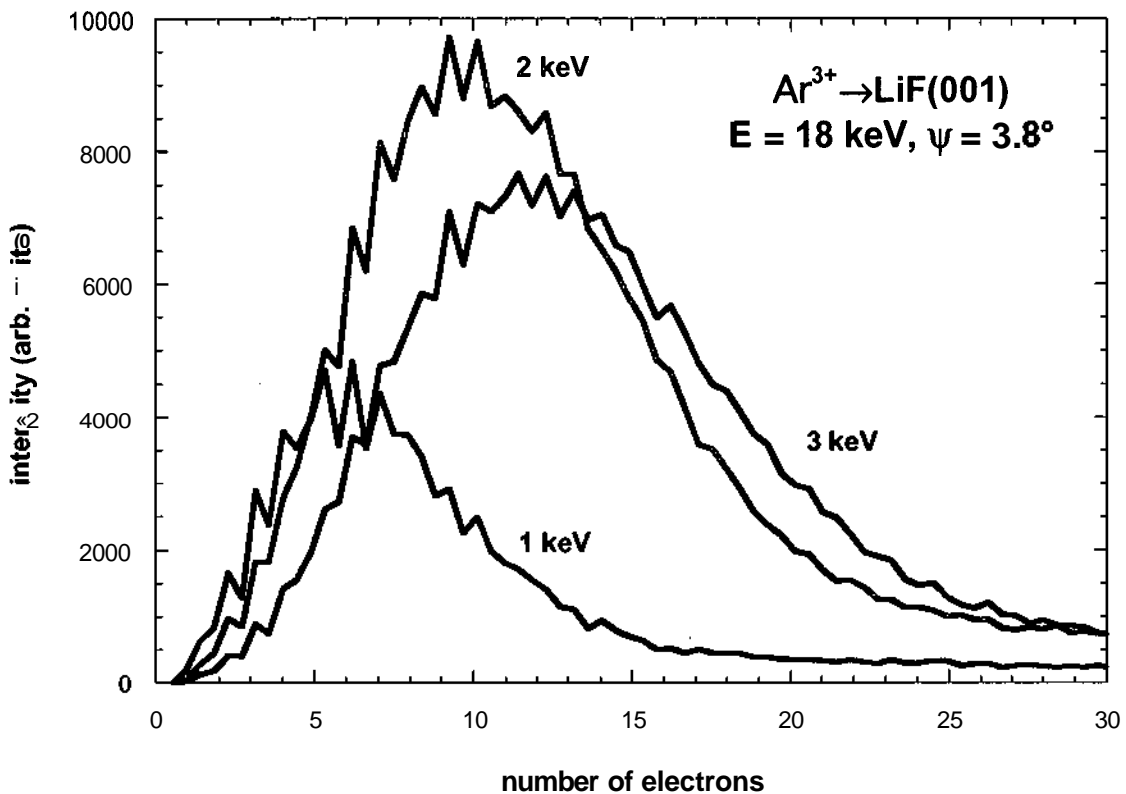


Fig. 1.24: Cuts of coincidence spectrum for 18 keV Ar^{3+} ions impinging on clean LiF(OOI) for $E_{loss} = 1, 2$ and 3 keV (cuts numbered 1, 2, 3 in fig. 1.23).

In fig. 1.25 cuts along constant numbers of emitted electrons are shown for 18 keV Ar^{3+} ions impinging on clean LiF(OOI) according to fig. 1.23. Also in this plot it can be seen that the projectile energy loss increases for cuts corresponding to higher numbers of emitted electrons.

It has to be pointed out that cuts along constant projectile energy loss and constant numbers of emitted electrons give different results when walking on the ridge of the coincidence distribution. Fig. 1.26 shows a comparison between the two different ways of data evaluation. It can be seen that cuts along constant numbers of emitted electrons deliver a threshold of the projectile energy loss for 0 electrons emitted during the scattering process while cuts for constant energy loss yield a minimum number of emitted electrons for zero energy loss.

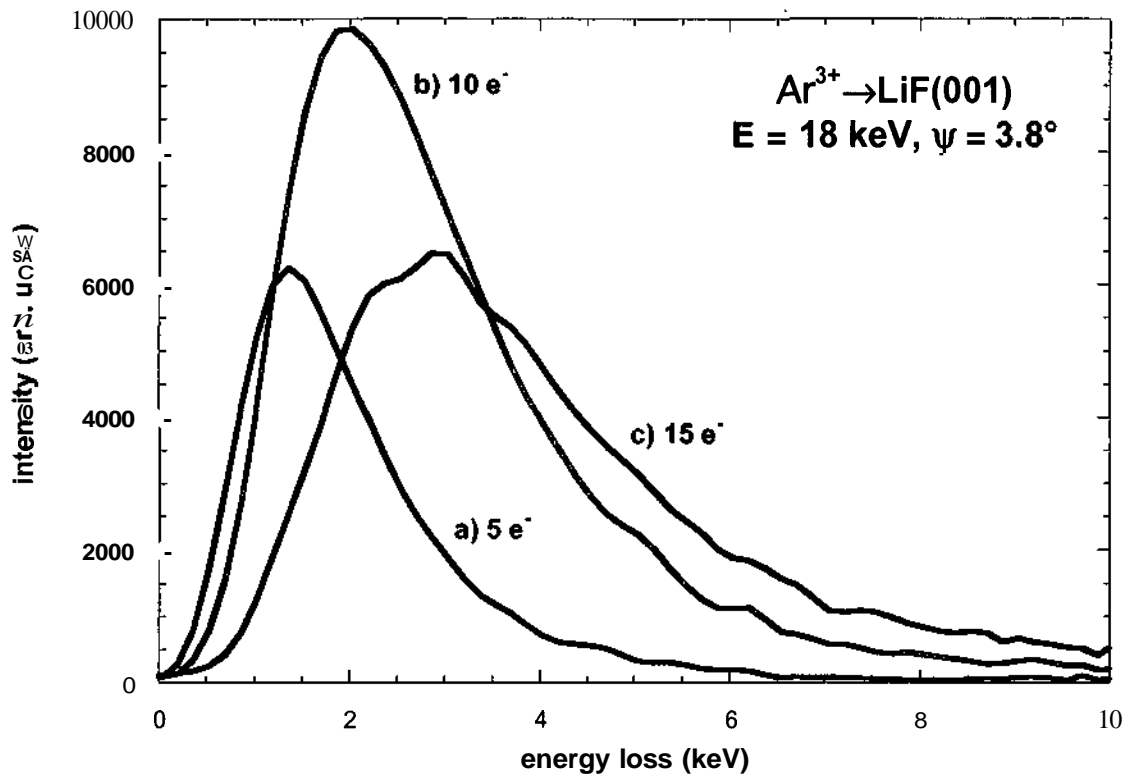


Fig. 1.25: Cuts of coincidence spectrum for 18 keV Ar³⁺ ions impinging on clean LiF(OOI) for 5, 10, and 15 emitted electrons (cuts a, b, c from fig. 1.23).

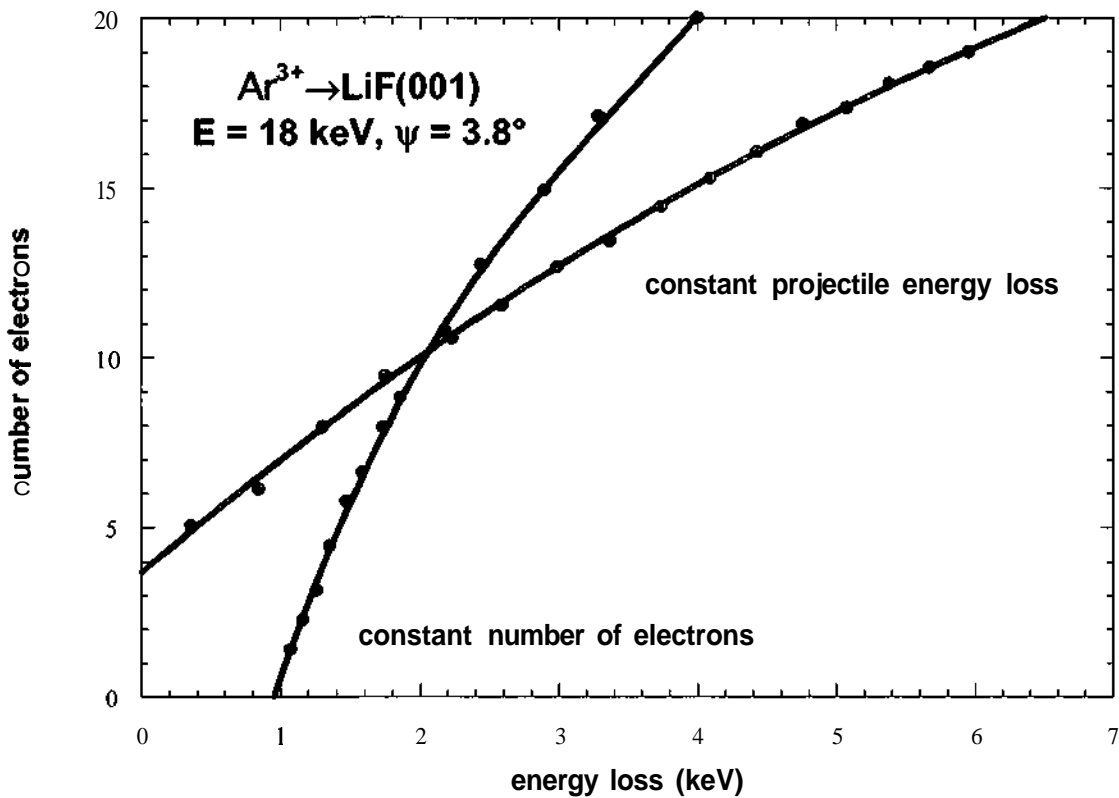


Fig. 1.26: The red curve gives mean electron yields evaluated from the coincidence spectrum shown in fig. 1.23 for cuts along constant projectile energy loss, the green data show the mean energy loss evaluated for fixed numbers of emitted electrons. All data for 18 keV Ar³⁺ ions impinging on clean LiF(OOI).

I.3. Results and discussion

The coincidence technique allows to clearly distinguish between three different types of projectile trajectories [16] namely (see Fig. 1.27):

- Type 1: Projectiles reflected specularly at the target surface
- Type 2: Projectiles which have entered the target (e.g. at surface imperfections) and have left it after having undergone multiple scattering below the topmost atomic layer, causing exit angles slightly different from the angle of incidence ψ .
- Type 3: Projectiles penetrating the target (or being scattered at a very different angle).

Accordingly we defined two regions on the MCP to look for differences in the number of emitted electrons for type 1 and type 2 trajectories projectile trajectories (see fig. 1.28).

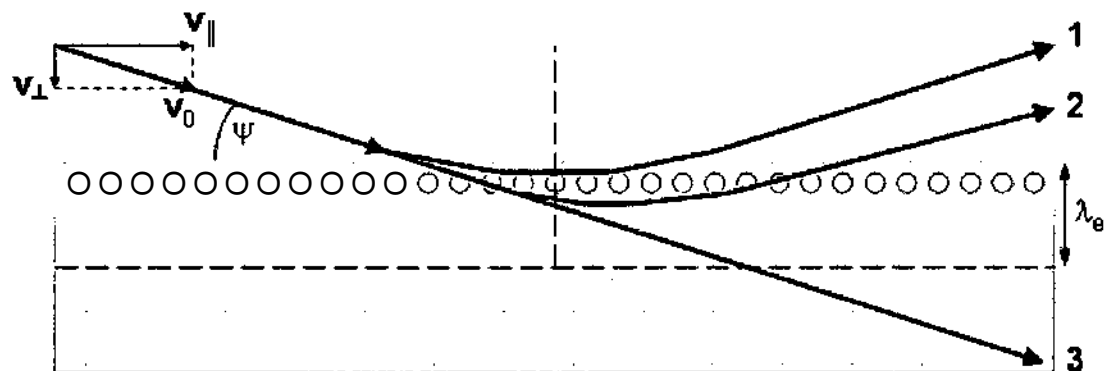


Fig. 1.27: Scheme of different types of trajectories of a projectile under grazing incidence on a single crystal target.

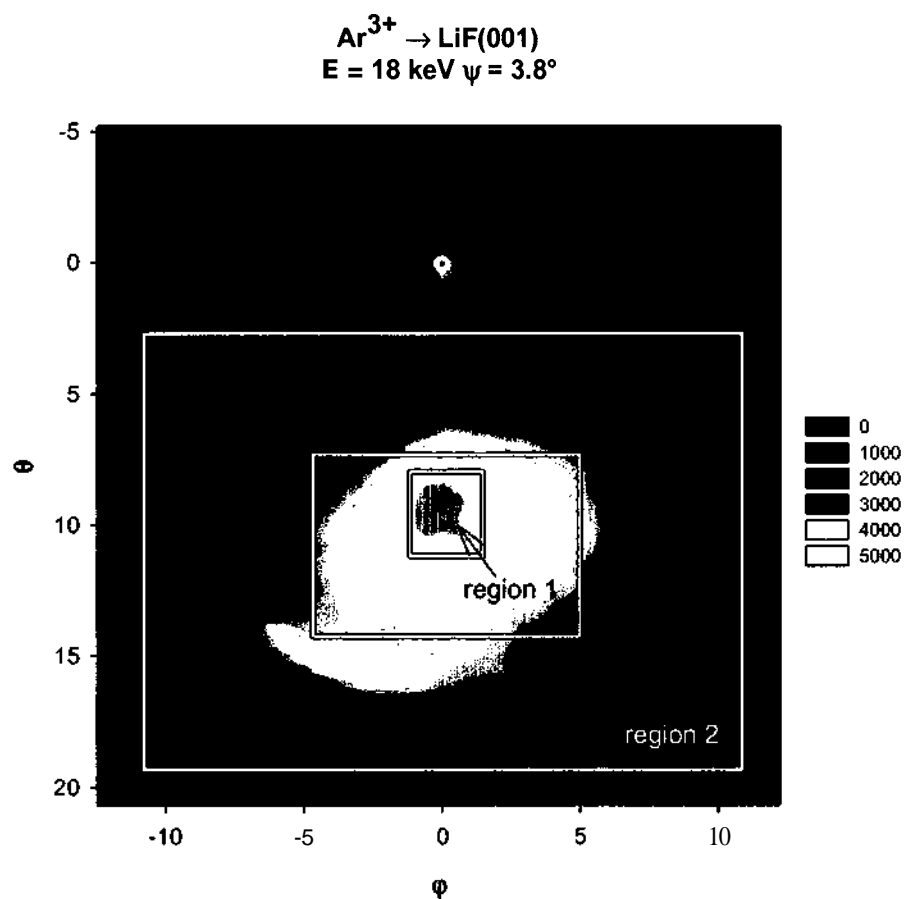


Fig. 1.28: Scheme of selected regions of the scattering distribution for the analysis of the different types of trajectories for Ar^{3+} at $E = 18 \text{ keV}$ on LiF(OOI) .

Fig. 1.29 shows the maxima of the projectile energy loss distributions for 18 keV Ar ions impact on LiF(OOI) with different charge states ($q = 2, 3, 4, 6$). It can be seen that the kinetic energy loss for both types of trajectories is rather independent of the projectile charge state which gives a first hint that the above and below surface interaction can be separated. Trajectories of type 1 (above-surface scattering) show also a smaller energy loss than type 2-scattered ions ($\Delta E_{loss} \sim 700 \text{ eV}$). A similar result is also found in fig. 1.30 where the mean energy loss of the projectiles is plotted for 18 keV Ar^{q+} ($q = 2, 3, 4, 6$) on LiF(OOI) . Here the difference in energy loss for the two types of trajectories is about $\Delta E_{mean} \sim 1200 \text{ eV}$.

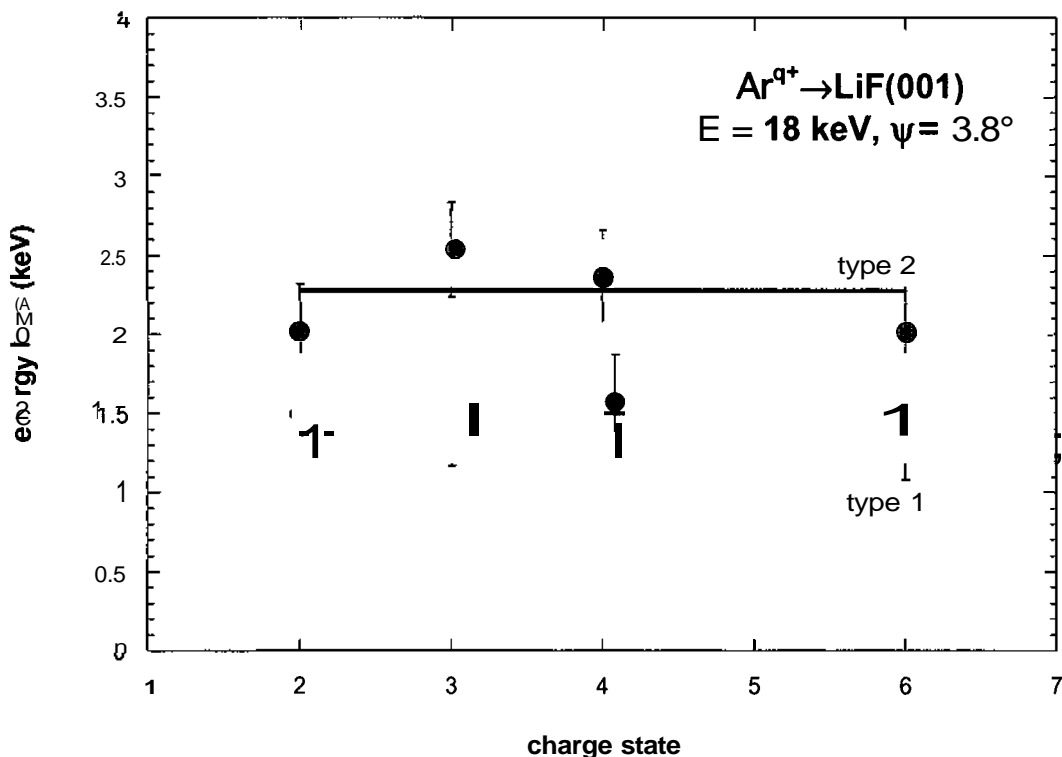


Fig. 1.29: Maximum of the projectile energy loss distribution for type 1 and type 2 trajectories (see above) for 18 keV Ar^{q+} ($q = 2, 3, 4, 6$) on $\text{LiF}(001)$.

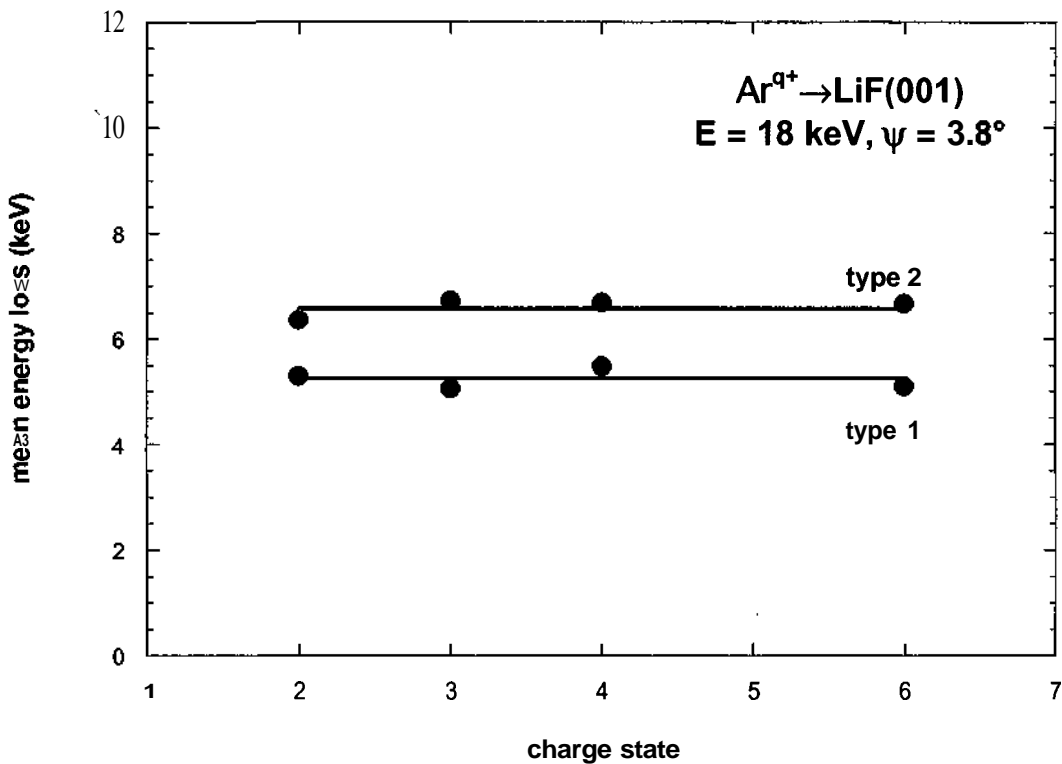


Fig. 1.30: Mean projectile energy loss for trajectory types 1 and 2 (see above) for 18 keV Ar^{q+} ($q = 2, 3, 4, 6$) on $\text{LiF}(001)$.

The electron yield γ as plotted in fig. 1.31 shows a weak but significant dependence on the projectile charge state. The yield increases with higher charge state and therefore increased potential energy of the impinging ion. It can be seen that the yield difference between the two types of trajectories remains about constant over the hole range of investigated projectile charge states and therefore supports the idea that the below surface part of the interaction is independent of the initial charge state of the projectile.

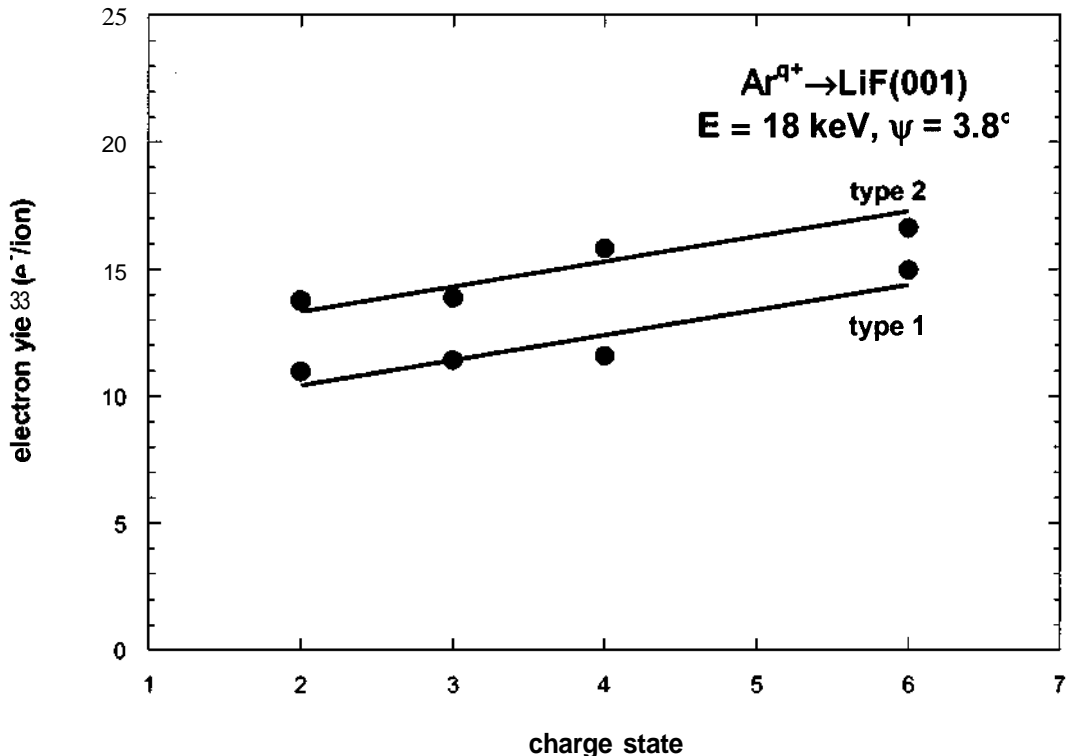


Fig. 1.31: Total electron yield γ for trajectories of type 1 and 2 (see above) for 18 keV Ar^{q+} ($q = 2, 3, 4, 6$) on LiF(OOI) .

For a further evaluation coincidence plots as shown in fig. 1.23 have been analyzed for different projectile charge and impact energies. In fig. 1.32a electron yields for cuts along constant projectile energy loss are shown for Ar^{q+} ($q = 2, 3, 4, 6$) ions at $E = 18$ keV while in fig. 1.32b these cuts are given for different impact energies ($E = 24, 30, 42$ keV Ar^{6+} , and 54 keV Ar^{8+}). All curves show similar dependences of the electron yield on the energy loss. If the data are extrapolated to zero energy loss, a finite number

of emitted electrons is derived, which we believe can be associated with "pure" potential electron emission $\gamma(\Delta E = 0) = \gamma_{PE}$. As can be seen from fig. 1.23 events with zero-energy loss almost never happen, but our extrapolation clearly allows us to derive that part of the yield which causes no energy loss of the projectile. Plotting the extrapolated γ_{PE} values as a function of the potential energy of the projectile ion one finds a linear dependence (fig. 1.33). In a simple model an energy of $2W_\phi$ is necessary to emit an electron via potential emission. Taking into account the available energy given by the potential energy (E_{pot}) of the projectile one can estimate the maximum number of emitted electrons due to potential emission with the formula:

$$\gamma_{PE}^{\max} = \frac{E_{pot}}{2W_\phi}. \quad (1.21)$$

Equ. (1.21) is shown as a green line in fig. 1.33 and agrees surprisingly well with our measured data. We conclude that this part of the electron yield is produced in front of or at the surface and emitted towards our electron detection unit (see also Part II). Although we have a weak electric field which accelerates the electrons towards the grid about half of all electrons should be emitted into the solid surface. But since the band gap of the LiF target extends a few eV above the vacuum level these electrons cannot penetrate and are therefore "reflected" by the band gap.

As a next step we now consider the mean energy loss for cuts along constant numbers of emitted electrons. In fig. 1.34a we first show the charge state dependence Ar^{q+} ($q = 2, 3, 4, 6$) at a fixed impact energy of $E = 18$ keV while in b we plot curves for different impact energies $E = 24, 30, 42, 54$ keV but fixed projectile charge state (Ar^{6+}). First of all we note (fig. 1.34a) that the charge state q has little influence on the mean energy loss. Especially interesting results are obtained if one extrapolates the curves to zero electron emission. Although again very rare events they provide information on the mean energy loss associated with the emission of no electron (pure stopping case). In fig. 1.34b a strong correlation between projectile energy loss and initial kinetic energy can be observed. Plotting energy loss values (extrapolated for zero electron emission) vs. the kinetic energy reveals as a first approximation a linear dependence. The slope of this line is given by $E_{loss}/E_{kin} \sim 0.06$ [38].

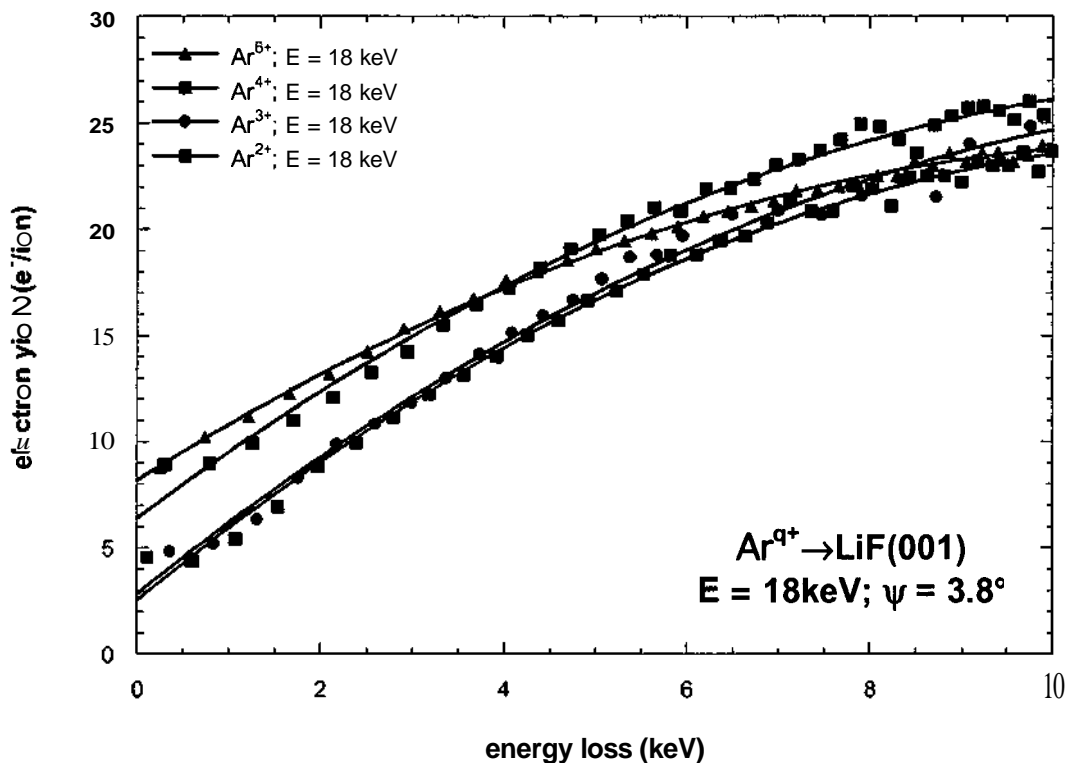


Fig. 1.32a: Electron yield for cuts along different values of projectile energy loss for Ar^{q+} ($q = 2, 3, 4, 6$) $E = 18$ keV on LiF(OOL) .

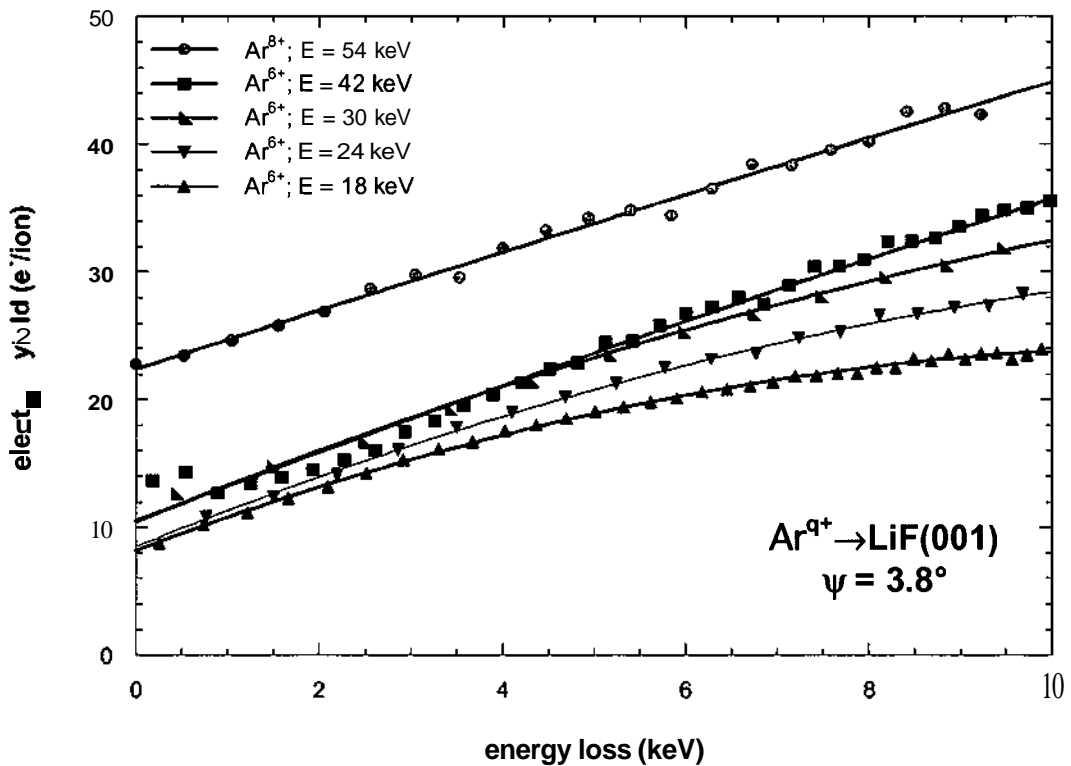


Fig. 1.32b: Electron yield for cuts along different values of projectile energy loss for Ar^{6+} at $E = 24, 30, 42$ keV and Ar^{8+} at $E = 54$ keV on LiF(OOL) .

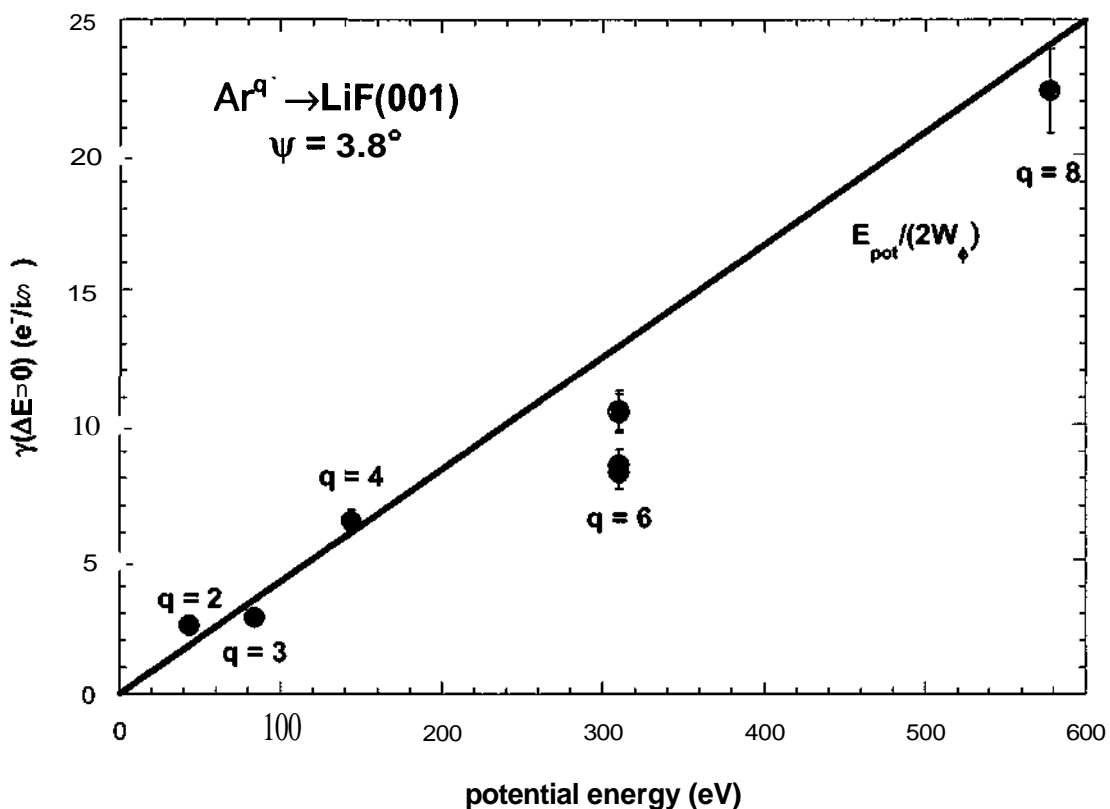


Fig. 1.33: Electron emission associated with zero energy loss of the projectile plotted as a function of the charge state for Ar^{q+} ($q = 2, 3, 4, 6$) $E = 18$ keV as well as for Ar^{6+} at $E = 24, 30, 42$ keV, and Ar^{8+} at $E = 54$ keV on LiF(OOI) . Green line calculated according to equ. (1.21).

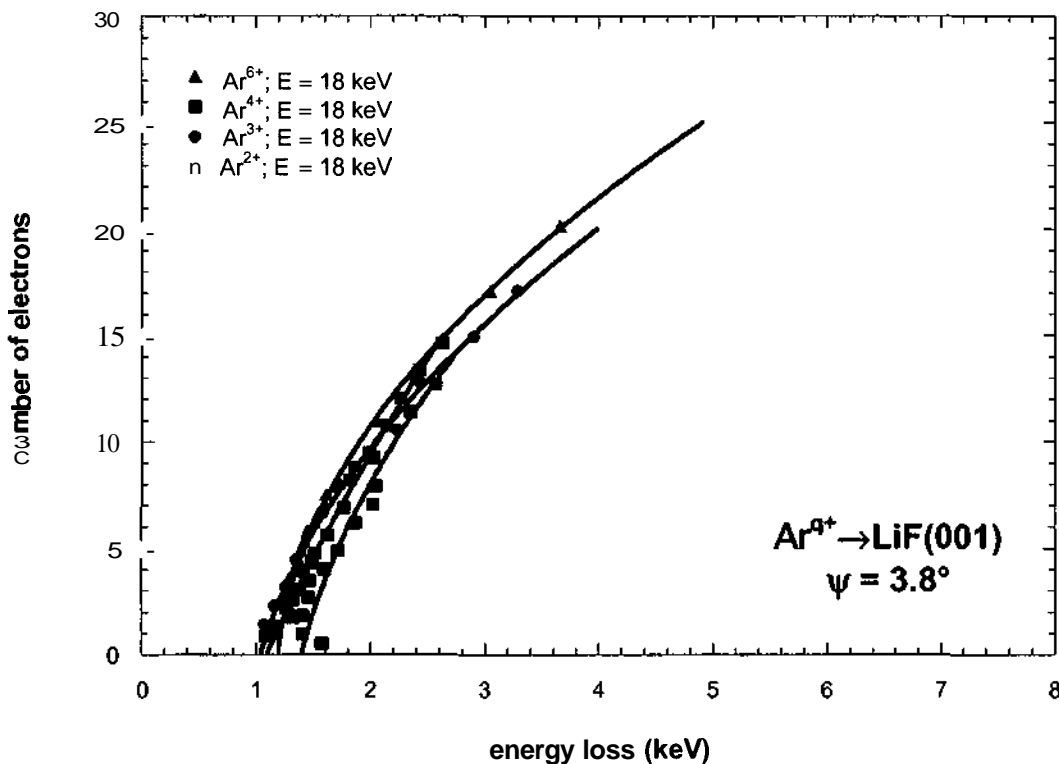


Fig. 1.34a: Electron yield for cuts along different numbers of emitted electrons for Ar^{q+} ($q = 2, 3, 4, 6$) at $E = 18$ keV on $\text{LiF}(001)$.

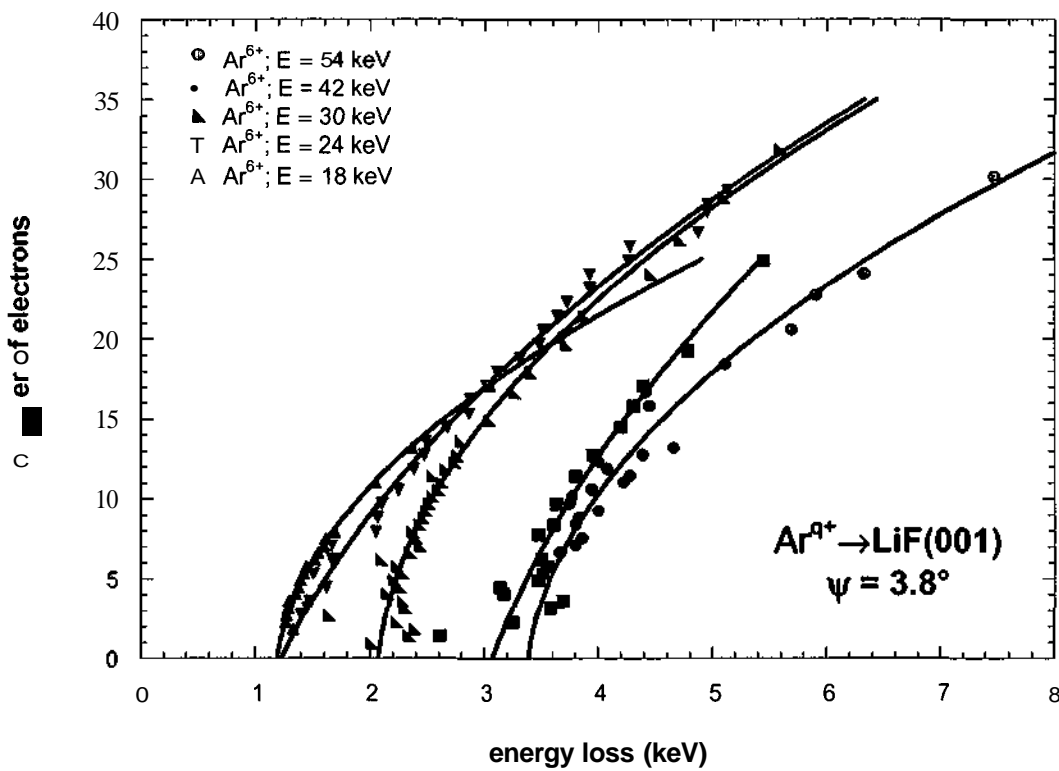


Fig. 1.34b: Electron yield for cuts along different numbers of emitted electrons for Ar^{6+} at $E = 18, 24, 30, 42, 54$ keV on $\text{LiF}(001)$.

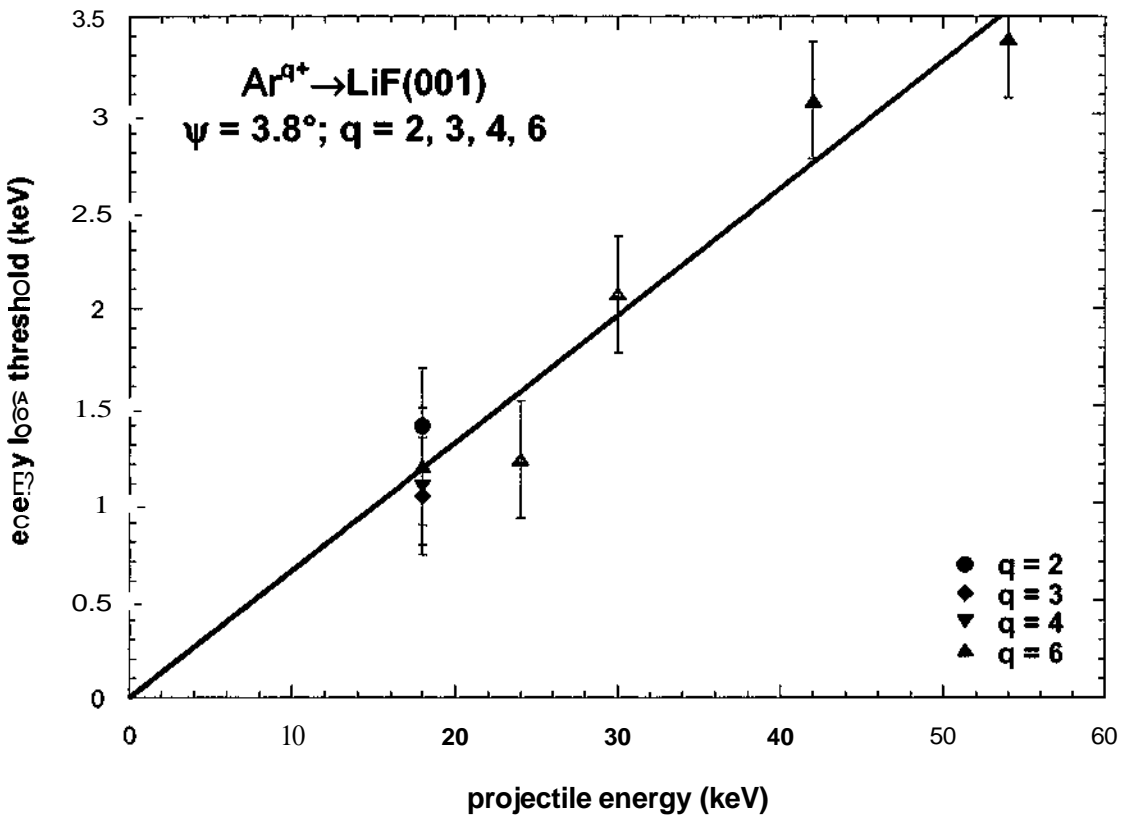


Fig. 1.35: Projectile energy loss for zero emission of electrons vs. kinetic energy of the projectile for Ar^{q+} ($q = 2, 3, 4, 6$) at $E = 18$ keV as well as Ar^{6+} at $E = 24, 30, 42, 54$ keV on LiF(OOL) . The green line is a linear fit to the measured data.

From the data presented in this chapter we propose the following scenario. The multiply charged ion approaches the surface and according to its potential energy a certain number of electrons is emitted via potential electron emission. This "pure" potential emission contribution can be derived from our coincidence data in a unique way (despite the fact that an almost equally large kinetic contribution is present) by extrapolating the cuts for constant projectile energy loss to zero.

Further electron emission takes place when the projectile finally hits the surface and is either reflected or penetrates the target. Since this contribution is nearly independent of the primary ion charge state we assume that the "hollow atom" formed during the approach has been destroyed during or shortly before the impact and the

projectile has lost its memory (on the original charge state). Electrons are no longer emitted at the expense of the projectile's potential energy but now cost kinetic energy. This kinetic energy loss increases linearly with the projectile energy but is (almost) independent of the primary projectile charge state.

The small remaining charge state dependence is consistent with data obtained for multiply charged ions on LiF surfaces under normal incidence conditions, where electron promotion in quasi-molecular collisions between the projectile and F" lattice atoms has been assumed to be responsible for the slight decrease in kinetic electron emission yield with increasing charge state [12, 13].

The total projectile energy loss ΔE results from the integration of a position dependent stopping power $dE/dx(z)$ over complete trajectories:

$$\Delta E = \int_{\text{traj}} \frac{dE}{dx}(z) dx \quad (1.22)$$

Recently, Auth and Winter [39] have shown that obtains for a planar potential approximated by long range screening $U(z) = 2\pi n_s Z_1 Z_2 a_s a_3 \exp(-b_3 z/a_s)/b$ (n_s = density of surface atoms, Z_1 and Z_2 nuclear charges of projectile and target atoms, respectively, a_s - screening length, $a_3 = 0.35$ and $b_3 = 0.3$ for Moliere screening, atomic units used)

$$\frac{dE}{dx}(z) = \frac{dE}{dx}(0) \exp\left(-\frac{b_3}{2a_s} z\right) \quad (1.23)$$

with

$$\frac{dE}{dx}(0) = \Delta E \cdot \left(\frac{n_s Z_1 Z_2 a_s b_3}{2\pi a_s E} \right)^{1/2} \quad (1.24)$$

Since in our experiment we observe $\Delta E \sim E$ (see fig. 1.35), we obtain from equ. (1.24) that $dE/dx(0) \sim \sqrt{E} \sim v$ which is the usual velocity dependence behavior for electronic stopping in this velocity regime already found for LiF transmission experiments with light ions [40].

Part II:

- Electron emission and energy loss in grazing collisions of neutral projectiles with insulator surfaces

II.1. Introduction

Electron emission phenomena induced by ion impact on insulator targets show interesting features as relatively high electron yields and low thresholds for kinetic emission [1, 12, 41, 42]. At first glance, these results come somewhat surprising, since, for e.g. ionic crystals the binding energies of valence band electrons amount to typically 10 eV, i.e., clearly larger than work functions of metals surfaces. Recent studies on this problem revealed interatomic electron promotion as the dominant mechanism for electron emission from insulators at low impact energies [13, 42].

Electron promotion has also been considered for the interpretation of a "metal-like" behavior concerning stopping of atomic projectiles in the bulk or in front of an insulator target [40], where a threshold for a wide band gap insulator (LiF) is observed for protons at energies as low as about 1 keV [43]. First coincident measurements of projectile energy loss and electron emission by Roncin *et al.* [44] by means of a multi-detector array and analysis of list-mode data revealed the dominant mechanisms for the dissipation of kinetic energy of hydrogen projectiles in front of a LiF(OOI) surface. In particular, evidence for an energy loss via the excitation of surface excitons was obtained by relating time-of-flight (TOF) spectra to events with emission of no electron. From inelastic events accompanied with no electron emission Roncin *et al.* [44] identified the formation of surface excitons as dominant excitation channel for valence band electrons.

An alternative mechanism for electron emission during grazing impact of hydrogen ions on LiF was proposed by Stracke *et al.* [45] and Zeijlmans van Emmichoven *et al.* [42] from measured electron spectra for projectile energies of some 100 eV. Here, electron promotion in close $H^+ + F^-$ binary collisions followed by autoionization of doubly excited F^- states is considered to explain emission of electrons at low collision energies (details see below).

In this section of the thesis studies with hydrogen atoms as well as helium atoms scattered under a grazing angle of incidence from an atomically flat and clean LiF(OOI) surface are presented. For these conditions, characterized by well-defined projectile trajectories ("surface channeling" [46, 47]), the number of emitted electrons per incident projectile (the electron number statistics), and - by means of a TOF setup - the

projectile energy loss have been studied. By relating events in the detection branch for scattered projectiles to the signal of the electron detector, one obtains information on the electron excitation and emission processes during bombardment of the surface with H° and He^0 atoms. Our data support recent findings of a close relation between electron emission and projectile energy dissipation [44]. From measurements of electron yields and projectile energy losses for a consequent variation of the grazing angle of incidence ψ and the projectile energy E , we derive position dependent electron production rates $P(z)$ and stopping power $S(z)$. Information on the interaction processes are deduced from TOF measurements in coincidence with specific electron numbers.

The measurements have been performed at the Institut für Physik der Humboldt Universität zu Berlin during several research visits in 2000 - 2002. The electron emission statistics detector unit was built in Vienna and installed at the ion scattering experiment in Berlin.

Persons involved in the experiments were A. Mertens, K. Maass, S. Lederer, and H. Winter from the Berlin side and J. Stöckl, H. Eder, HP. Winter, and F. Aumayr from the TU Wien side.

II.2. Description of the experiment

II.2.1. Experimental setup

Fig. 2.1 shows a sketch of the experimental setup. A well collimated beam of H^+ (or He^+ atoms produced as ions in a hollow cathode ion source with kinetic energies of $250 \text{ eV} < E < 20 \text{ keV}$ (energy spread $\Delta E/E < 10^{-3}$) is chopped, neutralized, and directed under a grazing angle of incidence $0.4^\circ < \psi < 2^\circ$ on a flat and clean $\text{LiF}(\text{OOL})$ surface. The target is kept under UHV conditions at a base pressure of about $5 \times 10^{-11} \text{ mbar}$, and its surface is prepared by cycles of grazing sputtering with 25 keV Ar^+ ions and subsequent annealing at about 400°C . Neutral projectiles are used here in order to eliminate effects on projectile trajectories caused by the small electric field needed for initial collection of electrons into the electron number detector and by image charge attraction for ions [13]. Furthermore, contributions of potential electron emission can be excluded for neutral atoms. Chopped H^0 (He^0) beams for the TOF studies are achieved by deflection of protons in a pair of electric field plates ($U = \pm 5 \text{ V}$ per keV beam energy) and subsequent near-resonant neutralization in a differentially pumped gas-target ($p = 10^{-3} \text{ mbar}$) operated with Kr gas (in the case of He^+ resonant neutralization with He gas). Non-neutralized projectiles are deflected via electrostatic field plates behind the gas-target. Typical intensities of the projectile beam amount to some 10^3 atoms/sec so that modifications of the target surface by projectiles will be on a negligible level. Scattered projectiles are detected by a channelplate electron multiplier (CEM, Roentdek) mounted at a distance of 1.38 m behind the target. The CEM has a dihedral angle of 0.8° to limit the scattered beam and is moveable to measure at various scattering angles. This detector provides the "start" signal for the TOF setup, whereas the "stop" is derived from the precise digitally delayed signal of the beam chopper.

Electrons emitted from the surface are extracted by a weak electric field of some 10 V/cm applied to a highly transparent grid about 1 cm apart from the target. A sketch of the electron detection unit can be seen in fig. 2.2. This grid shields the voltage for accelerating the electrons toward a surface barrier detector (SBD) biased at +30 kV. The number of electrons emitted per projectile impact is obtained from the pulse height distribution of the SBD which shows discrete peaks that can unambiguously be assigned

to discrete numbers of emitted electrons. The efficiency for detection of electrons by the SBD is close to 100 % (ray trace calculations indicate that about 98 % of the electrons with energies < 50 eV are detected), so that no corrections for the electron number spectra are needed.

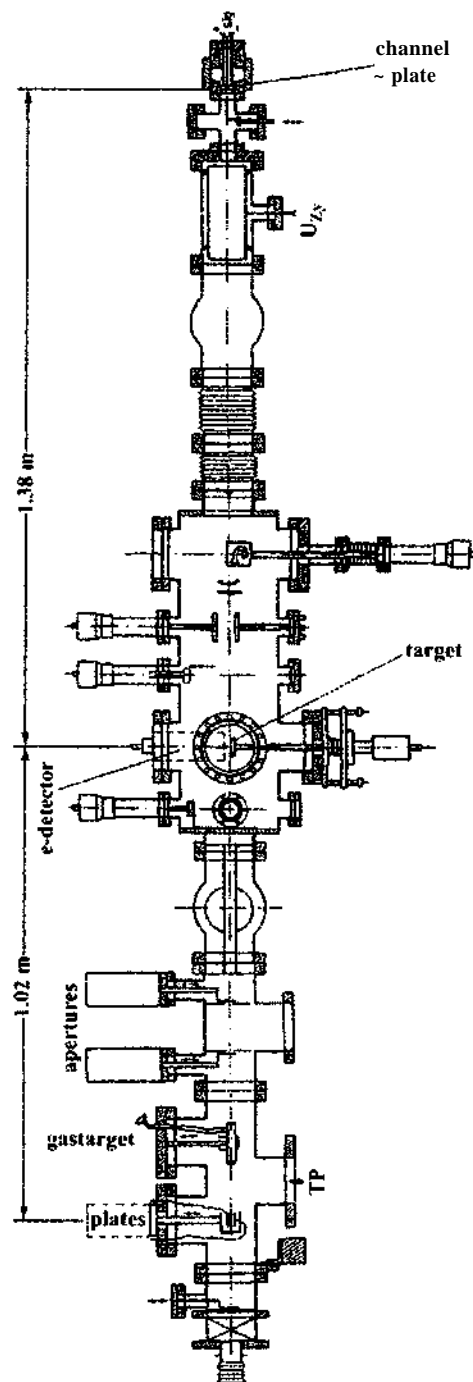


Fig. 2.1: Experimental setup [48].

In the experiment, the H° (He^0) projectiles are scattered from the surface for an azimuthal orientation of the crystal surface about 10° off the $\langle 110 \rangle$ -axis in the surface plane, i.e., a "random" azimuthal setting. At fixed projectile energies the (polar) angle of incidence ψ is varied and data with the electron number detector and CEM are recorded.

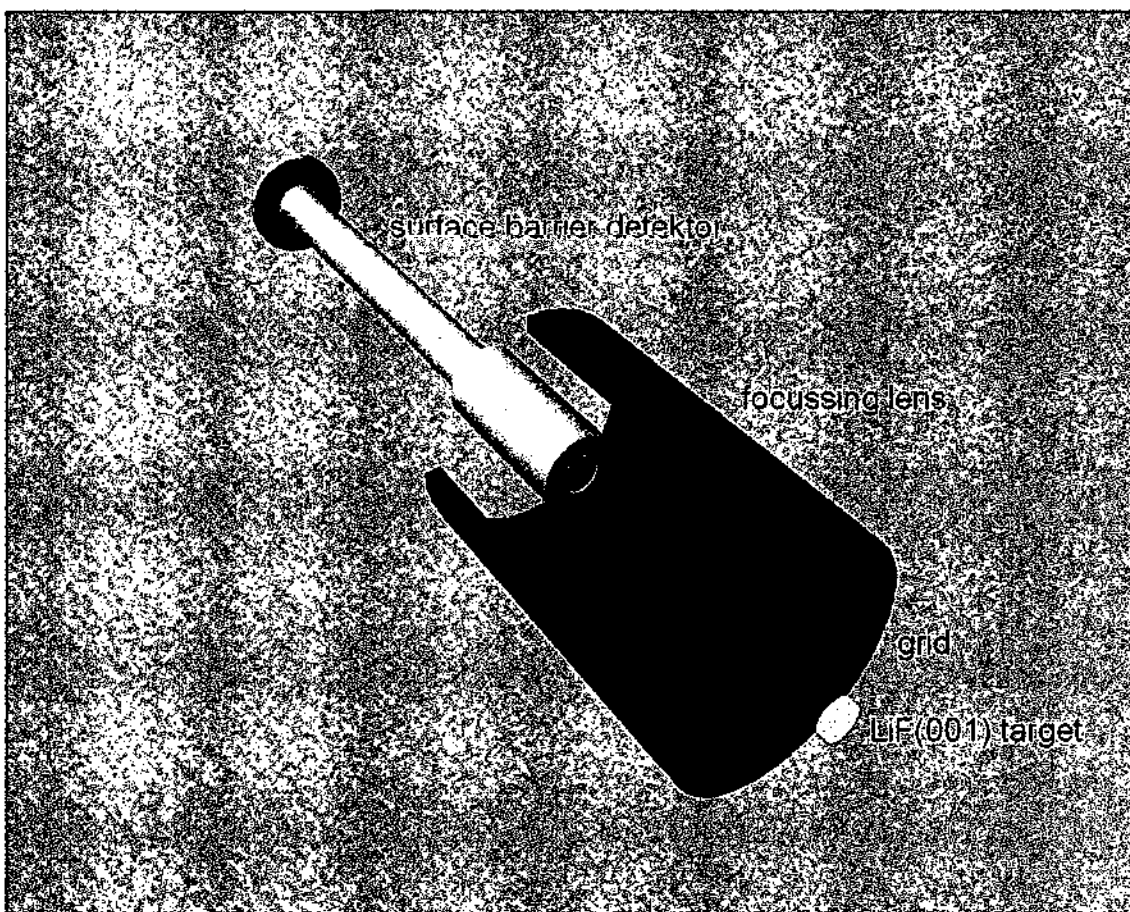


Fig. 2.2: Electron detection unit.

II.2.2. Data acquisition

In the TOF setup, the output signal from a time-to-amplitude converter (TAC) is fed to an analog-to-digital converter (ADC) and stored in the block of a memory unit, with the block address derived via the pulse height of the SBD from a second ADC. Data transfer to the memory unit is triggered at the instant when a projectile recorded by the CEM hits the surface. Because recording of data is initiated by the CEM signal and the efficiency for detection of electrons by the SBD is close to 100%, no corrections for electron number spectra as in studies with the setup reported in Ref. [44] are necessary. Fig. 2.3 shows an electron pulse height spectrum recorded in coincidence with the CEM signal for 1.25 keV H^0 atoms scattered under $\psi = 1.3^\circ$, revealing well-resolved peaks for the emission of n electrons (including events where no electron is emitted!).

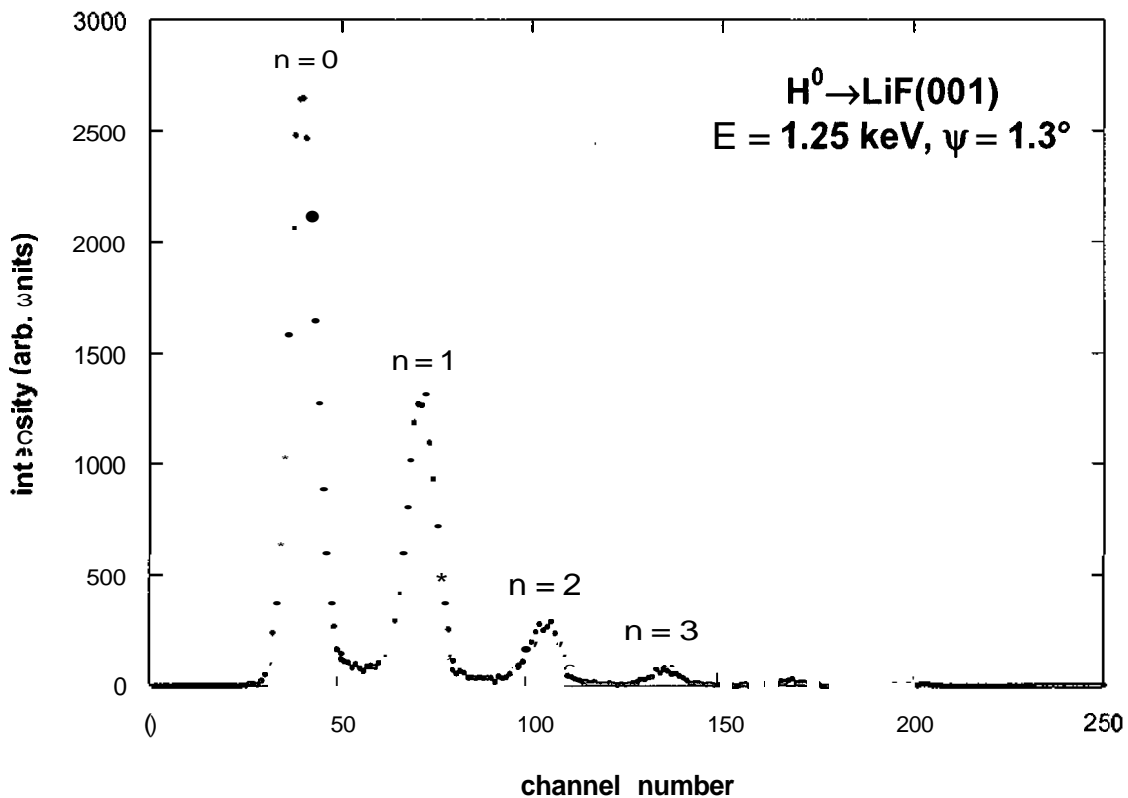


Fig. 2.3: Pulse height spectrum of the SBD for recording electrons in coincidence with 1.25 keV H^0 atoms scattered from $\text{LiF}(001)$ at $\psi = 1.3^\circ$.

II.2.3. Data analysis

Signal patterns as presented in fig. 2.3 allow to investigate the inelastic interaction mechanisms in detail. Owing to the high efficiency for detection of electrons, corrections in the evaluation of data play a negligible role and precise total electron yields from measured probabilities W_n for the emission of n electrons can be obtained from [32]

$$\gamma = \sum_{n=0}^{\infty} n W_n / \sum_{n=0}^{\infty} W_n. \quad (2.1)$$

The coincident detection of TOF and ES spectra delivers as well the probability W_0 for emission of no electron (see fig. 2.3) and makes our method a unique tool for precise measurements near the kinetic emission threshold, where γ is very small and W_0 dominates. The substantial progress for studies on electron emission achieved with this setup follows from the fact that an ES detector of "conventional" design does only provide data for nonzero numbers of electrons, and for small yields γ the probability W_0 has to be estimated from assumptions on the statistics of the emission processes [12].

TOF spectra obtained with 1.25 keV and 1.5 keV H^0 at $\psi = 1.3^\circ$ are displayed in Figs. 2.4(a) and (b). The spectra show discrete peaks as already reported in previous studies which can be attributed to specific electron excitation and emission processes [43, 44, 49, 50].

To determine the projectile energy loss the difference in the time-of-flight of scattered and non-scattered projectiles At has to be transformed to an energy scale. The rotational axis of the ion detector is not situated at the position of the target but further downstream which results in a difference of the flight lengths As . In a non-relativistic calculation the energy E_0 of the projectile is given by:

$$E_0 = \frac{m}{2} v_0^2 = \frac{m}{2} \frac{s_0^2}{t_0^2} \quad (2.2)$$

where m is the mass of the ion, s_0 the flight length of the unscattered ion, and t_0 the flight time.

Consequently the energy of the scattered ion is given by:

$$E_1 = E_0 - \Delta E = \frac{m}{2} \frac{s_1^2}{t_1^2} = \frac{m}{2} \left(\frac{s_0 + \Delta s}{t_0 + \Delta t} \right)^2 \quad (2.3)$$

and therefore the energy loss is

$$\Delta E = E_0 - \frac{m}{2} \left(\frac{s_0 + \Delta s}{\sqrt{\frac{m}{2E_0} s_0 + \Delta t}} \right)^2. \quad (2.4)$$

By tuning the delay of the direct beam in the time-of-flight spectrometer one can easily distinguish the time per channel (Δt_c) of the ADC. The time-difference Δt in a measured time-of-flight spectrum is therefore given by:

$$\Delta t = \Delta t_c \Delta k \quad (2.5)$$

where M is the number of channels in the ADC spectrum.

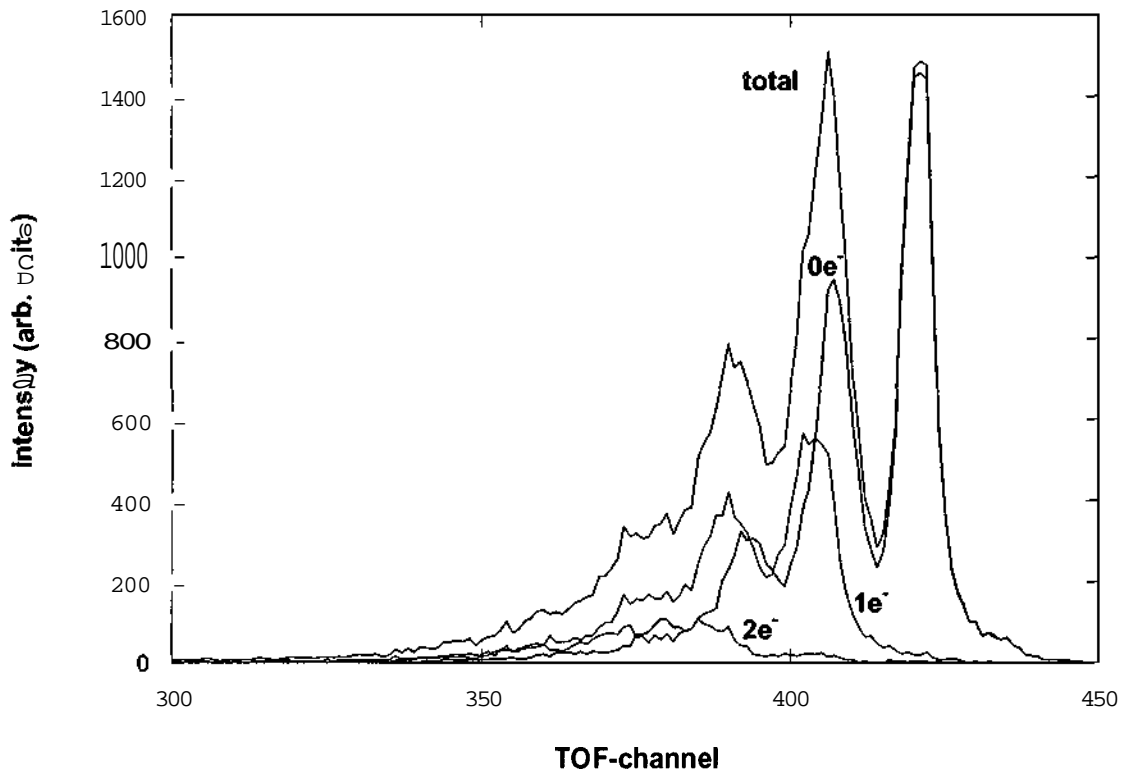


Fig. 2.4a: TOF-spectrum obtained for 1.25 keV H° atoms scattered from LiF(001) at $\psi = 1.3^\circ$. The spectra have been cut for different numbers of electrons.

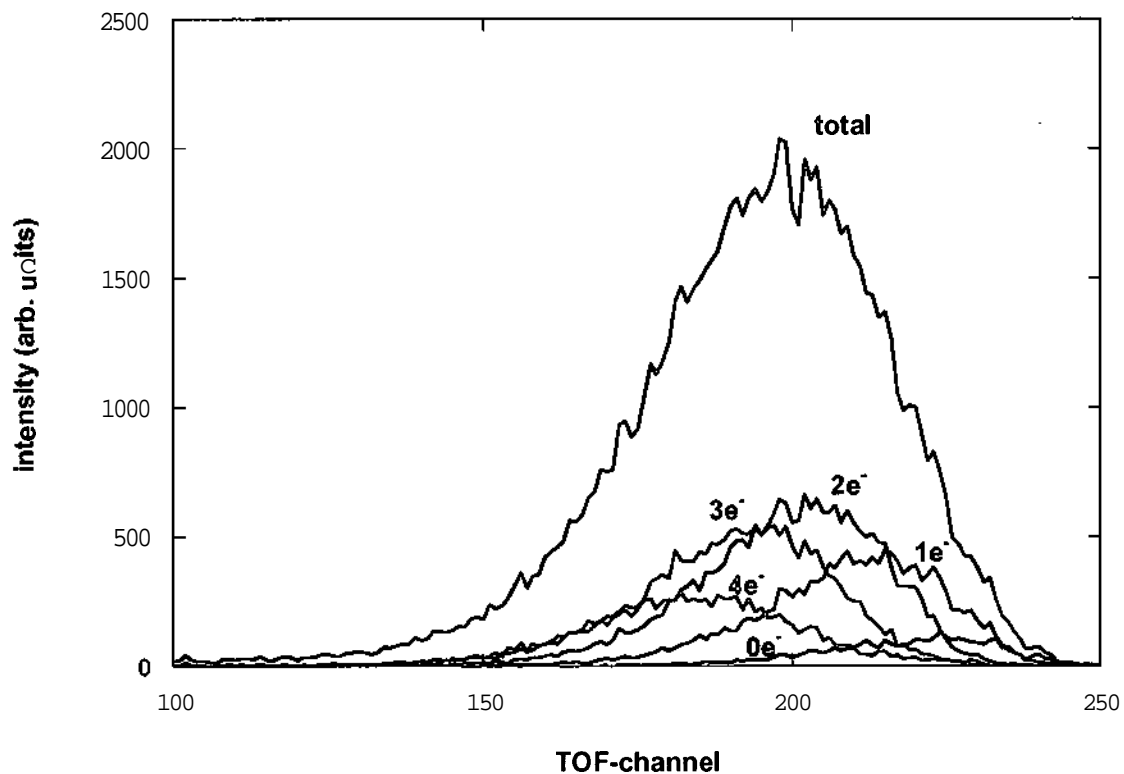


Fig. 2.4b: TOF-spectrum obtained for 1.5 keV H° atoms scattered from $\text{LiF}(\text{OOI})$ at $\psi=1.3^\circ$. The spectra have been cut for different numbers of electrons.

As the energy losses of the projectiles are small compared with the initial energy non-linear parts in the time-of-flight- energy loss transformation can be neglected for the measurements presented in this part of the thesis and it is sufficient to transform only the time scale.

II.3. Results for HO on LiF

From electron spectra and TOF spectra as shown in figs. 2.3 and 2.4, respectively, we derive total electron yields γ and mean energy losses ΔE .

In figs. 2.5(a) and (b), we show these mean values as function of angle of incidence ψ for 1.56 and 3.00 keV impact energy. The two scales are adjusted in a way, in order to match the electron yields γ (full circles) and energy losses ΔE (open circles) as close as possible. Within the uncertainty of our data, both data sets reveal the same dependence on ψ ; this statement holds for all measurements performed for energies ranging from about 1 to 20 keV. The solid curves are best fits to the data on the basis of position-dependent electron production rates $P(z)$ and projectile stopping powers $S(z)$. For simplicity we assume that for the range of distances probed by the projectiles ($z > 1$ a.u.) both functions can be approximated by a single exponential expression, i.e., $P(z) = P_0 \exp(-z/z_0)$ and $S(z) = S_0 \exp(-z/z_0)$. The parameters P_0 , S_0 and z_0 are obtained from best fits to the data for an integration over complete trajectories

$$\gamma(\psi_{in}) = \int_{traj} P(z) dz, \quad (2.6)$$

$$\Delta E(\psi_{in}) = \int_{traj} S(z) dz, \quad (2.7)$$

where classical trajectories are calculated using a planar continuum potential derived from "universal" interatomic potentials with ZBL-screening [51] for the Li and F sublattices of the crystal surface.

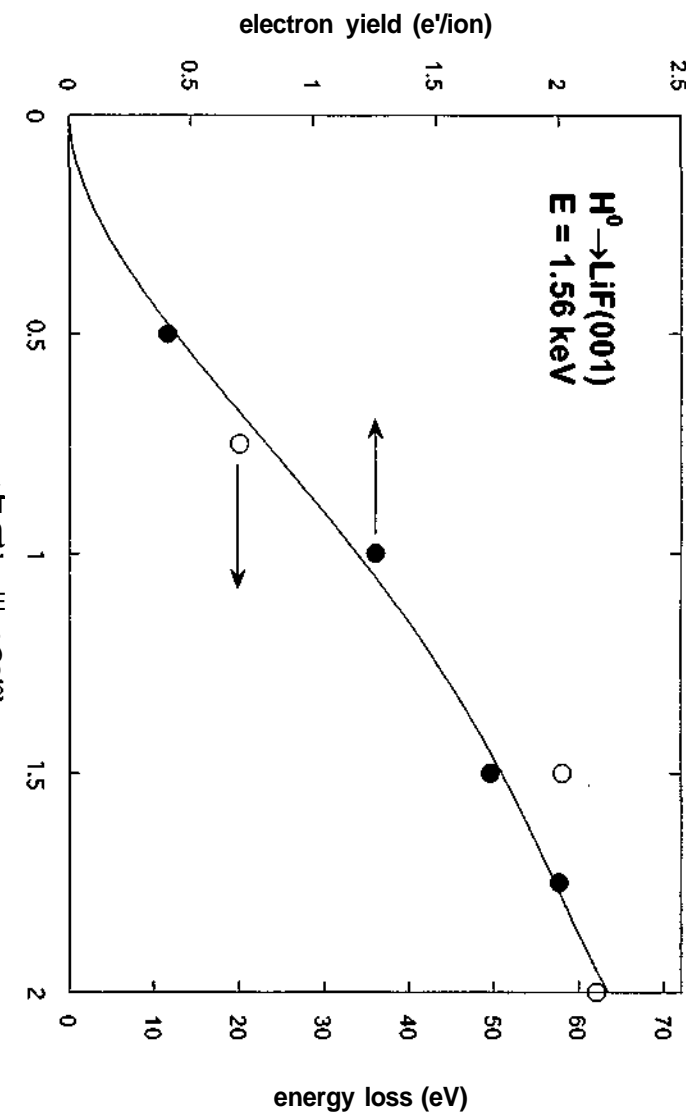


Fig. 2.5(a): Electron yield (full circles) and mean energy loss (open circles) as function of ψ for 1.56 keV H^0 scattered from $LiF(001)$.

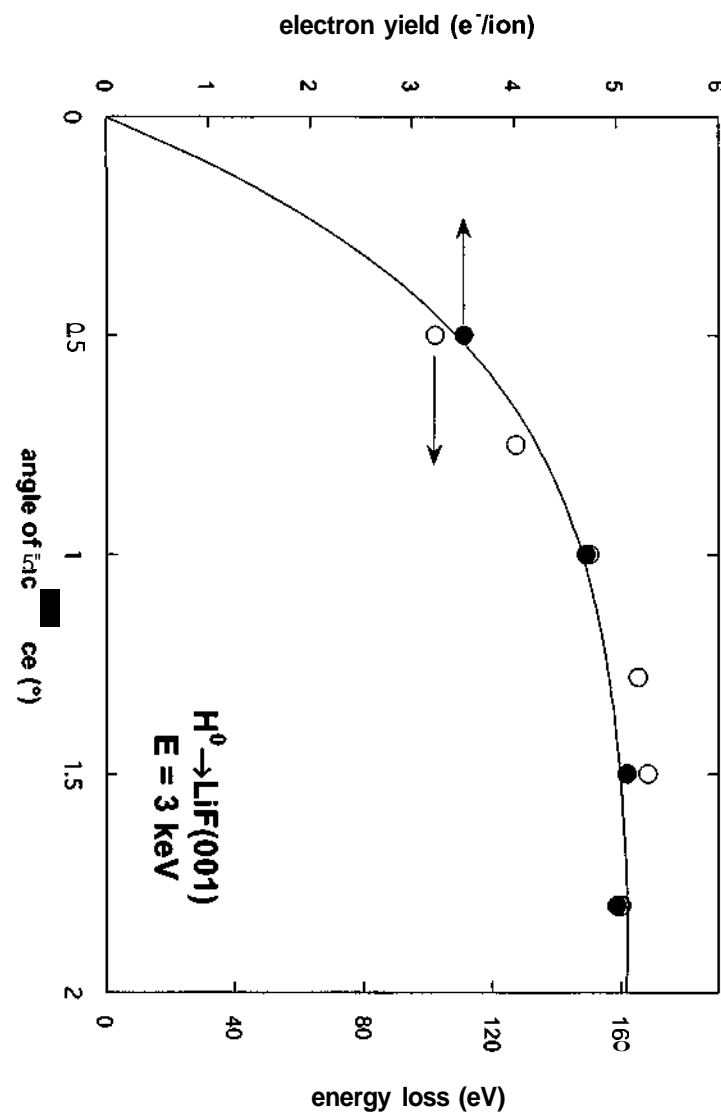


Fig. 2.5(b): Electron yield (full circles) and mean energy loss (open circles) as function of ψ for 3 keV H^0 scattered from $LiF(001)$.

In fig. 2.6, we display semi-logarithmic plots of $P(z)$ for different projectile energies. The good fits obtained in all cases (see, e.g., figs. 2.5(a) and (b)) imply that single exponential functions appear to be good approximations for $P(z)$ and $S(z)$. The monotonic increase of the electron yields with projectile energy [52] is reflected in a corresponding increase of the production rates. Up to energies of about 4 keV the slopes of $P(z)$ decrease, i.e., the decay z_0 length increases [52]. At higher projectile energies, the slopes and thus z_0 are about constant ($z_0 \approx 2.4$ a.u.) so that the position and energy dependence of the production rate can be separated according to $P(z, E) = P(E)P(z)$. We note that for this case we find $P(E) \sim E^{1/2} \sim v$ and also $S(E) \sim v$, which is the established velocity dependence for stopping in metals and gases at low velocities ($v < v_0$) [53]. For energies below about 4.2 keV ($v = 0.4$ a.u.) we find that z_0 varies linear with velocity. Thus, a separation of $P(z, E)$ in distance and energy-dependent factors is only feasible at higher impact energies. The finding for low velocities that $P(z)$ shows an exponential dependence $\exp(-\tau_0 z/v)$ (TO constant) is interpreted to originate from the transition probabilities between potential curves for the initial ($H + F'$) and final ($H\sim + F$) states [43, 44, 54] (see fig. 2.10 below).

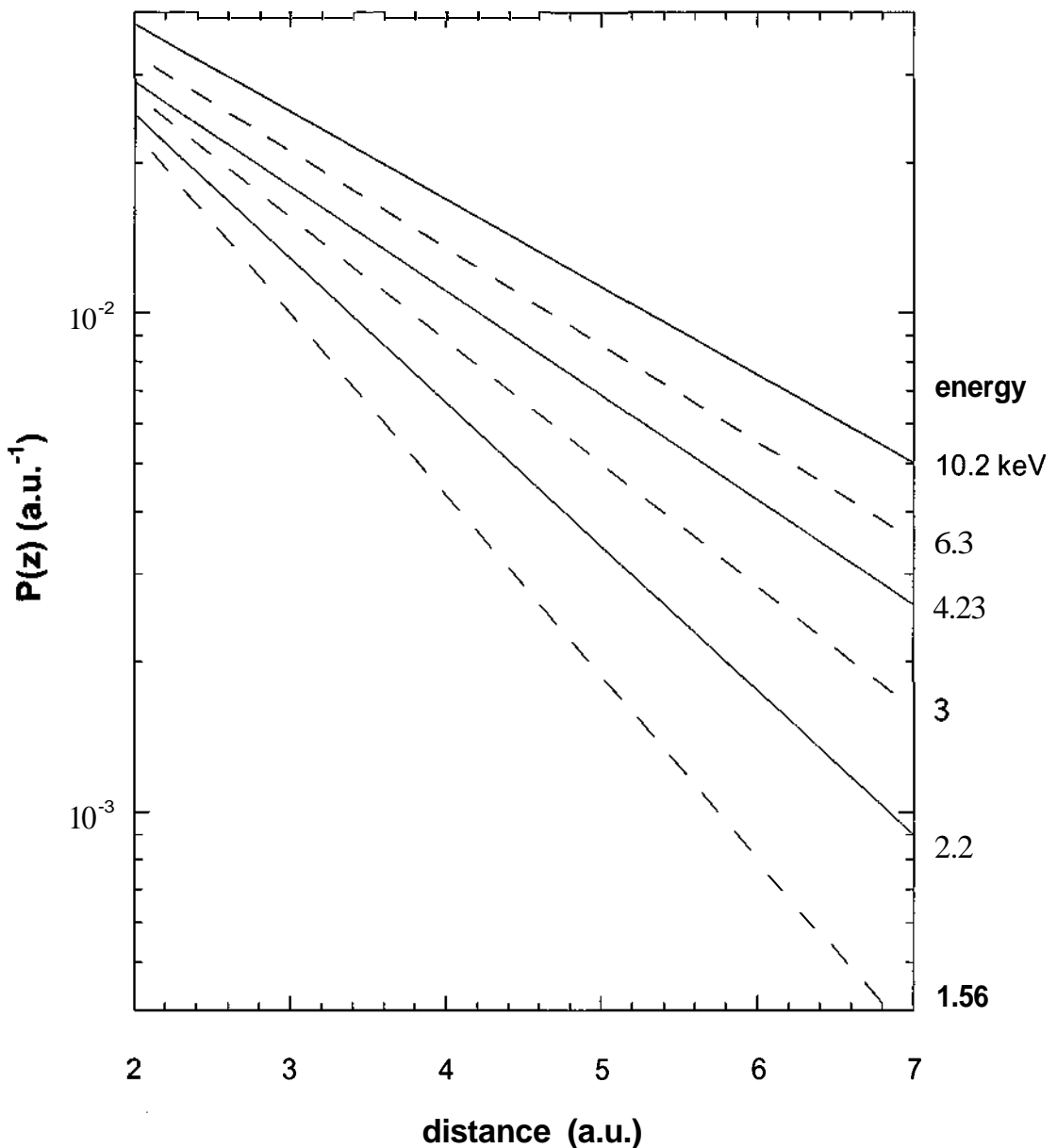


Fig. 2.6: Electron production rates $P(z)$ as function of distance z from the surface plane.

The fits to the data shown in figs. 2.5(a) and (b) result in ratios S_0/P_0 - (32.5 ± 1.0) eV/electron. This number is found to hold over the whole range of projectiles energies studied here and has also been reported in previous studies by Khemliche *et al.* [50]. Inspection of TOF spectra for the emission of one electron in fig. 2.4(a) reveals that an energy loss of 14 eV is related with this process, i.e., this energy is needed to excite electrons from the flat conduction band to vacuum. Considering that emitted

electrons have kinetic energies of 1 - 2 eV only this means that about 50% of the projectile energy is dissipated by other means than the ejection of electrons into vacuum. From the TOF spectra gated by specific pulse heights of the electron number detector the relevant excitation and emission processes can be analyzed. Roncin *et al.* [44] first observed discrete energy losses of 12 eV in the TOF spectra for the emission of no electron which are attributed to an internal electronic excitation of the target, creation of surface excitons at F" sites in the lattice with binding energies of about 1 eV with respect to vacuum. The energy loss accompanied by the emission of one electron is about 2 eV larger (see discussion above) and shows further discrete peaks owing to the additional excitation of excitons. TOF spectra for electron numbers up to 3 are resolved in the data shown in fig. 2.4(a).

As the measurements of TOF and electron multiplicities are done in coincidence one can use 2D plots of these two signals for further analysis.

In fig. 2.7 we show, as a representative example of data obtained with our coincidence setup, a 2D scatter plot of TOF (energy loss) versus electron number for 1 keV H° atoms from LiF(OOl) at an angle of incidence $\psi = 1.8^\circ$. In this plot several discrete features can clearly be identified for specific electron numbers (horizontal axis) as well as projectile flight times (vertical axis).

The identification of the discrete peaks in the figure is straightforward and follows the interpretation by Roncin *et al.* [44]. Elastic scattering from the surface is represented by the lowest peak in the left column showing negligible energy loss and no emission of electrons. The energy loss of 12 eV is attributed to the excitation of a surface exciton, i.e. a local excitation of a F" ion imbedded in the ionic lattice with a binding energy of about 1-2 eV with respect to vacuum. The mean energy necessary to lift an electron from the LiF valence band into vacuum with about 14 eV is larger than for producing an exciton. In the first column of fig. 2.7 multiple energy losses of 12 eV without electron emission correspond to population of (multiple) surface excitons. In the second column one can identify the energy loss for emission of one electron (14 eV) and additional excitations of excitons (12 eV), the third column shows events associated with the emission of 2 electrons and several excitons and so on.

1.2 keV H^0 - LiF(001), $\psi = 1.8^\circ$

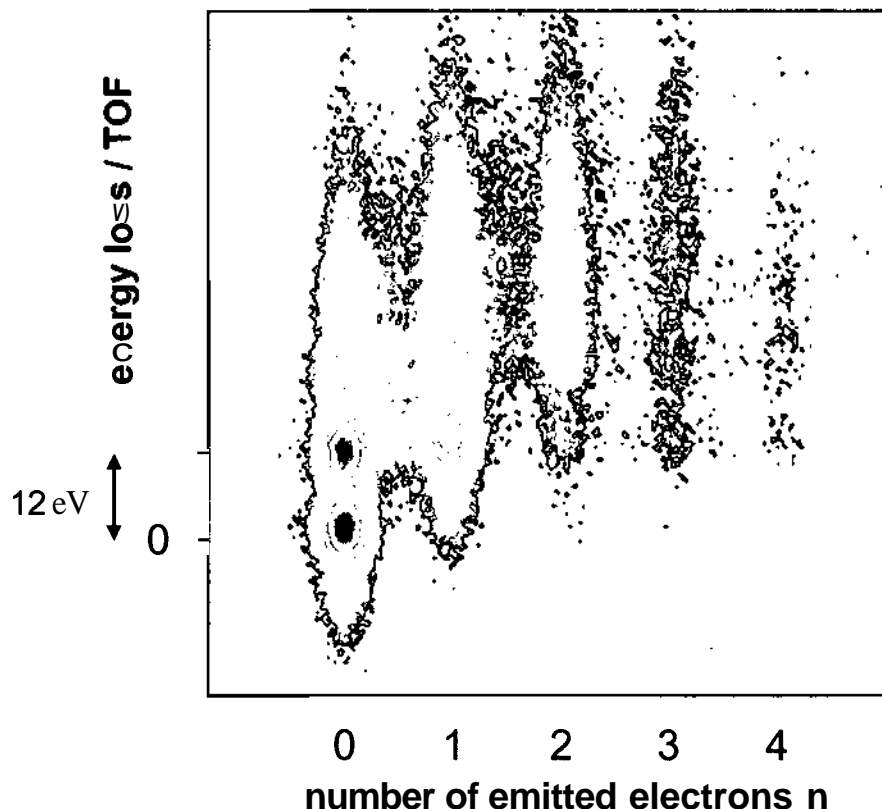


Fig. 2.7: 2D-TOF-electron number spectrum obtained for 1.2 keV H^0 atoms scattered from LiF(001) at 1.8° .

In fig. 2.8 for 400 eV and 800 eV H^0 scattered at $\psi=1.8^\circ$ one can now follow these discrete features for specific electron numbers (horizontal axis) and projectile flight time (vertical axis) down in impact energy to their respective thresholds.

In fig. 2.8b for 800 eV H^0 scattered at $\psi=1.8^\circ$ from LiF(001) still a number of inelastic channels are visible (up to events when one exciton is excited and one electron is emitted during a single collision event). Close to 400 eV impact energy (see fig. 2.8a), however, only very few events can be related to the emission of an electron while excitons are still produced.

$$H^0 - LiF(001), \psi = 1.8^\circ$$

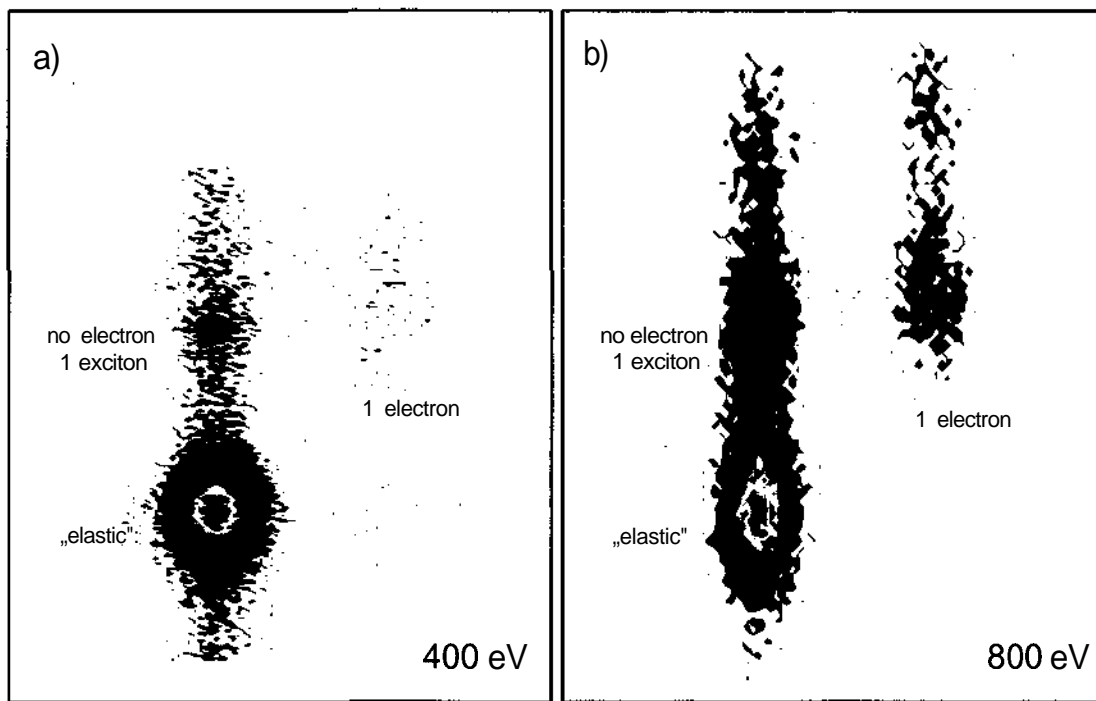


Fig. 2.8: Projectile time of flight versus number of emitted electrons for 400 eV (a) and 800 eV (b) H^0 impact on $LiF(001)$ at $\psi=1.8^\circ$.

From spectra taken at $\psi=1.8^\circ$ as shown in fig. 2.8 we derive fractions for the excitation of one exciton as well as for emission of one electron (fig. 2.9) We determine in addition by means of electric field plates and a further CEM, fractions of negative ions (H^-) in the scattered beam (positive ion fractions are negligible here) and also plot those in fig. 2.9. The data reveal a somewhat different kinetic onset behavior for the three quantities, with a dominance of the production of surface excitons. This finding can be used to clarify the relevant interaction mechanisms. In passing we note that the proportionality between electron yield and mean energy loss observed for this system at higher energies ($E > 1$ keV; see e.g. fig. 2.5) [44, 52] does not hold near the kinetic threshold.

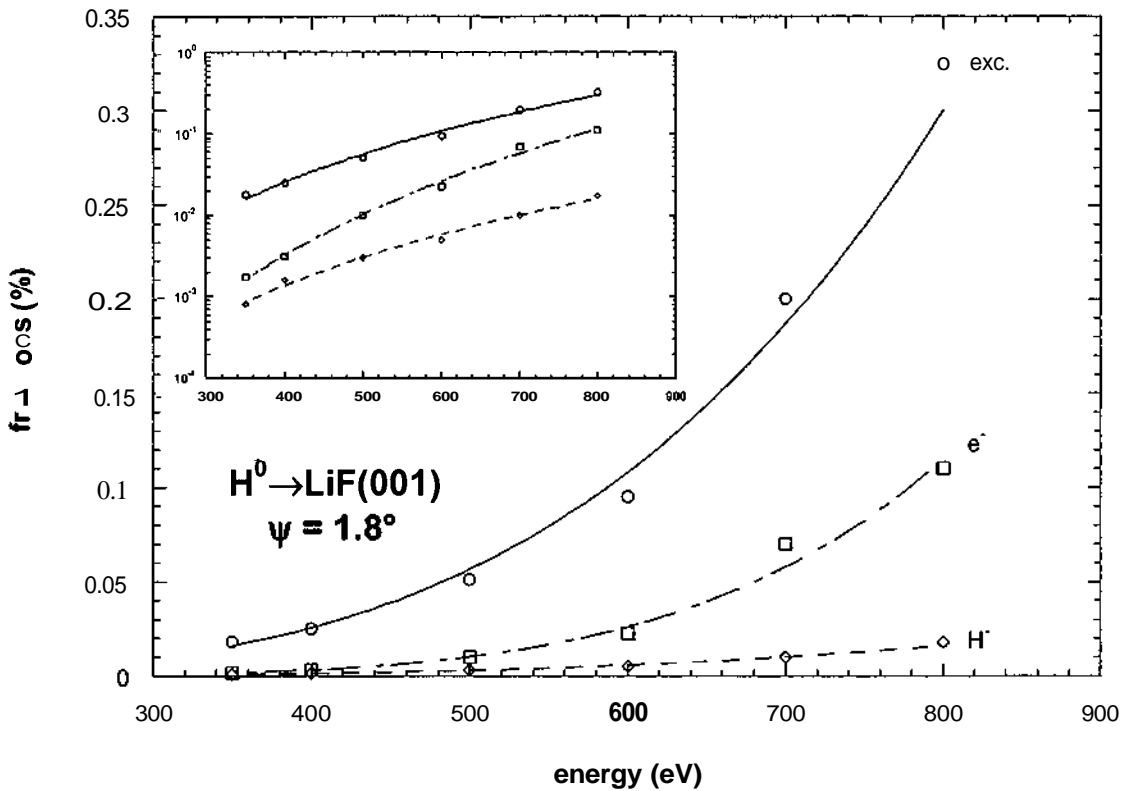


Fig. 2.9: Fractions of excitons (red circles), emitted electrons (blue squares), and H'' ions (green diamonds) for scattering of H° atoms from LiF(OOl) under $\psi = 1.8^\circ$ as function of projectile energy.

Electron emission from wide-band gap insulators as LiF is interpreted to proceed in binary collisions of H° atoms with F'' ions embedded at crystal lattice sites ("active sites"). The two current models for the microscopic interactions are presented in terms of potential curves as sketched in fig. 2.10. The upper panel (a) shows calculated potentials as derived in Ref. [42] with a crossing of diabatic curves for initial ($H^\circ + F''$) and final ($H'' + F^\circ$) interactions at a distance from the active site of $R \sim 4$ a.u. In this model, electron emission proceeds via electron promotion to vacuum (reference for energy scale $H^\circ + F^\circ$) at $R < 3$ a.u., and population of doubly excited F'' (F^{**}) with subsequent autoionization. In the alternative approach (b), diabatic potentials curves for the initial and final interactions do not cross, and H'' is the precursor for excitation of surface excitons (F^*) and electron emission via detachment ($H^\circ + e^-$) triggered by

interactions with lattice atoms surrounding active sites. In this qualitative picture, a diabatic curve crossing with the exciton branch ($H^0 + F^*$) is present.

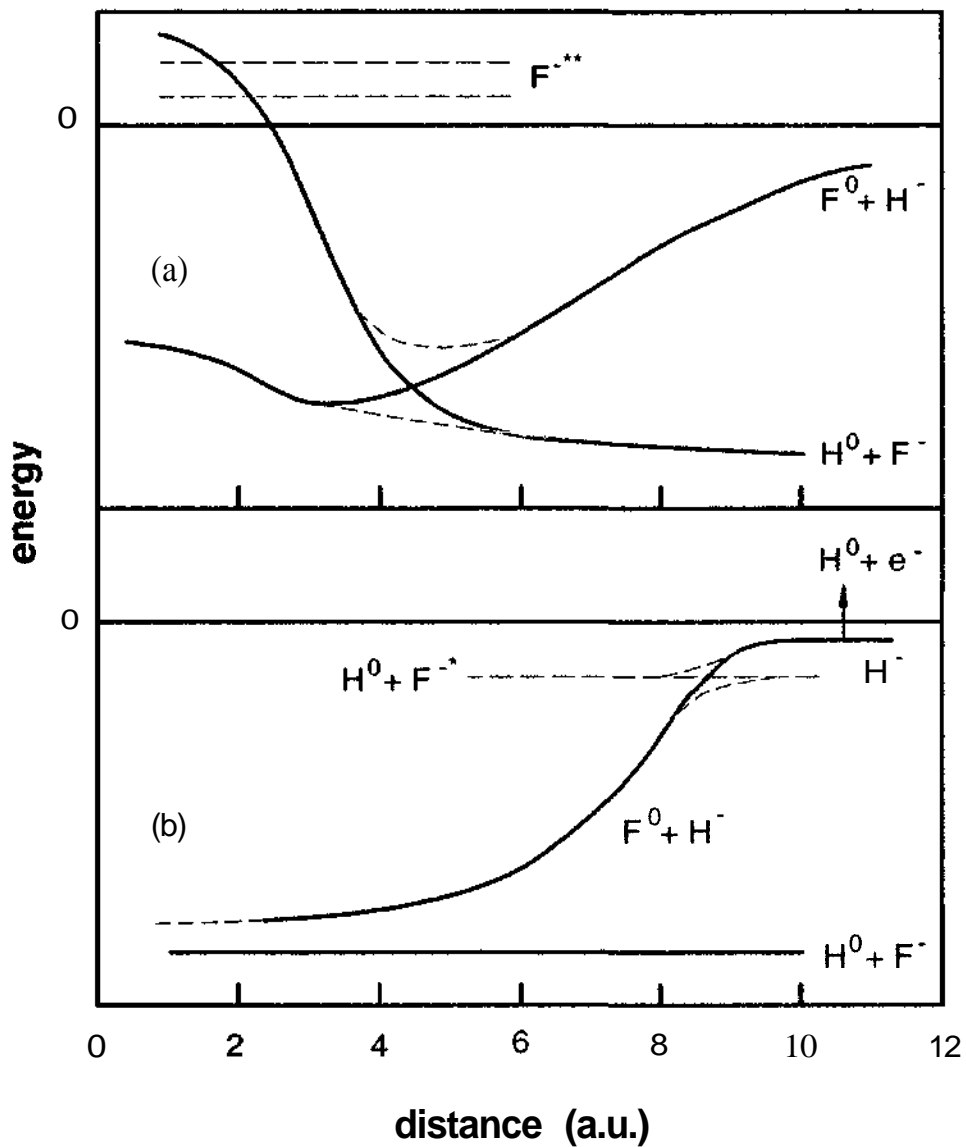


Fig. 2.10: Sketch of energy diagrams illustrating two models for the interaction of an H^0 atom with a LiF(OOI) surface (details see text).

Main features of model (b) were developed to describe the efficient formation of negative ions during grazing scattering of reactive ions from the surface of ionic crystals by capture of valence electrons from "active sites" with binding energies > 12 eV. Capture is mediated by a confluence of levels for the initial (here F^0) and final (here H^-) states owing to the Madelung potential acting on the active electron. From comparison

with recent coupled cluster calculations for F" formation at LiF [55], we conclude also for the present situation no crossing of the diabatic potential curves for distances of relevance here, contrary to model (a). In the following the two models are compared with the data.

- (1) Projectile trajectories derived from collective interatomic potentials for the Li and F sublattices of the surface using "universal screening" [51] have distances of closest approach $z_{min} > 3$ a.u. (fig. 2.10a) for the scattering conditions presented in this thesis. If a distance $R \sim 2.5$ a.u. is needed in model (a) to promote electrons into vacuum, a crossing with F^{**} is not reached, and no electron emission can take place.
- (2) The probability for electronic transitions in the present collision system can be estimated for the onset region from the data shown in fig. 2.9 and amounts to typically 1 % or less. For diabatic curve crossings in model (a) transition probabilities from Landau-Zener theory are estimated.

$$P \approx \exp\left(-\frac{\pi}{2\nu} \Delta E(R_x)^2 \left/ \frac{d}{dR} (V_{H^-+F^0} - V_{H^0+F^-}) R_x\right.\right) \quad (2.8)$$

(atomic units) with $\Delta E(R_x)$ being the energy gap between the adiabatic potential curves [dashed curves in fig. 2.10a] at the distance R_x for diabatic curve crossing and ν the projectile velocity. From the potential curves given in Ref. [42] $\Delta E(R_x) - 2.7$ eV = 0.10 a.u. is deduced as well as the slopes and from equ. (2.8) for 400 eV H⁰ atoms ($\nu = 0.127$ eV) $P \sim 0.4$ for avoiding the crossing in a single collision sequence during surface channeling is obtained. Even without knowledge on the specific collision sequence during surface channeling, such a transition probability would exceed the experimental findings by more than one order of magnitude.

In model (b), the transition probability P_{bin} from the initial potential curve (about "parallel" diabatic potential curves in the transition region) can be estimated from the Demkov model [56] which reads for low velocities

$$P_{bin} \approx 2e^{-\pi\Delta W/\nu} \quad (2.9)$$

with $1/\alpha = (\sqrt{E_1} + \sqrt{E_2})/\sqrt{2}$, E_1 and E_2 being the binding energies of the collision partners and ΔE the energy defect in the collision. For the specific case mentioned, $\Delta E \approx$

4 eV = 0.15 a.u. (see below) from (2.9) $P_{bm} \sim 4 \times 10^{-3}$ and, at grazing incidence, the total probability for an effective number of N collisions is $P \sim N \cdot P_{bin} \sim 2 - 3 \%$ with $N \sim 5 - 8$, in fair agreement with the experimental data.

In model (b), the transition probability to the potential curve $F^o + H''$ is directly related to the sum of all fractions in the excitation process (F''^* , e^- , and H''), i.e. $P \sim N \cdot P_{bin}$, $P_{bm} - n_{ex} + n_e + mi$. Since ΔE and thus also P depend on the distance from the surface, the distance of closest approach z_{min} has been kept constant for variation of v by the same energy of projectile motion normal to the surface $E_z - E_0 \sin^2 \psi = 0.4$ eV via tuning of ψ . Then lengths of trajectories scale according to $1/\psi_{in}$. Based on (2.9) a semilogarithmic plot of $(n_{ex} + n_e + n_{H''}) \cdot \psi_{in}$ versus $1/v$ for $350 \text{ eV} < E < 800 \text{ eV}$ ($1.91^\circ > \psi \geq 1.31^\circ$) shows in fig. 2.11 the expected linear behavior. From the slope $-\pi \alpha \Delta E$ a value $\Delta E = (4.0 \pm 0.5) can be deduced which is consistent with an estimate based on a lowering of the H'' binding energy by the Coulomb potential owing to the hole at the active site and by the dielectric response [54, 57, 58]. The effective number of collisions is deduced to $5.3 \leq N \leq 7.8$.$

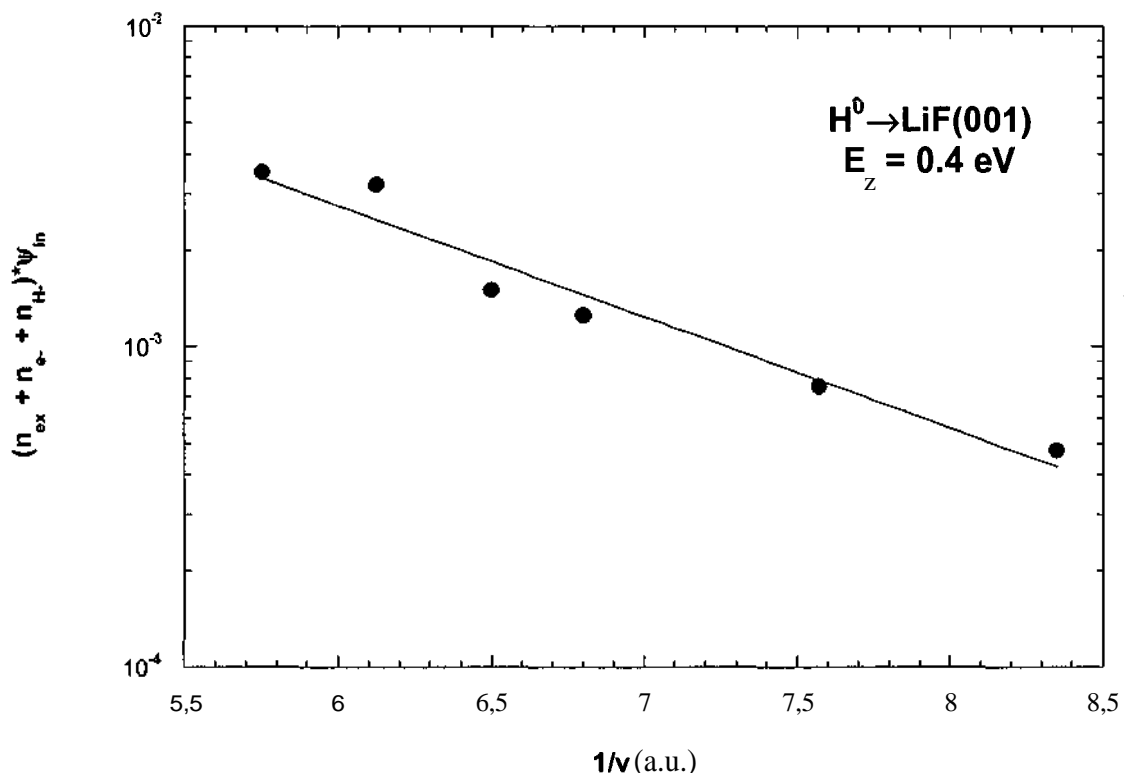


Fig. 2.11: Plot of $(n_{ex} + n_e + n_{H''}) \psi$ versus $1/v$ for constant energy of normal projectile motion $E_z - 0.4$ eV.

In the second step, the specific fractions in the excitation result from the curve crossing on the outgoing path at distances $\gg z_{min}$. Then the different kinetic threshold behavior for exciton production and electron emission is interpreted by an avoided crossing of the adiabatic potential curves [See fig. 2.10b]. It is expected that the potential parameters in equ. (2.9) show only a weak dependence on the collision geometry so that, e.g. the relative exciton yield $(n_{ex})/(n_{ex} + n_e + n_H)$ is given by $1 - P - 1 - \exp(-c/v)$. Experimental exciton yields as function of projectile energy as shown in fig. 2.12 are well fitted by $1 - P$ with $c \sim 0.22$ a.u. With a rough estimate of about 1 eV/a.u. for the difference in slope of the potential curves, we derive from equ. (2.8) for the separation of the adiabatic potential curves $\Delta E(R_x) \sim 2$ eV.

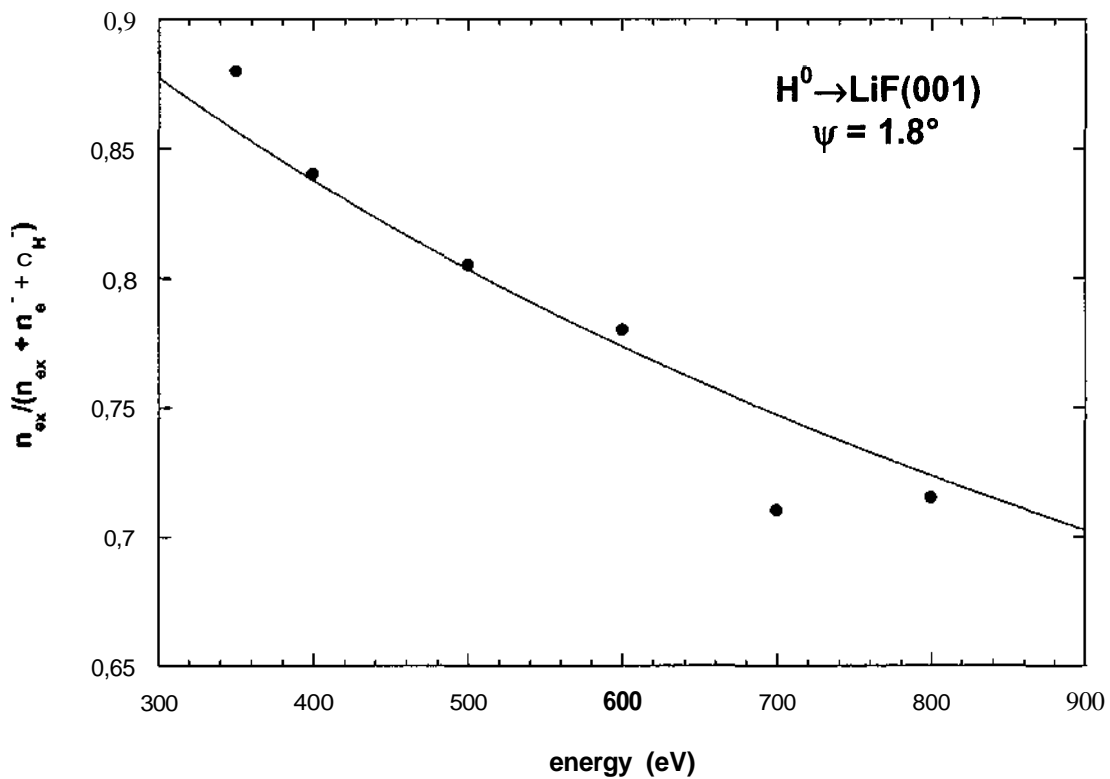


Fig. 2.12: Plot of $(n_{ex})/(n_{ex} + n_e + n_H)$ versus projectile energy for $\psi = 1.8^\circ$. Solid curve: description of data using eq. (2.8).

From spectra as shown in fig. 2.7 for H^0 atoms with energies ranging from 300 eV to 1.5 keV we also determine the fractions of peaks displayed in fig 2.7 and derive the normalized ratios for production of one surface exciton and emission of one electron

$n_{lex}/(n_{lex} + n_{le})$ as shown in fig. 2.13 for three different angles $\psi = 0.8^\circ$, 1.3° and 1.8° . These ratios are close to unity at the lowest impact energies of our studies and show a monotonic decrease with impact energy. The data reveal only a small systematic increase with decreasing angle of incidence. The green diamonds represent ratios observed for $\psi = 2.9^\circ$ by Khemliche *et al.* [50] and the solid curve illustrates the dependence as described by model (b).

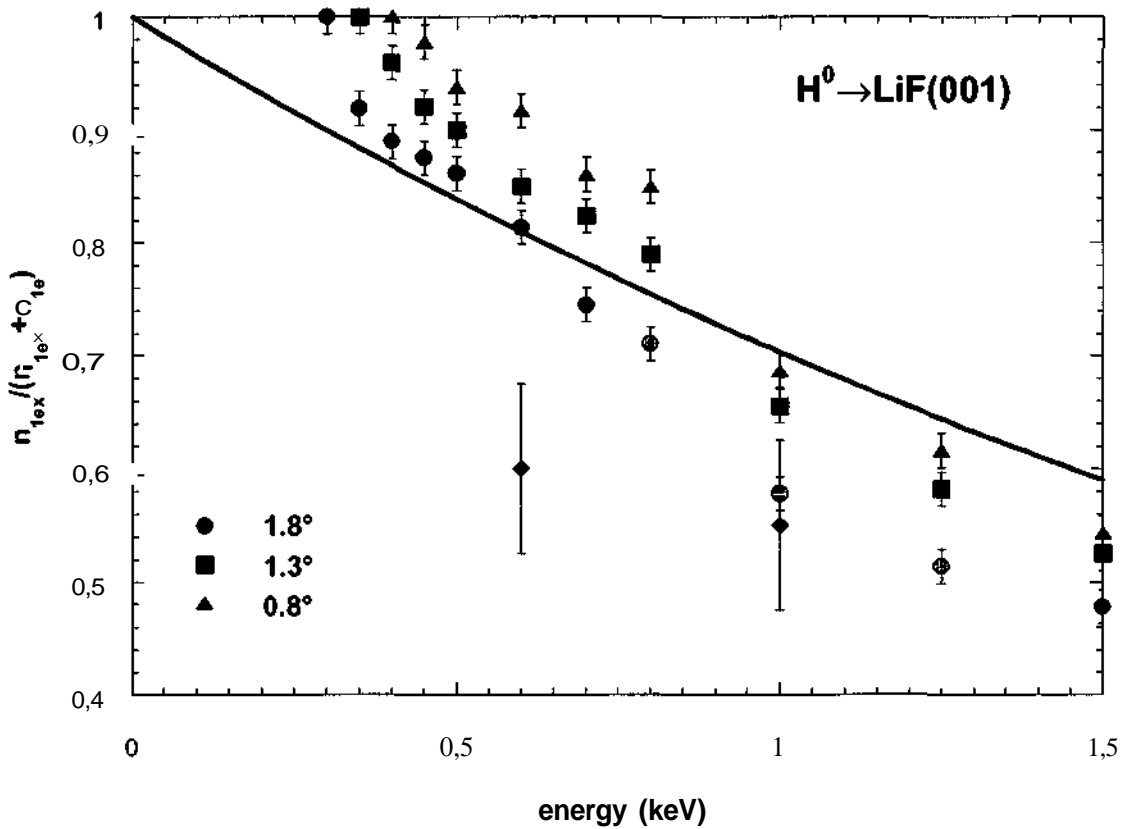


Fig. 2.13: Exciton fractions $n_{lex}/(n_{lex} + n_{le})$ as function of projectile energy for angles of incidence $\psi = 0.8^\circ$ (blue triangles), 1.3° (black squares), and 1.8° (red circles). Green diamonds: data from Ref. [50] for $\psi = 2.9^\circ$, solid curve: calculations using Equ. (2.8).

II.4. Results for He^0 on LiF

In fig. 2.14 total electron yields γ are shown for different velocities of He^0 atoms impinging on LiF(OOl) under $\psi = 1.8^\circ$. The measurements show a similar behavior but a slightly higher yield than results for H^0 atoms scattered from LiF(OOl). As in the latter case the number of emitted electrons in grazing incidence collisions depends on the distance of closest approach.

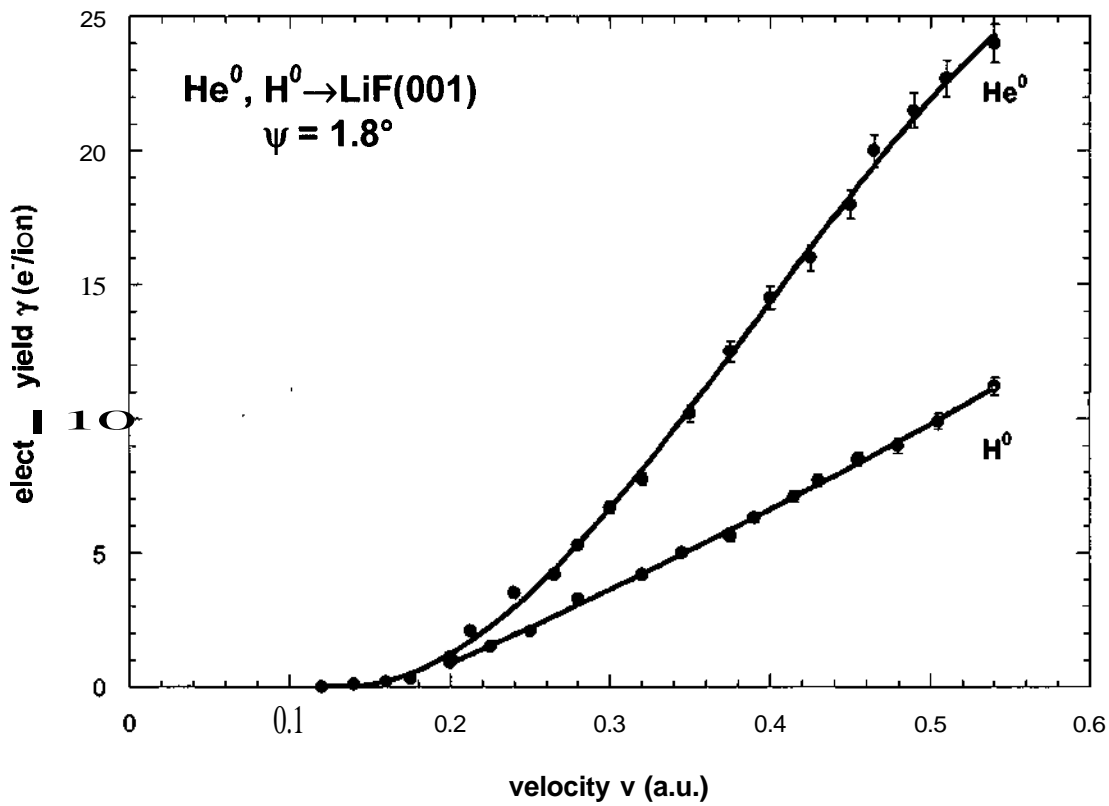


Fig. 2.14: Total electron yield γ for He^0 (blue) and H^0 (red) atoms scattered from LiF(OOl) under $\psi = 1.8^\circ$.

Using equ. (2.6) one can again calculate production rates for electrons taking the exponential approximation

$$P_z = P_0 \exp^{-\frac{z}{z_0}} \quad (2.10)$$

with the parameters P_0 and the decay length z_0 for a given projectile energy deduced from numeric integration of (2.6) and fitting this function to the measured electron yields (z being the distance from the target surface). Fig. 2.15 shows calculated values for z_0 and PO as derived by this fitting procedure for electron emission of He^0 atoms scattered from LiF(OOL) for different projectile velocities. The decay length z_0 first shows a linear dependence for low velocities up to 1 a.u. and then remains constant for higher velocities. This results are in qualitative agreement with our measurements for hydrogen projectiles. The parameter P_0 shows a completely different behavior compared to ZQ . Between $v \sim 0.3$ a.u. and 1 a.u. PO strongly decreases with increasing velocity. Both parameters remain constant for velocities $v > 1$ a.u. Since the behavior of He^0 atoms impinging on LiF is very similar to that of hydrogen atoms the results can be interpreted in a similar way. LiF as alkali-halide is a wide-bandgap insulator so that direct excitation of valence band electrons into vacuum which is the dominant mechanism in atom-metal interaction can be ruled out. For angles of grazing incidence the interaction with the surface can be seen as local interaction in binary collisions of projectiles with negative halogen sites in the ionic lattice.

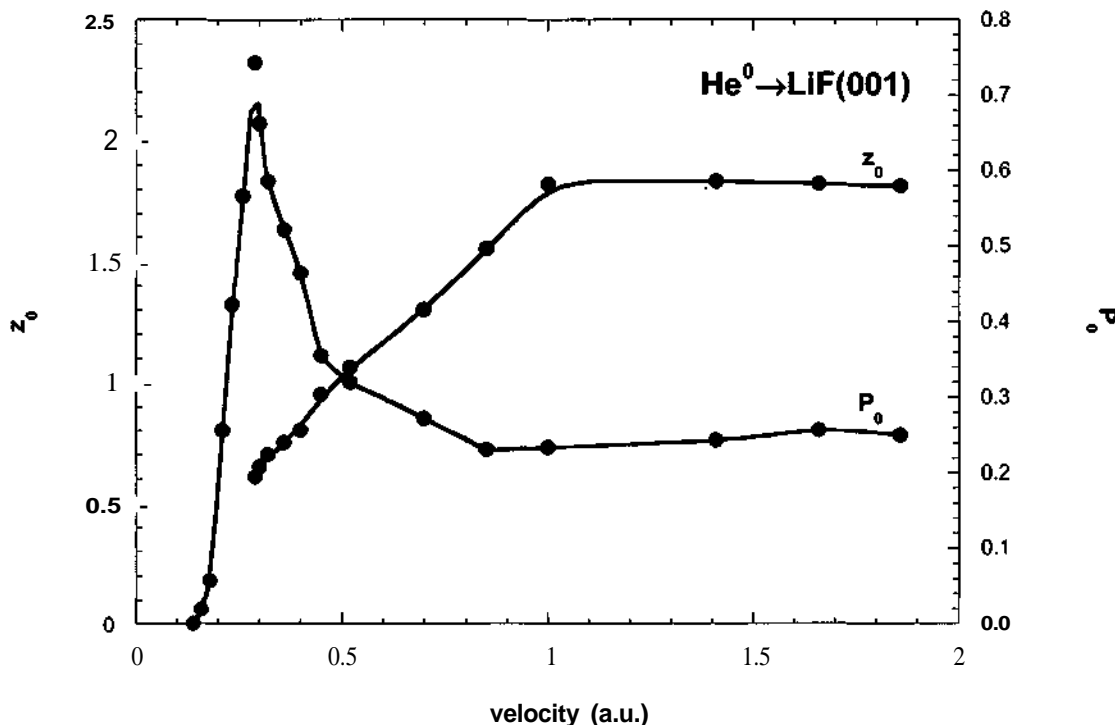


Fig. 2.15: Decay length z_0 and production rate PO for electron emission of He^0 atoms scattered from $\text{LiF}(001)$.

Summary

In this thesis new experimental investigations on the interaction of neutral atoms and (multicharged) ions with insulating LiF surfaces are presented. The experiments are performed under grazing angles of incidence, which has the advantage that the collisions with the surface proceed along well-defined trajectories (surface channeling). Interesting details of the interaction mechanisms could be revealed by measuring the projectile energy loss (and -angular scattering patterns) in coincidence with the number distribution of emitted electrons.

For multiply charged Ar^{q+} ions ($q = 2-8$) the projectile energy loss derived from the respective time-of-flight was correlated with the number of electrons emitted along specified trajectories. An extrapolation of our data to projectiles with zero energy loss allowed us to separate potential and kinetic contributions to electron emission in an impact region where both are strongly contributing to the total electron yield. The potential emission found increases linearly with the available potential energy of the projectiles. On the other hand by extrapolation of the projectiles energy loss to cases with no emission of electrons we could demonstrate that the stopping power associated with the energy loss is (as expected) proportional to projectile velocity and shows a weak charge state dependence in agreement with data obtained earlier for MCI impact on LiF under normal incidence.

In similar experiments carried out in Berlin with hydrogen atoms as projectiles information on the specific mechanism for kinetic electron emission from LiF could be obtained. Coincident TOF - electron number spectra revealed the production of surface excitons and the emission of electrons as dominant interaction mechanisms. Yields of excitons and electrons and, in addition, also fractions of negative hydrogen ions, recorded as function of projectile energy showed a clearly different threshold behavior. In a detailed analysis we could demonstrate that the specific features of electron emission for impact of atomic projectiles on insulator surfaces can be understood by a promotion mechanism where the formation of H^+ ions serves as precursor. Formation of H^+ ions and the subsequent production of excitons and emission of electrons can be described by Demkov- and Landau-Zener theory, respectively.

References

- [1] D. Hasselkamp, in *Particle Induced Electron Emission II*, edited by G. Höhler (Springer, Heidelberg, 1992), Vol. 123, p. 1
- [2] M. Rosier and W. Brauer, in *Particle Induced Electron Emission I*, edited by G. Höhler (Springer, Berlin, 1991), Vol. 122.
- [3] R. Baragiola, in *Chap. IV in Low energy Ion-Surface Interactions*, edited by J. W. Rabalais (Wiley, 1993).
- [4] G. Spierings, I. Urazgil'din, P. A. Zeijlmans van Emmichoven, and A. Niehaus, *Phys.Rev.Lett.* **74**, 4543 (1995).
- [5] J. Burgdörfer, in *Fundamental Processes and Applications of Atoms and Ions*, edited by C. D. Lin (World Scientific, 1993).
- [6] A. Arnau, F. Aumayr, P. M. Echenique, M. Grether, W. Heiland, J. Limburg, R. Morgenstern, P. Roncin, S. Schippers, R. Schuch, N. Stolterfoht, P. Varga, T. J. M. Zouros, and H. P. Winter, *Surf. Sci. Reports* **229**, 1 (1997).
- [7] H. Winter and F. Aumayr, *J.Phys.B:At.Mol.Opt.Phys.* **32**, R39 (1999).
- [8] H. P. Winter and F. Aumayr, *Euro. Phys. News* **33**, 215 (2002).
- [9] F. Aumayr, H. Kurz, D. Schneider, M. A. Briere, J. W. McDonald, C. E. Cunningham, and H. P. Winter, *Phys.Rev.Lett.* **71**, 1943 (1993).
- [10] J. Limburg, S. Schippers, R. Hoekstra, R. Morgenstern, H. Kurz, F. Aumayr, and H. P. Winter, *Phys.Rev.Lett.* **75**, 217 (1995).
- [11] H. Winter, *Physics Reports* **367**, 387 (2002).
- [12] M. Vana, F. Aumayr, P. Varga, and H. P. Winter, *Europhys. Lett.* **29**, 55 (1995).
- [13] S. Zamini, G. Betz, W. Werner, F. Aumayr, H. P. Winter, J. Anton, and B. Fricke, *Surf. Sci.* **417**, 372 (1998).
- [14] K. Töglhofer, F. Aumayr, and H. P. Winter, *Surf.Sci.* **281**, 143 (1993).
- [15] H. Eder, F. Aumayr, and H. P. Winter, *Nucl.Instrum.Meth.B* **154**, 185 (1999).
- [16] C. Lemell, J. Stöckl, J. Burgdörfer, G. Betz, H. P. Winter, and F. Aumayr, *Phys.Rev.Lett.* **81**, 1965 (1998).
- [17] H. Kurz, K. Töglhofer, H. P. Winter, F. Aumayr, and R. Mann, *Phys.Rev.Lett.* **69**, 1140 (1992).

- [18] M. Vana, F. Aumayr, P. Varga, and H. P. Winter, *Nucl. Instrum. Meth. Phys. Res. B* 100, 284 (1995).
- [19] H. Winter, *Europhys.Lett.* **18**, 207 (1992).
- [20] V. A. Morosov, A. Kalinin, Z. Szilagyi, M. Barat, and P. Roncin, *Rev.Sci.Instrum.* **67**, 6 (1996).
- [21] J. Stöckl, C. Lemell, H. P. Winter, and F. Aumayr, *Phys. Scr.* **T92**, 135 (2001).
- [22] M. Leitner, D. Wutte, J. Brandstötter, F. Aumayr, and H. Winter, *Rev.Sci.Instrum.* **65**, 1091 (1994).
- [23] C. Lemell, (TU Wien, 1998).
- [24] C. Lemell, J. Stöckl, H. P. Winter, and F. Aumayr, *Rev. Sci. Instrum.* **70**, 1653 (1999).
- [25] C. Kittel, *Introduction to Solid State Physics* (Wiley, New York, 1971).
- [26] I. G. Hughes, J. Burgdörfer, L. Folkerts, C. C. Havener, S. H. Overbury, M. T. Robinson, D. M. Zehner, P. A. Zeijlmans van Emmichoven, and F. W. Meyer, *Phys.Rev.Lett.* **71**, 291 (1993).
- [27] J. Burgdörfer, in *Fundamental Processes and Applications of Atoms and Ions*, edited by C. D. Lin (World Scientific, Singapore, 1993).
- [28] F. Aumayr and H. P. Winter, *Comments At.Mol.Phys.* **29**, 275 (1994).
- [29] C. Auth, T. Hecht, T. Igel, and H. Winter, *Phys.Rev.Lett.* **74**, 5244 (1995).
- [30] G. Lakits, F. Aumayr, and H. P. Winter, *Rev.Sci.Instrum.* **60**, 3151 (1989).
- [31] G. Lakits, F. Aumayr, M. Heim, and H. P. Winter, *Phys.Rev.A* **42**, 5780 (1990).
- [32] F. Aumayr, G. Lakits, and H. P. Winter, *Appl.Surf.Sci.* **47**, 139 (1991).
- [33] H. Kurz (Technische Universität Wien, 1994).
- [34] M. Bergsmann, P. Hörlsberger, F. Kastner, and P. Bauer, *Phys. Rev. B* **58**, 5139 (1998).
- [35] M. Bergsmann, P. Hörlsberger, F. Kastner, and P. Bauer, *Nucl. Instrum. Meth. Phys. Res. B* **136 - 138**, 1218 (1998).
- [36] R. Pfandzelter, *Phys. Rev. B* **57**, 15496 (1998).
- [37] V. A. Morozov, F. W. Meyer, and P. Roncin, *Physica Scripta* **T80**, 69 (1999).
- [38] H. D. Hagstrum, in *Electron and Ions Spectroscopy of Solids*, edited by L. Fiermans, J. Vennik and W. Dekayser (Plenum, New York, 1978), p. 273.
- [39] C. Auth and H. Winter, *Physica Scripta* **T92**, 35 (2001).

[40] K. Eder, D. Semrad, P. Bauer, P. Maier-Komor, F. Aumayr, M. Penalba, A. Arnau, J. M. Ugalde, and P. M. Echenique, Phys. Rev. Lett. **79**, 4112 (1997).

[41] J. Schou, Scanning Microsc. **2**, 607.

[42] P. A. Zeijlmans van Emmichoven, A. Niehaus, P. Stracke, F. Wiegershaus, S. Krischok, V. Kempter, F. J. Garcia de Abajo, and M. Penalba, Phys. Rev. B **59**, 10950 (1999).

[43] C. Auth, A. Mertens, H. Winter, and A. Borisov, Phys. Rev. Lett. **81**, 4831 (1998).

[44] P. Roncin, J. Villette, J. P. Atanas, and H. Khemliche, Phys. Rev. Lett. **83**, 864 (1999).

[45] P. Stracke, F. Wiegershaus, S. Krischok, V. Kempter, P. A. Zeijlmans van Emmichoven, A. Niehaus, and F. J. Garcia de Abajo, Nucl. Instrum. Meth. Phys. Res. B **125**, 67 (1997).

[46] D. S. Gemmel, Rev. Mod. Phys. **46**, 129 (1974).

[47] R. Sizmann and C. Varelas, *Festkörperprobleme* **17**, 1977).

[48] S. Lederer, (HU Berlin, 2001).

[49] H. Winter, C. Auth, and A. Mertens, Nucl. Instrum. Meth. Phys. Res. B **164**, 559 (2000).

[50] H. Khemliche, J. Villette, P. Roncin, and M. Barat, Nucl. Instrum. Meth. Phys. Res. B **164**, 608 (2000).

[51] J. F. Ziegler, J. P. Biersack, and U. Littmark, *The Stopping and Range of Ions in Matter* (Pergamon, New York, 1985).

[52] H. Eder, K. Mertens, K. Maass, H. Winter, H. P. Winter, and F. Aumayr, Phys. Rev. A **62**, 052901 (2000).

[53] P. M. Echenique, R. M. Nieminen, and R. H. Ritchie, Solid State Commun. **37**, 779 (1981).

[54] A. G. Borisov and V. Sidis, Phys. Rev. B **56**, 10628 (1997).

[55] A. G. Borisov, J. P. Gauyacq, V. Sidis, and A. K. Kazansky, Phys. Rev. B **63**, 045407 (2001).

[56] Y. N. Demkov, Sov. Phys. JETP **18**, 138 (1964).

[57] C. Auth, A. G. Borisov, and H. Winter, Phys. Rev. Lett. **75**, 2292 (1995).

[58] A. G. Borisov, V. Sidis, and H. Winter, Phys. Rev. Lett. **77**, 1893 (1996).

Danksagung

An dieser Stelle sei allen Personen gedankt, die zum Gelingen der vorliegenden Arbeit beigetragen haben.

Zu allererst danke ich natürlich meinem Betreuer Herrn a.o. Univ. Prof. Dr. Friedrich Aumayr für die ausgezeichnete Betreuung und das Vertrauen. Vor allem möchte ich mich für die Möglichkeit von Forschungsaufenthalten im Ausland sowie für die Unterstützung bei experimentellen „Notfällen“ bedanken.

Ich möchte mich auch sehr herzlich bei unserem Institutsvorstand Herrn o. Univ.-Prof. Dr. Hannspeter Winter für sein Interesse am Fortgang der Arbeit, sowie für seinen fachkundigen Rat und aufmunternden Worte bei Problemen bedanken.

Dank gebührt auch allen Mitgliedern der Arbeitsgruppe, insbesondere Herrn S. Cernusca und Herrn E. Galutschek, die durch ihr kollegiales Verhalten eine angenehme Atmosphäre schufen, und auch dazu beigetragen haben, dass ich nicht nur Kollegen hatte, sondern auch gute Freunde gefunden habe.

Herrn Prof. Helmut Winter möchte ich für die Möglichkeit danken an seinem Institut an der Humboldt Universität zu Berlin Messungen durchführen zu können. Weiters sei dem Team in Berlin, namentlich Herrn Dr. Axel Mertens und Herrn Dipl.-Phys. Sven Lederer, für die Zusammenarbeit gedankt.

Besonderer Dank gilt meinen Eltern, die mir durch ihre Unterstützung dieses Studium ermöglicht haben.

Zum Schluss bedanke ich mich bei meinem Bruder, Freunden und Freundinnen, die für die nötige Abwechslung gesorgt haben. Die aber vor allem dann wichtig waren, wenn es nicht so gut lief.

Die Arbeiten wurden im Rahmen eines Projekts des Fonds zur Förderung der wissenschaftlichen Forschung in Österreich (Proj. Nr.: 14337-PHY) durchgeführt und auch teilweise von EURATOM-ÖAW (Proj. P2) finanziert.

Lebenslauf

Johannes Stöckl

Geb. 27. April 1973 in Wien
Hohe Schule 5, 2122 Ulrichskirchen
Tel.: 0676 351 49 59
e-mail: stoeckl@iap.tuwien.ac.at

1979 - 1983 Volksschule Ulrichskirchen-Schleinbach
1983 - 1997 Gymnasium der Stadt Wien BRG XXI
1987 - 1992 HTBLA Wien XXII Fachrichtung Nachrichtentechnik-Informatik
1992 - 1993 Präsenzdienst
1993 - 2000 Diplomstudium Technische Physik an der TU Wien
Diplomarbeit: „*Ioneninduzierte Elektronenemission an Isolatoroberflächen bei streifender Streuung*“
am Institut für Allgemeine Physik
Betreuer: a.o. Univ.-Prof. Dr. Friedrich Aumayr
2000 - Doktoratsstudium Technische Physik an der TU Wien
Dissertation: „*Electron Emission and Energy Loss in Grazing Collisions of Multiply Charged Ions and Neutral Projectiles with Insulator Surfaces*“
am Institut für Allgemeine Physik
Betreuer: a.o. Univ.-Prof. Dr. Friedrich Aumayr

Forschungsaufenthalte:

1997 Lawrence Berkeley National Laboratory (LBNL), Berkeley, USA
2000 - 2001 Humboldt Universität zu Berlin, Berlin, Deutschland
2000 Commissariat à l'Energie Atomique (CEA), Grenoble, Frankreich
2002 Centre Interdisciplinaire de Recherche Ions Lasers (CIRIL), Caen, Frankreich